UNIVERSITY OF CALIFORNIA
RIVERSIDE

Low-energy Ion-surface Interactions at Semiconductor and High-T_C Superconductor Surfaces

A Dissertation submitted in partial satisfaction
of the requirements for the degree of

Doctor of Philosophy

in

Physics

by

Reuben David Gann

December 2011

Dissertation Committee:

Dr. Jory A. Yarmoff , Chairperson
Dr. Ward P. Beyermann
Dr. Allen P. Mills

The Dissertation of Reuben David Gann is approved:

Committee Chairperson

University of California, Riverside

Acknowledgments

A good adviser has to evaluate a student and determine whether he needs to be managed closely or left alone. By that account, Jory is an excellent adviser. Though I'm substantially a lone wolf in the lab, he was always there with a good suggestion, kind word, or pointed question when I needed it.

The work put forth in this document was mainly done by me and Jory Yarmoff, but would have been impossible without Zdenek Sroubek, Genda Gu and his group at Brookhaven, and Ruqian Wu, our collaborators. In running nearly inscrutable simulation code, I depended on the expertise of Marcus Karolewski (author of KALYPSO) and Roland Kolasinski (for help with MARLOWE). They endured endless email conversations to my benefit.

I was fortunate to meet Abhay Pasupathy, who told me of this method for cleaving samples in ultra-high vacuum. A technique that involves two kinds of epoxy with different curing times and temperatures could not have been simple to devise.

This thesis was supported by grants from the U.S. Army Research Laboratory and the U.S. Army Research Office under Contract/Grant No. 52723PH, and by the National Science Foundation under CHE-1012987.

My father and late mother supported me financially and were quite confident in my abilities. Needless to say, this was indispensable.

Finally, thanks to my wonderful wife, who always assumed I was much more capable than I did, and never thought for a minute I would fail.

To Jessica.

ABSTRACT OF THE DISSERTATION

Low-energy Ion-surface Interactions at Semiconductor and High-T_C Superconductor Surfaces

by

Reuben David Gann

Doctor of Philosophy, Graduate Program in Physics
University of California, Riverside, December 2011
Dr. Jory A. Yarmoff , Chairperson

Low-energy ion scattering is a powerful surface analysis technique for interrogating the structural and chemical makeup of a surface, as well as the electronic structure. We used this technique to probe the local electrostatic potential of $Bi_2Sr_2CaCu_2O_8$, and corroborated the findings of density functional theory. Sputtering with Ar^+ ions was conducted on this same material, revealing the formation of a Bi capping layer that prevents further damage due to the low surface energy of Bi. Finally, scattering was used to investigate atom-surface charge exchange at the Si(111) surface as a function of doping, a fundamental study which revealed that the bulk band gap has a strong effect on the neutralization of scattered ions, despite the work function being unchanged with added dopants.

Contents

List of Figures

List of Tables

Chapter 1

Introduction

1.1 The problem of scattering

Scattering has long been among the problems of top importance in physics. James Clerk Maxwell first investigated the issue when attempting to understand the kinetic theory of gases. The scattering of alpha particles from a gold foil was the first experimental evidence of the atomic structure we know today, where Rutherford observed that the alpha particles actually backscattered from small heavy nuclei in the foil. Quantum mechanics, upon its inception in the early 20th century, took up scattering early on, with Max Born writing in detail about it in 1926.

The problem is of such fundamental importance that stating it is incredibly simple. Scattering, in the sense it is used, is the process of two bodies nearing each other, undergoing an interaction where the momentum and energy are exchanged, and then separating again. Mainly, when thinking about this we wish to know certain things about the outgoing condition of atoms in such a collision: outgoing trajectory (or scattering angle)

and outgoing energy are the two most obvious. Additionally, we may want to know the electronic condition of the outgoing species: how many bound electrons they have, what energy state those electrons are in, what the overall spin is, etc.

Fundamentally important the problem may be, but the details of such an interaction are often intractably difficult to understand. In classical scattering, the final trajectory of two particles can be solved in quadratures once the force is known, providing the force depends only on the separation distance. This allows for a determination of the outgoing trajectories given the impact parameter, or what the separation would have been if no scattering had occurred. So long as the particles are hard spheres, or are singly charged particles that interact with the Coulomb potential, this is then solvable. However, almost no interaction involves only two particles, and in nuclear collisions the determination of the force must be made semi-empirically, for its origin is essentially quantum mechanical, depending on the interaction among all the particles in the nuclei and all the orbiting electrons. This problem is especially acute when talking about the scattering of an ion from a solid, which is composed of a huge number of atoms. Moreover, the process of charge exchange between an ion and a solid surface is a purely quantum mechanical problem, involving in principle the wave functions of all the electrons in the solid and the atom colliding with it.

For a variety of reasons, the experimental results detailed in this thesis involve low-energy alkali ions scattered from solid surfaces. This has some immediate implications for the physics involved. Using this means that

- the collisions are binary atomic collisions in nature,
- the ions penetrate at most a few atomic layers into the solid,

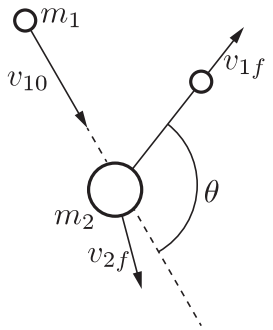

Figure 1.1: Schematic of a binary collision of two particles. The angle θ is the scattering angle.

- the electron tunneling to the ions from the solid are mainly due to resonant mechanisms.

1.1.1 Binary collision classical scattering

If the scattering process proceeds in a way that atoms essentially interact with only one partner at one time, then the outgoing energy and momentum of the ion can be found via classical mechanics. This will fail if the energies are so low that the wave function of the particle is not a localized wave packet, but apart from very slow ions, it will get the job done. This has the benefit of not requiring the specific form of the force, and only relies on energy and momentum conservation.

Suppose a particle of mass m_1 enters a region with initial velocity $\vec{v}_{10}$ and collides elastically with a particle m_2 which is initially at rest, as shown in Fig. 1.1. Suppose further that we care only about the final energy of the particle m_1. Then, one can derive the scattered energy of the projectile m_1 is[1]

[1]See Appendix A

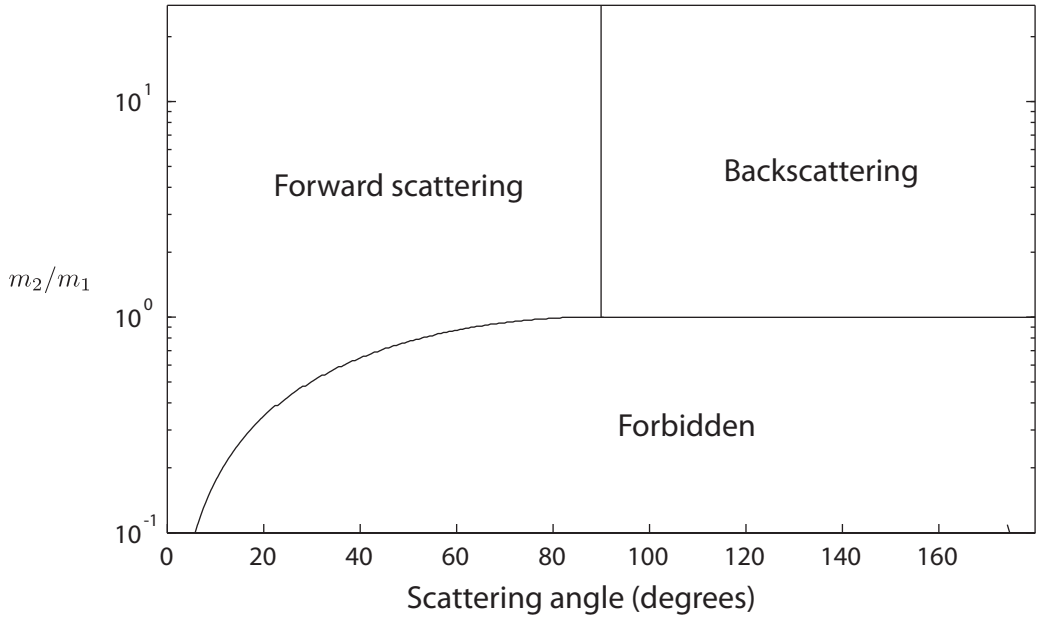

Figure 1.2: Schematic of the possible trajectories for mass m_1 scattered from m_2 at all possible scattering angles.

$$E_{1f} = E_{10}\left[\frac{\cos\theta \pm \sqrt{(m_2/m_1)^2 - \sin^2\theta}}{1 + m_2/m_1}\right]^2 . \tag{1.1}$$

This equation must have the conditions that the discriminant be positive and that the speed is positive. The constraints are summarized in Fig. 1.2. For $\mu < 1$ (the projectile heavier than the target), only forward scattering $\theta < 90°$ is allowed. For $\mu > 1$, any angle from 0 to 180° is allowed. In this thesis, we will only describe backscattering of lighter species from heavier ones (i.e. $\mu > 1$).

For a given scattering angle, incident energy, and projectile mass, which are the conditions in these experiments, it is then possible to determine the mass of target atom by analyzing the measured scattered energy.

1.1.2 Screened potentials in scattering

For an ion striking a solid surface, made up of many close-packed atoms, in general the process would be many-bodied. Even if the force between the projectile and a nearest neighbor site were to be very small, the force exerted by the target atom would be affected by the interatomic potential between the target and its nearest neighbors. This is the case unless the projectile speed is fast enough that it leaves the surface on a time scale that is short compared to the interaction of the solid atoms between themselves. In that case, the projectile is far away by the time the crystal reacts to being hit.

This is indeed the case for low-energy scattering processes, as will be seen later on in results from a complete dynamical simulation. Such a simulation is only possible once the interatomic potential is specified. The potential between atom pairs is given to a good degree of accuracy by the following empirically obtained expression:

$$U(r) = \frac{Z_1 Z_2 q^2}{4\pi\epsilon_0}\Phi(r/a_U) \tag{1.2}$$

with

$$\Phi(x) = A_1 e^{-a_1 x} + A_2 e^{a_2 x} + A_3 e^{-a_3 x} + A_4 e^{-a_4 x}, \tag{1.3}$$

and

$$a_U = \frac{0.8854 a_0}{Z_1^{0.23} + Z_2^{0.23}} \text{ Å}. \tag{1.4}$$

Z_1 and Z_2 are the atomic numbers of the atoms, a_0 is the Bohr radius 0.529 Å, and the parameters A_j and a_j are given in Table 1.1. This is the so called "Universal" or Ziegler, Biersack, and Littmark potential[1]. This form guarantees a relatively short-ranged potential, allowing the binary-collision approximation to be used in simulations. Inelastic

	A_j	a_j
1	0.1818	3.2
2	0.5099	0.9423
3	0.2802	0.4029
4	0.02817	0.2016

Table 1.1: Coefficients for the Universal potential

losses (mainly through the ion exciting plasmons) will give a slight discrepancy between the energy observed and that of Eqn. 1.1, on the order of less than 10%.[2]

Because the projectile/surface atom interaction behaves in a binary way, it is possible to get information about the topmost layer of atoms visible to the ion beam separated from the effects of lower lying atoms. This cannot be said of techniques, such as photoelectron spectroscopy, in which the electrons can realistically travel on the order of 10-20 Å, thus probing atoms in the first several layers.

1.1.3 Charge exchange in scattering processes

When an ion scatters from a surface, it can pick up an electron, leaving it neutral. In a typical experiment, an ion beam will be focused onto a specimen of interest, and the scattered species collected by a detector. While capable of measuring the energy, it is also possible to measure the neutral fraction, or the number of detected species that are neutral divided by all the detected species. If taken simultaneously, the neutral fraction of ions scattered in a single binary collision with a surface atom can be differentiated from those scattered from 2 or more surface atoms. Thus, what we measure is the neutral fraction, and hence the neutralization probability $n(z = \infty)$ of a scattered atom that was initially

[2] A better way to perform such calculations would be to use the interatomic potential predicted from density functional theory. There are some who are using this to correct the ZBL[15].

an ion. Moreover, n is measured for both single-scattering and multiple scattering.

In the present work, we are solely interested in n for single-scattering events. Since these events form a peak in the ion-scattering spectrum, we are therefore interested in the n for the single-scattering peak (SSP). The physics of neutralization of ions scattered from many atoms is not comparable, as the time scales that the latter occur during are much longer. The theory covered in the next section will not address that specifically, and some results may differ.

1.2 Theory of resonant charge exchange

Any simulation of the dynamics of scattering or sputtering has as a parameter the neutralization fraction of the outgoing ions. In secondary-ion mass spectroscopy (SIMS), detection of sputtered species is made by use of a mass spectrometer that detects ions only. Thus it is crucial to determine what fraction of the atoms scattered from the surface come off as ions, and what fraction is neutrals. The answer to this question will affect the aforementioned phenomena, in addition to physisorption models, ion implantation and sputtering models. It is also of basic scientific interest.

If we consider a simple model, the effect of assembling a lattice of atoms is to create a potential barrier for free electrons to jump out of the solid. Speaking semi-classically, then, there would only be two possibilities: either the energy of electrons in the solid is larger than the barrier, in which case we expect that all incoming ions will be neutralized by electrons, or the energy is smaller than the barrier, in which case we expect that no ions will be neutralized. Quantum mechanically, though, there is always a tunneling probability,

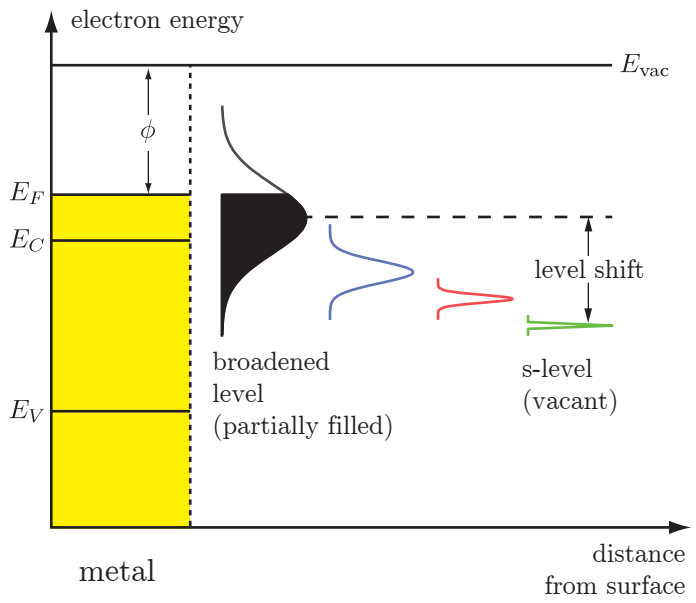

Figure 1.3: Schematic of the evolution of a vacant electron state of a low-energy ion approaching a surface. At long distances the state is narrow and below the vacuum level an amount equal to the ionization energy. As it gets closer, the level shifts up and broadens.

and it is nontrivial whenever the barrier is not enormous. Further, there are processes by which an electron of higher energy than the barrier would jump down to the atomic level, and donate the rest of the energy to another electron in the solid, ejecting it in an Auger process. Other multi-particle processes could also occur.

Despite that, the dominant charge transfer mechanism at low energy is a resonant, single electron process. The tunneling can only come from states in the crystal that are degenerate in energy with the vacant atomic state of the ion. The atomic level near the surface is hybridized with the states in the crystal, forming a state of energy width Δ_a, called a resonance.

A schematic of the process is shown in Figure 1.3. The left side of the figure

represents a metal surface's electronic structure, with filled states up to the Fermi energy E_F, where $E_F > E_C$, the conduction band edge. E_F lies at an energy ϕ, the work function, below the vacuum energy (taken to be at infinite distance, in many cases). The right side of the figure depicts what happens to the vacant s-level of an ion as it approaches the surface from right to left. Several things should be noted about this diagram. First is that the level shifts as it approaches the surface. Second is that it spreads out from a discrete energy level to a band. Third is that the ionic level becomes partially filled (shading) due to charge transfer with the surface, and that the filling happens over the energy range where the resonance and the filled states of the sample overlap. Thus we expect that the work function is going to be of prime importance to determining the final charge state. Finally, note that the sample is idealized, in that the surface is taken to be a distinct flat surface, a so-called jellium surface, and that the band structure is flat. These assumptions may not hold, but they are a good first try.

1.2.1 Level shifting

As depicted, the level shifts upward in energy as it approaches the surface. This is due to the induced image potential of a charged particle in the neighborhood of a grounded conductor. Consider the system of the positively charged ion core, an orbiting electron, and the image charges of these two in a grounded conductor. Note that even though an incoming ion has no electron, *were you to put one there*, it would have the following energy. The work done to bring in the electron against its own image charge is

$$W = \int_{\infty}^{z} \frac{q^2}{4\pi\epsilon_0} \frac{1}{(2z)^2}\, dz. \tag{1.5}$$

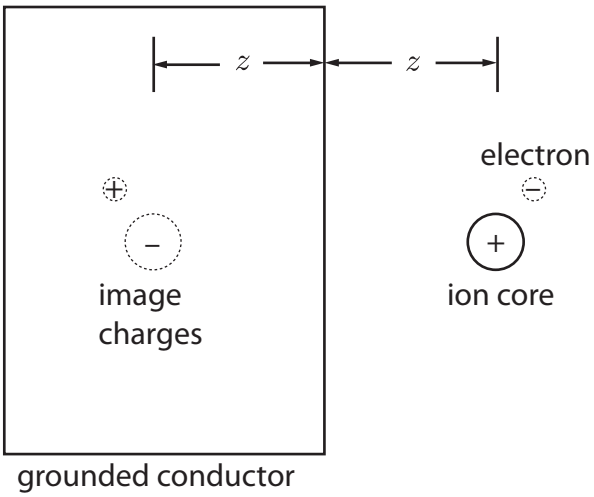

Figure 1.4: Induced image charges in a metal due to an ion.

This is in SI units. For the duration of this work, I'll use atomic units, in which energy is measured in Hartrees, charge in units of the electron charge, distances in Bohr radii, and masses in the mass of the electron. This makes $q = 1$, $1/4\pi\epsilon_0 = 1$, $\hbar = 1$, and $m_e = 1$. Then the work is

$$W = \int_{\infty}^{z} \frac{1}{4}\frac{1}{z^2}\, dz = -\frac{1}{4z}. \tag{1.6}$$

The work to bring the electron in against the image of the ion core is calculated by keeping the ion core's image fixed

$$W = -\int_{\infty}^{z} \frac{1}{(z+z')^2} dz' = \frac{1}{2z}, \tag{1.7}$$

Therefore the total energy shift due to both charges is

$$\Delta\epsilon_a = \frac{1}{4z}, \tag{1.8}$$

and is positive. That is, the energy of the electron is greater than it was at infinity, and greater than the amount it would be without the metal by $1/4z$. This is represented in Fig. 1.3 by showing the initial discrete level far away being lower than the final broadened level at short distances.

For a perfect jellium metal, this would be all that is needed to model the energy level shift. However, as the atom comes close to the metal, the value of the shifting saturates due to the atomic structure of the surface. Typically this is modeled in the literature by introducing a parameter k such that

$$\Delta\epsilon_a = \frac{1}{\sqrt{(4z)^2 + k^2}}. \tag{1.9}$$

This prevents the function from diverging unphysically, but introduces an unknown parameter which has to be determined.

1.2.2 Level broadening

If single-electron tunneling occurred from the states degenerate with the vacant level in the ion when it was not broadened, there would be precisely one value for a discrete energy, and the neutralization probability would be either 100% or 0%, depending on whether the level position was above or below the highest occupied orbital in the sample. However, the energy level is broadened in the presence of the surface, as the sample electron wave functions overlap with the vacant atomic orbital. The broadening at the distance of closest approach is on the order of 1-2 eV. If a significant number of levels overlaps with this broadened level, there will be efficient tunneling between the ion and the surface, but the final charge state of the ion will be a value intermediate to 100% and 0% whenever

this width overlaps the Fermi energy. When measured, the neutralized fraction gives the probability of neutralization, as the partially ionized state is collapsed.

The degree to which the atomic level broadens is determined primarily by two things. The first is how adiabatic the process is, with faster ions corresponding to larger energy broadening according to the uncertainty principle. The second is the density of states in the solid, where any unoccupied bands may not contribute to the overlap of wave functions.

There have been many attempts to calculate the resonance width from first principles. The main results come from Nordlander and Tully[2]. They calculated the width by treating the electron level as a collection of plane waves to form a wave packet. This "complex scaling" technique has some significant technical difficulties, as the side effect of the plane wave assumption is to create wave functions that are not square integrable and have complex energy eigenvalues. Nevertheless, the parameters for H, Li, Na, K, Rb, and Cs scattering from Al jellium surfaces were calculated. Though the results contain many parameters, the overall dependence resembles

$$\Delta_a(z) = \frac{\Delta_0}{(e^{4\alpha z} + (\Delta_0/\Delta_{\mathrm{sat}})^4 - 1)^{1/4}}, \tag{1.10}$$

where Δ_0, α, and Δ_{sat} are different for each species [3]. This has the desired properties that it decays exponentially away from the surface and saturates within 1-2 a.u. of the surface.

On the other hand, the transition rate is given by first order perturbation theory (Fermi's Golden Rule):

$$w = \frac{2\pi}{\hbar} \sum_k \rho_k |V_{ak}|^2, \tag{1.11}$$

where ρ_k is the density of states and V_{ak} is the matrix element of the perturbing potential.

Formally this is the probability per unit time of a transition from the sample to the atomic state, and is valid until the atomic state is significantly filled [4]. (Conversely, a one-to-many transition follows the same rule until the "one" state is depleted.) The inverse of w is then the time per transition, and is therefore the lifetime, τ of the unoccupied level. By the uncertainty principle

$$\Delta_a \tau \cong \hbar \tag{1.12}$$

or, to first order,

$$\Delta_a = \hbar w = 2\pi \sum_k \rho_k |V_{ak}|^2. \tag{1.13}$$

We thus have two independent expressions for the broadened level width. (Note that the literature often speaks of half-widths, and so omits the factor of 2.)

It should be stressed that this treatment is not meant to be taken literally. There is no stationary state with width Δ_a. A more formal explanation is that if some interaction couples the atomic and metal states, then neither is a stationary state of the Hamiltonian. However, a stationary state approximate to the actual state is one that is broadened (and shifted), and is resonant between the atom and metal state. The uncertainty principle then implies a finite band width for the atomic level. In practice, we view this as tunneling into a broadened state [5].

1.2.3 Perpendicular and parallel velocity

The time interval over which the charge exchange occurs is dictated by the component of the classical velocity (Eqn. A.7) that is perpendicular to the surface. As $v_\perp$ increases, it is expected that the lifetime decreases and hence the broadening increases. This leads to fewer neutrals in the case that the energy level of the resonance passes through the Fermi

energy on approach. The more slowly the atom moves, and hence how adiabatic the process is, the more neutrals are expected.

Two experimental approaches can be taken to affect this. The first is to just decrease the energy of the incoming ions, which can be experimentally quite difficult due to the problems of focusing a slow beam of ions, and due to the low detection efficiency at lower energies. The other method is to change the emission angle toward the detector, which is typically very easy. However, there are two complications with this method. The first is that if the local electrostatic potential (LEP) is nonuniform (i.e. the jellium model breaks down), then the energy shifting and broadening will be affected by this. As such, it is possible for the observed neutral fraction to go down as $v_\perp$ is increased. We especially expect this to happen anytime the surface is made up of two species, given the relative electronegativities of bonded species, and was found to be significant in Na scattered from CeO_2[6]. The second is the effect of parallel velocity, most relevant in collisions that are very grazing. The number of electrons in resonance with the ion can be influenced by the coordinate transformation, and in such cases such as the formation of H^- from H^+ scattered from Cs/W(110), the above description is inadequate [7].

The fact that the LEP affects the neutral fraction, though, means that studies of this potential may be undertaken with low-energy ion scattering. One can probe the nonuniformity of the LEP by changing the exit angle of the ions scattered from, say, an oxide surface, and looking for the hallmark of decreasing neutral fraction with increasing angle. This can then be quantified by density-functional theory determinations of the LEP, which will indicate a certain shift in potential from normal incidence.

1.2.4 Induced work function shifts

According to the schematic figure of the RCT mechanism, changing the work function should have significant effect, particularly when the change is an appreciable fraction of the resonance width. In ion-scattering experiments of this type, the work function is normally changed by adsorption of ionic species that either donate or accept an electron to the surface. To lower the work function, an alkali metal such as potassium could be used, as it accepts an electron. To raise the work function, a halogen such as iodine, which donates an electron, is deposited. A complication of this, however, is that for significant coverages of an adatom, the charge imbalance can create an inhomogeneous potential at the surface[8]. As such, some sites are not equal to others as regards the charge exchange. At that point, the band approximation mentioned earlier is not valid, and does not accurately predict the neutralization probability[9].

1.2.5 Freezing distance and Memory loss

The time evolution of the expectation value of the atomic level occupancy can be written in terms of the broadened level Δ according to the differential equation[12]

$$\frac{d}{dt}\langle n_a(t)\rangle = \Delta(z)[N(z,T) - \langle n_a(t)\rangle], \tag{1.14}$$

where N is the equilibrium charge state

$$N(z) = \int_{-\infty}^{\infty} dE\, \rho(E) f(E,T) \tag{1.15}$$

and $f(E,T)$ is the Fermi-Dirac distribution. It is then possible to show [13] that so long as the ionization probability depends only on the outgoing velocity (and not the incoming

velocity as well), $\langle n_a(t) \rangle$ is sharply peaked at a distance

$$z^* = \alpha^{-1} \ln(\Delta_0 / \alpha v_\perp) \tag{1.16}$$

called the freezing distance. For heavier species such as sodium, this value represents a characteristic length that the charge state is ostensibly determined at this distance alone. Simply evaluate

$$\langle n_a(t) \rangle \approx N(z^*). \tag{1.17}$$

At $T = 0$, it is possible to integrate N directly to obtain

$$N(z) = \frac{1}{2} + (1/\pi) \tan^{-1}[2(I - \Delta E(z) - \phi)/\Delta(z)] \tag{1.18}$$

where I is the ionization potential at infinity, ΔE is the image potential shift, and ϕ is the work function. Therefore, the neutralization probability has an $\tan^{-1}$ dependence as, for instance, ϕ is changed.

As mentioned before, the existence of a characteristic freezing distance depends on the ion experiencing a loss of memory as to its initial state, so that the neutralization probability depends only on the outgoing velocity. This will happen any time that the scattered ion is not very swift. In that case, during the initial trajectory the term in the master equation (1.14) that depends on the initial charge state decays by a factor of 1000[14]. This is not to say that memory loss happens in every case. Indeed, the model developed in Chapter 4 retains slight memory effect, due to the relatively quick speed of scattered Li. Nevertheless, the idea of a freezing distance has great utility when explaining the interactions of, e.g., Na ions scattered from metal surfaces.

1.3 Further avenues of investigation in resonant charge transfer

The preceding section on neutralization highlights the fact that ion scattering neutralization studies are almost always done on clean metal single-crystal surfaces. While metals are the simplest to understand from a band theory outlook, they are far from the only material of interest in surface science and solid state physics.

Oxides, in particular, are ubiquitous, and understanding how the RCT model deals with them is of both fundamental and practical importance. Previous studies of the neutralization from oxide surfaces are rare. Measurements have been conducted for TiO_2, but only as a support for metal nanoclusters. The surface of ceria was investigated by our lab [6], resulting in compelling behavior as angle and surface work function was varied. Because many novel materials are oxides, or at least made up of two different atomic species, the situation is ripe for ion scattering studies.

Another material in which the charge exchange at the surface is poorly characterized is Si, the material used in nearly every ultra large scale integration processes. Doping is known to have an effect on several fabrication techniques, but heretofore no studies have been conducted looking at the effect of ion scattering neutralization from the Si surface as a function of doping.

Both oxides and Si have a major complication when it comes to RCT analysis, which is the presence of a band gap. The effect of a band gap on surface charge exchange at low energies is poorly understood. The RCT model detailed above depends almost entirely on the surface work function, but the work function is determined only by the

highest occupied orbital (the Fermi energy), and not on the density of states. While some preliminary theoretical and experimental work on surface band gaps (due to surface states) has been conducted (see Chapter 4), there has been surprisingly little work on the effect of bulk band gaps.

As such, in this thesis we focus on neutralization of scattered ions from an oxide material and a semiconductor. The oxide material ($Bi_2Sr_2CaCu_2O_8$) demonstrates interesting properties when molecules of different types are adsorbed on it, where modifying the work function unexpectedly does not necessarily effect the neutral fraction. With Si, the same observation may be made—that the work function for differently doped samples is identical, the neutral fraction is still changed. Each of these cases represents a small but explainable divergence from the standard RCT model. As such, these studies have helped push the boundaries of the analysis of surface charge exchange beyond metals.

1.4 Low-energy ion scattering experimental design

The experimental apparatus necessary for determination of the energy distribution and charge state of low-energy ions scattered from surfaces is relatively straightforward, though unconventional. The usual method for determination of the energy distribution of the ions, in ion-scattering spectroscopy (ISS), is to use an electrostatic analyzer. This, naturally, relies on the outgoing species being ionized, and is thus not suitable for determination of charge state concentration. Instead, it behooves us to measure the time-of-flight for each species, and utilize a detector that responds equally to ions or neutrals.

In order to measure the time-of-flight, an array of micro-channel plates with no

electrostatic filter may be used. This has the desired property of responding equally to ions and neutrals. It also responds more efficiently to higher energy ions, thus reducing any background signal of ions. The method relies on the ability to pulse the ion beam with a pulse width that is lower than or nearly the desired time resolution. Once achieved, the time between counts on the detector and pulses on the ion source gives the time-of-flight. For low-energy ions, the time-of-flight is on the order of 1 μs, and a resolution of 0.1 μs is desired, so a beam of 1-3 keV ions must be able to be pulsed with a width of on the order of 10-100 ns. This can be achieved relatively easily by scanning the beam with deflection plates so that it passes by a suitably small aperture in a time of about 20 ns.

Adding charge resolution to this setup is just a matter of filtering the ions out of the scattered beam by way of a set of deflection plates. Then the counts under the single-scattering peak may be determined for the total yield (when the deflection plates are at ground) and for the neutral yield (when the plates have 300 V across them). The quotient of these two areas is the neutral fraction, and hence a measure of the neutralization probability.

A schematic of the experimental apparatus is depicted in Fig. 1.5. All experiments need to be undertaken in ultra-high vacuum ($< 5 \times 10^{-10}$ torr), due to the extreme surface sensitivity of the technique and the need to keep the surface clean. The scattering angle is determined by the angle between the position of the ion source mounting and the detector mounting, which is fixed in these experiments. However, by rotating the sample holder in the plane of the page, the incident and emission angles can be changed easily, though not independently.

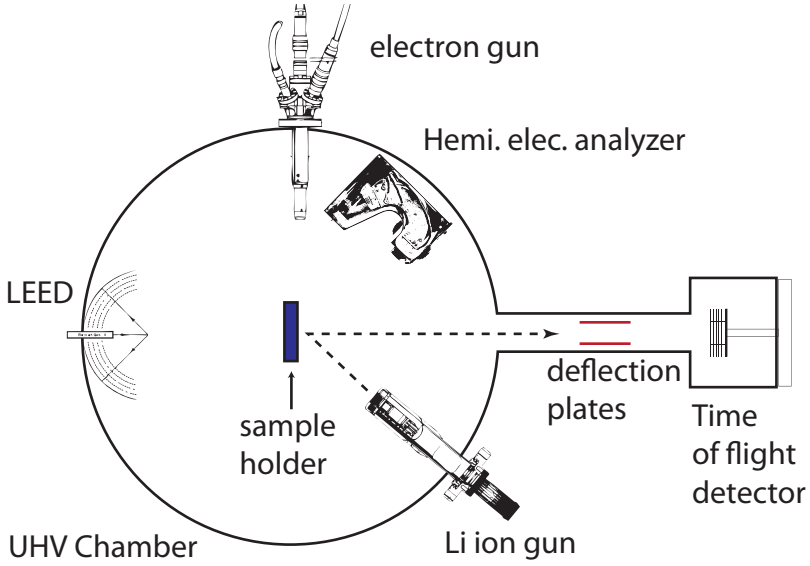

Figure 1.5: Schematic of the experimental apparatus for TOF-LEIS.

A typical LEIS-TOF spectrum is displayed in Fig. 1.6. Time here is plotted in reverse, so that the positive horizontal axis is in the direction of increasing scattered energy. The shaded areas are one example of the determination of neutral fraction.

1.4.1 Data analysis

There are several options to obtain a neutral fraction from the TOF spectrum. The simplest would be to compare the peak heights of the total and neutral spectra at the time value of the single-scattering peak of interest. This works perfectly well for spectra in which the background of the scan is a time-independent static noise. It is not, however, satisfactory in samples with a large background that has some structure. A better option in that case is to set the ostensible limits of the peak, and find the area of the peak while subtracting the background. That is, the effective area under the SSP for the total yield

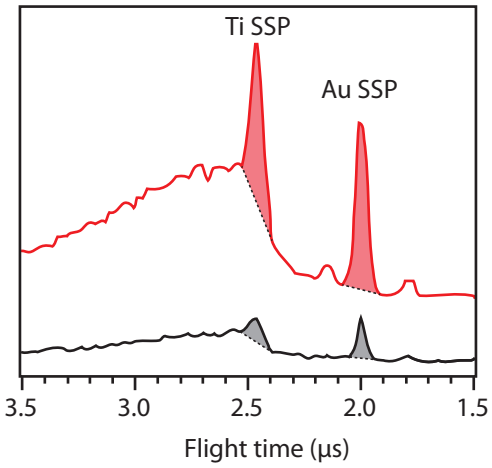

Figure 1.6: LEIS-TOF spectrum of Li scattered from Au on TiO_2. Taken from [10].

(in counts) is

$$A_{\text{tot}} = \frac{1}{\Delta t}\left(\left[\int_{t_1}^{t_2} T(t)\,dt\right] - \left[\frac{T(t_2)+T(t_1)}{2}(t_2 - t_1)\right]\right), \tag{1.19}$$

for total yield spectrum $T(t)$, and peak limits t_1 and t_2. The area is divided by the step size Δt of the spectrum so that one is operating in pure numbers (counts) again. Two notes are of interest. One, the integration of the first term should *not* be performed as a simple sum, but instead should employ at least trapezoidal integration. Two, the background is assumed here to be a trapezoid; if the background is known to be nonlinear, one could use a fitting algorithm to remove the background instead. The neutral fraction is calculated simply by $n = A_{\text{neu}}/A_{\text{tot}}$.

1.4.2 Error estimates

A TOF experiment is akin to any other nuclear experiment where the number of trials is huge compared with the number of successes. Typically, an experiment requires

a number of measurements, and the standard deviation of this distribution is calculated to give an error estimate. We can get around this because our incident current is on the order of 10^6 ions per second (0.1-0.5 pA) and the number of counts that we find in our peak (as found in Eqn. 1.19) is on the order of 10 or perhaps 100 per second. In the terms of probability theory, it is a binomial distribution with a large number of total trials N, and a low probability of success p. As a result, the standard deviation in our total peak area is simply $\sqrt{A_{\text{tot}}}$. A proof of this amazing result is given in the appendix.

After finding A_{tot} and A_{neu} and corresponding uncertainties $\sqrt{A_{\text{tot}}}$ and $\sqrt{A_{\text{neu}}}$, one can calculate the uncertainty in the quotient by[11]

$$\Delta n = n\left(\frac{\sqrt{A_{\text{tot}}}}{A_{\text{tot}}} + \frac{\sqrt{A_{\text{neu}}}}{A_{\text{neu}}}\right). \tag{1.20}$$

Bibliography

[1] J. F. Ziegler, Ion Implantation - Science and Technology, Ion Implantation Technology Co., 1996.

[2] P. Nordlander, J. C. Tully, Phys. Rev. B **42**, 9 (1990).

[3] A. V. Onufriev and J. B. Marston, Phys. Rev. B **53**, 20 (1996).

[4] Leonard I. Schiff, Quantum Mechanics, McGraw Hill, New York, 1949, pg 193

[5] This issue is discussed at some length by J.W. Gadzuk, Surf. Sci. **6** (1967), 133-158.

[6] J. A. Yarmoff and G. F. Liu, Surf. Sci. **600**, 2293 (2006).

[7] H. Winter and R. Zimny, in: Coherence in Atomic Collision Physics, eds. H.J. Beyer, K. Blum and R. Hippler (Plenum, New York, 1988) p. 283.

[8] C.B. Weare, J.A. Yarmoff, Surface Science **348** (1996), 359-369.

[9] A.G. Borisov, G.E. Makhmetov, D. Teillet-Billy, J.P. Gauyacq, Surface Science **375** (1997) L367-L374.

[10] G.F. Liu, Z. Sroubek, P. Karmakar, J.A. Yarmoff, J. Chem. Phys. **125**, 054715 (2006).

[11] J.R. Taylor, Introduction to Error Analysis, Univ. Science Books, 1982, page 48.

[12] J. Los and J.J.C. Geerlings, Phys. Rep. **190**, 3 (1990).

[13] B. Rasser, J.N.M. van Wunnik and J. Los, Surf. Sci. **118**, 679 (1982).

[14] R. Brako and D.M. Newns, Surf. Sci. **108**, 253 (1981).

[15] M.A. Karolewski, Nucl. Inst. Meth. Phys. Res. B, **243**, 43 (2006).

Chapter 2

Adsorption of Iodine and Potassium on $Bi_2Sr_2CaCu_2O_{8+\delta}$ Investigated by Low Energy Alkali Ion Scattering

2.1 Introduction

The high-temperature superconducting cuprates are oxides with complex layered structures. Surface studies of these materials are valuable, as they allow for the superconducting cuprate layer to be probed in a detailed way, especially with regard to formation of the paired carriers. One of the materials most often used for surface studies is

This chapter contains material published in R.D. Gann, J.X. Cao, R.Q. Wu, Jinsheng Wen, Zhijun Xu, G.D. Gu, and J.A. Yarmoff, "Adsorption of iodine and potassium on $Bi_2Sr_2CaCu_2O_{8+\delta}$ investigated by low-energy alkali-ion scattering", Phys. Rev. B **81**, 035418 (2010).

$Bi_2Sr_2CaCu_2O_8$ (Bi-2212), owing to the ease in cleaving the samples in ultra-high vacuum (UHV), which produces clean terraces of BiO. Previous studies, however, have been mainly confined to scanning probe microscopy and photoemission [1, 2, 3]. Reports of ion beam experiments on cuprate materials that do exist have either focused on disorder-induced changes to the critical current [4], rather than surface physical and electronic structure, or have been on surfaces that are much less ordered than cleaved Bi-2212, such as $YBa_2Cu_3O_{7-x}$ [5].

Low-energy ion scattering (LEIS) can provide complementary information to other surface analysis techniques [6]. The method is extremely surface sensitive, as the spectra display peaks resulting from single binary collisions between incident ions and the outermost surface atoms. LEIS can be used to determine composition, surface structure, and, under certain conditions, the local electrostatic potential (LEP). Time-of-flight spectroscopy with alkali ions, in particular, can simultaneously measure the mass of the surface atoms and the LEP [7]. An incoming alkali ion has an ionization level typically between 4.3 and 5.4 eV, which is commensurate with the work function at the surfaces of many materials. As the ion approaches a surface, this ionization level shifts due to the image potential, such that it passes the Fermi energy. The charge transfer process is non-adiabatic, and the charge distribution is determined along the outgoing trajectory as the projectile passes through an effective "freezing distance". This makes the neutralization probability of scattered ions a sensitive measure of the local potential just above the scattering site. Results from this method can be interpreted within the well-established theoretical framework of resonant-charge transfer (RCT), which includes both analytical formulae and numerical calculations [8]. Extensive prior experimental work with alkali ion scattering from metals, along with some work done with simple oxide surfaces (e.g. CeO_2, TiO_2), provides the context for

interpreting the results, and allows some extension of the theory to non-metals. We note here that it is not possible, for reasons discussed below, to see directly the effect on neutralization by paired carriers using this technique.

The RCT framework helps to determine the kinds of measurements to perform when characterizing a system with low energy alkali ion neutralization. Theoretical work using a semi-classical approach based on the Anderson Hamiltonian [8, 9] shows that the incoming vacant level broadens in energy, and the expectation value of the neutralization probability far from the surface, $\langle n(z=\infty)\rangle$, depends principally on the so-called freezing distance, $z^* = \ln(2\Delta_0/\alpha v_\perp)/\alpha$, where $v_\perp$ is the perpendicular component of the outgoing velocity. This is because the tunneling rate is peaked at this distance, constituting a majority of the tunneling involved in the neutralization process. Because this expression contains $v_\perp$, a strong dependence of neutralization on the outgoing perpendicular velocity is expected, which can be realized either through changing the incident ion energy or through changing the exit angle of the scattered ions. At a fixed energy and exit angle, the neutralization is then sensitive to changes in the surface LEP.

This chapter resent several related measurements in which LEIS was used to investigate the surface of Bi-2212. Results show an angular dependence of the neutralization probability in scattering from Bi that reveals an inhomogeneous potential similar to that of other oxide surfaces. Adsorbed ionic species, potassium and iodine, reside in different bonding sites, significantly influencing the neutral fraction of Na scattered from Bi in the presence of I, but not with K. This result is in agreement with the high-symmetry adsorption site and local potential that are predicted by density functional theory (DFT). In addition, DFT enables an experimental estimate of the freezing distance. We note that, to

our knowledge, this is the first time that the RCT model of neutralization in LEIS has been interpreted using DFT

2.2 Experimental Procedure

Low-energy alkali ion scattering experiments were performed in a custom-built UHV chamber. The base pressure was typically 3×10^{-10} torr. Details of the surface analysis equipment and time-of-flight (TOF) instrumentation are described elsewhere [10]. Briefly, a pulsed beam of Na^+ ions is focused onto the sample, and the time differences between the ion pulses and counts recorded on a micro-channel plate detector are collected, giving the TOF spectrum. Although the instrument is capable of producing pulse widths as short as 20 ns, a pulse width of ∼200 ns was used in this study, which resulted in a large, well-resolved scattered particle peak with good statistics. The detector leg is equipped with deflection plates capable of filtering scattered ions, so that the system can alternately measure the total yield and the yield of neutrals only. In order to account for any long-term drifts in incident beam current during this period, data were collected by cycling between totals and neutrals every 60 seconds for a scan that took about 30 minutes in total. Although the scattering angle is fixed at 150°, the sample can be rotated to change the angle between the surface normal and the detector, and hence change the perpendicular component of the velocity of the exiting projectile.

Float-zone grown single crystals of $Bi_2Sr_2CaCu_2O_{8+\delta}$ were cleaved in situ at low temperature by a method detailed elsewhere [11]. Experiments were conducted over the course of a few hours while maintaining the sample at low temperature, although no qual-

itative difference was observed in the spectra when the samples were heated to room temperature. Maintaining low temperature while taking data was done so that results were comparable to previous scanning tunneling microscopy (STM) work, where almost all samples were cleaved at low temperature and kept cold (c.f. [1, 2, 3]). Damage due to the incident alkali ion beam is of concern, particularly in experiments where alkalis themselves are the adsorbate, so the total fluence on any one part of the sample was limited to less than 1 ion per 100 surface atoms. Data were collected with incident energies from 800-3000 eV and several emission angles.

Potassium was deposited from a well-degassed SAES getter, while iodine was deposited from a solid-state AgI electrochemical cell that emits I_2 molecules [12]. X-ray photoelectron spectroscopy confirmed the presence of I on the sample after deposition. The change in surface work function upon deposition was determined via the shift of the low energy secondary electron cutoff. Secondary electrons were produced by bombarding the sample with a 200 eV electron beam, and the cutoff was measured using a hemispherical electrostatic analyzer (Comstock) [13]. The incident electron current during this measurement was approximately 200 nA, and no appreciable changes in the spectra were observed due to electron beam damage during a scan of about 60 seconds. The sample was exposed to the K or I adsorbates until there was no further change to the work function, thus indicating that saturation coverage was reached.

2.3 Results and Discussion

2.3.1 Time-of-flight results for a pristine Bi-2212 surface

Figure 2.1 displays representative charge-resolved TOF ion scattering spectra of 2 keV Na^+ collected from the as-cleaved Bi-2212 surface. The sharp single-scattering peak (SSP) represents a classical binary collision of Na^+ with a surface Bi atom. No single scattering from oxygen in the outermost layer occurs, since O has a lower mass than the projectile. Single-scattering events from the other constituents of the material are not observed on a virgin surface, presumably due to their being positioned below the surface atoms, and as such being completely shadowed by surface Bi or O. The broad background at longer flight times corresponds to projectiles that have escaped the surface after suffering multiple collisions. This result confirms that the cleaved Bi-2212 surface is terminated by a BiO plane (illustrated in the inset to Fig. 2.1), where weak van der Waals binding between the adjacent BiO layers ensures that samples almost always cleave at this interface [14]. The absence of scattering from the deeper lying metal atoms was consistent with a computation of the shadow cones using the empirical formula of Ref. [15] and assuming a simple bulk termination of the structure.

The shaded regions in Fig. 2.1 illustrate how the area of the SSP was typically resolved from that of the multiple-scattering background. The area of the neutral yield SSP divided by the area of the total yield SSP gives the neutral fraction for a given sample preparation, incident ion energy and orientation. In determining the error associated with each neutral fraction, both the shot noise, via the square root of the number of integrated counts, and the uncertainty in the time limits of integration are taken into account. The

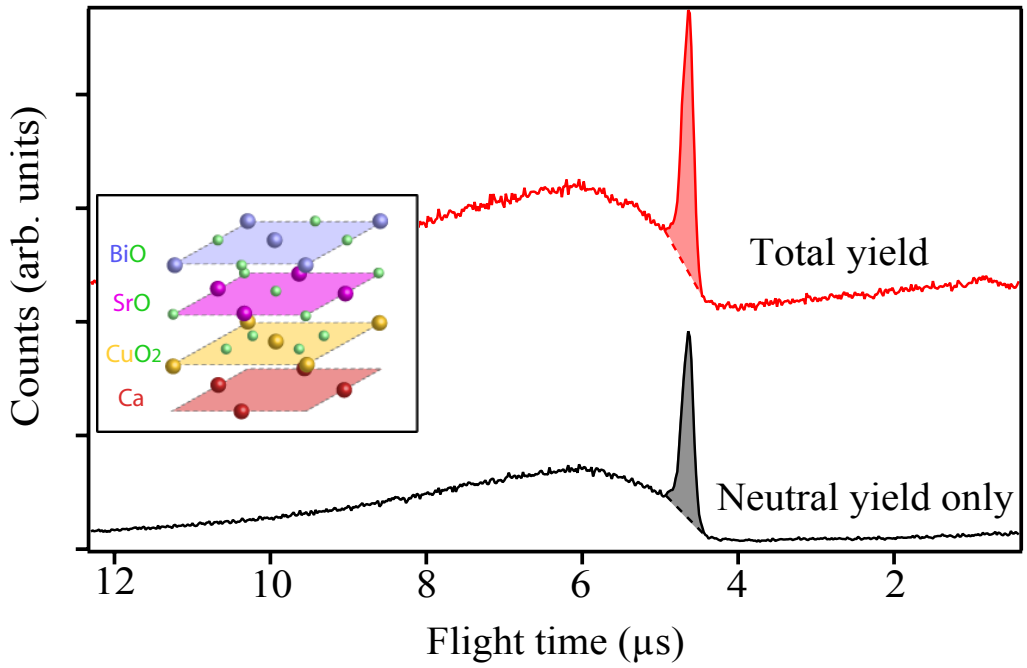

Figure 2.1: Time-of-flight spectra of 2 keV Na^+ scattered from Bi-2212 cleaved at 82 K, which shows a pronounced single-scattering peak from Bi. Because of the relatively large background, we employ a background subtraction scheme to calculate the neutralization probability, as shown by the shaded area. Inset: schematic of the first four layers of Bi-2212 (one inversion).

latter is accounted for by recalculating the neutral fraction at slightly different limits of integration, both for the lower and upper limits, and taking the largest and smallest values of the neutral fraction calculated. This is done because the chosen boundaries of the SSP are set visually and are thus somewhat arbitrary. Although variations in beam current are not directly accounted for in the error estimate, totals and neutrals were collected alternatively during each scan, as described above, and the beam current is typically quite stable over the duration of one scan.

Figure 2.2 shows neutral fractions obtained from a virgin surface at low temperature as a function of emission angle, measured from the surface normal, for three different

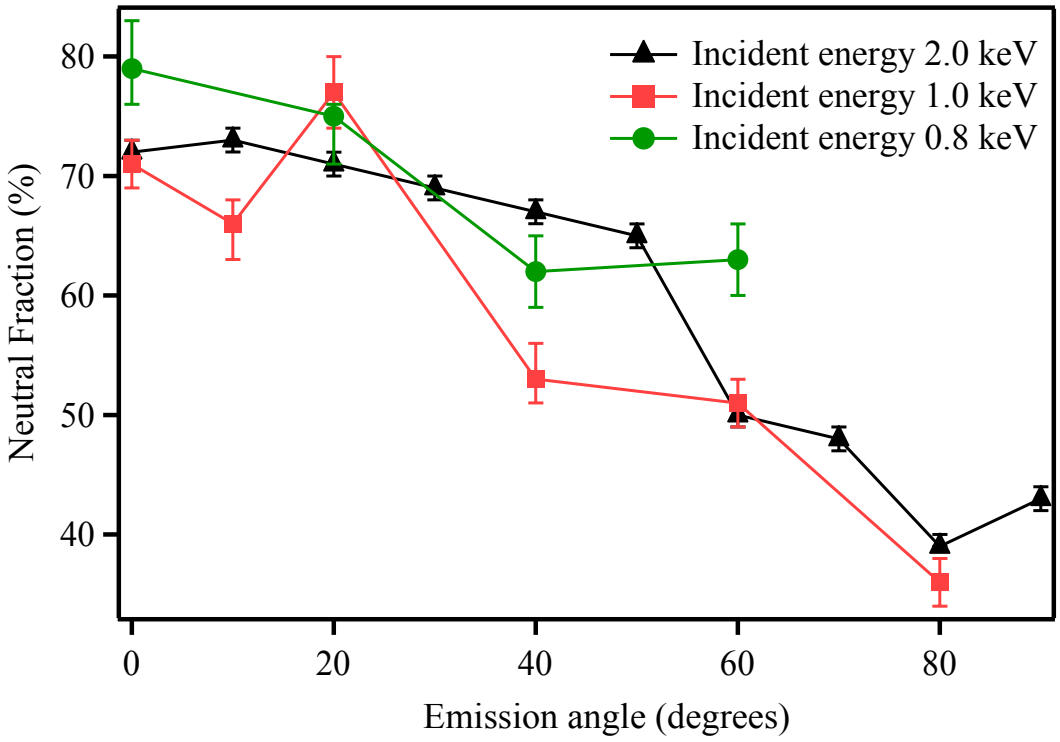

Figure 2.2: Neutralization versus emission angle for three different incident energies, along with error bars (1 std. dev.). There is at most a marginal dependence on incident energy, with a downward trend as emission angle is increased (corresponding with a lower perpendicular velocity). Note that a pronounced change is not necessarily expected when the energy is varied, as the range of energies for which reliable data could be collected in this case was only within the small range from about 1-2 keV.

incident energies. The three energies show identical neutral fractions, within the error bars of the measurement, as the energy range for which good spectra could be obtained is relatively small. Neutralization decreases for larger exit angles.

Note that a significant difference in neutralization was not observed when the data were collected at $T < T_c$ versus $T > T_c$. Although high-T_c materials have an emergent pairing gap at temperatures somewhat above Tc and a condensing of pairs below T_c, the

scale of this energy change makes it difficult to measure changes to the surface on that order with the LEIS technique, as the energy of the tunneling states would shift on the order of only 1 meV. Typical error in the neutralization measurement is ∼1-5%, and a cursory inspection of the literature suggests that work function shifts need to be at least 0.1 eV to produce an altered neutral fraction outside of these error bars (see, e.g., Ref. [16]). Another difference expected when heating is that the work function should change. Saito *et al.* found the work function of Bi-2212 to be 4.849 eV at 85 K, and that it rose by about 0.1 eV when the sample was allowed to warm to 130 K [17]. This is within the detection threshold in a normal metal: the electron tunneling probability depends strongly on the difference between the ionization level and the work function of the material when the electrostatic potential is homogenous. Although we did not monitor the work function while heating, if we assume that the overall work function does indeed change upon heating as reported, this suggests that the normally emitted Na probes only a local part of the electrostatic potential, namely that around the Bi atoms themselves, and that this potential is unaffected by annealing. The effect of annealing may involve diffusion of oxygen from the bulk to fill in vacancy defects at the surface, which would be consistent both with the positive change in the work function and the insensitivity of the Bi SSP neutral fraction to the temperature.

It is interesting to compare the dependence in parameter space of LEIS from Bi-2212 with that of a normal metal. In the case of a metal, the neutralization probability depends principally on the component of velocity perpendicular to the sample, $v_\perp$, along the outward trajectory. In particular, neutralization normally increases as $1/v_\perp$, and hence increases with emission angle when the surface has a homogeneous potential [18]. As seen in Fig. 2.2, however, the opposite appears to be the case with Bi-2212.

Previous alkali ion scattering studies of CeO_2 surfaces performed in our laboratory have produced a similar reduction in neutral fraction at more grazing angles, which were interpreted as resulting from the inhomogeneous potential associated with an ionic oxide surface [19]. At electropositive sites on a surface, the local work function would be reduced, pushing the Fermi energy up relative to the ionization level and leading to increased neutralization of scattered alkalis. Conversely, at electronegative sites the work function is increased, pushing the Fermi energy down and leading to a decrease in neutralization. Thus, the neutralization has a more complex trajectory-dependent behavior when the surface potential is inhomogeneous. In the case of CeO_2, the reduction in neutral fraction as the trajectories become more grazing was ascribed to the local distribution of charge at the surface-the negatively charged oxygen atoms sit higher up at the surface than the positively charged Ce atoms, so that the ions scattered from the Ce sites pass by the electronegative O atoms as they exit the surface at more grazing angles. Hence, the neutralization decreases with angle.

Unlike CeO_2, the positive Bi and negative O surface atoms in Bi-2212 are nominally at the same height, with at most a small wavy periodicity of 0.03 nm along the c-axis [20]. It is then expected that as the emission angle is increased, the ions scattered from Bi would pass near the negatively charged oxygen sites along the outgoing trajectory, but not as close as would an ion scattered from Ce in CeO_2. Consequently, the result for Bi-2212 should be qualitatively the same as on the ceria surface, but less pronounced, and that is indeed what is seen. In CeO_2, the neutralization probability changed from 100% down to about 40% as the trajectories became more grazing [19], whereas here the change is more modest, from perhaps 70% to 40%.

2.3.2 Adsorption

2.3.2.1 Results

Figure 2.3 shows the effects that alkali (K) and a halogen (I) adatoms have on the neutralization of Na^+ ions scattered from the Bi sites into the surface normal direction. The work function is decreased by K adsorption and increased by I, as would be expected from a simple consideration of the charge of the species. Both adsorbates saturate the surface, presumably because there are a limited number of available sites (i.e., they follow the Langmuir model).

Although a large work function change is observed as K is deposited, surprisingly there is no significant change in the scattered Na^+ neutral fraction for scattering from Bi at any K coverage. When I is deposited on the surface, however, the neutralization probability changes significantly with even a small deposition. Taking into account the total adsorbate flux and chamber geometry, it is estimated that for the points with elevated work function, the I_2 exposures are such that each surface atom has been hit by approximately one iodine molecule. With this exposure, the total adatom coverage is likely to be well below 1 ML since the sticking coefficient should be much less than unity [12]. This exposure decreased the neutral fraction from roughly 70% to 50%, which is well outside of the error bars.

Typically, the projectile-surface electronic system can be modeled by assuming that the incoming ionization level is shifted up by an image potential, so that it crosses the Fermi level along the outgoing trajectory. As such, when the work function is significantly altered by the introduction of adsorbates, the neutralization is also strongly affected (at least in the limit of a homogeneous potential), with a negatively charged adsorbate expected to

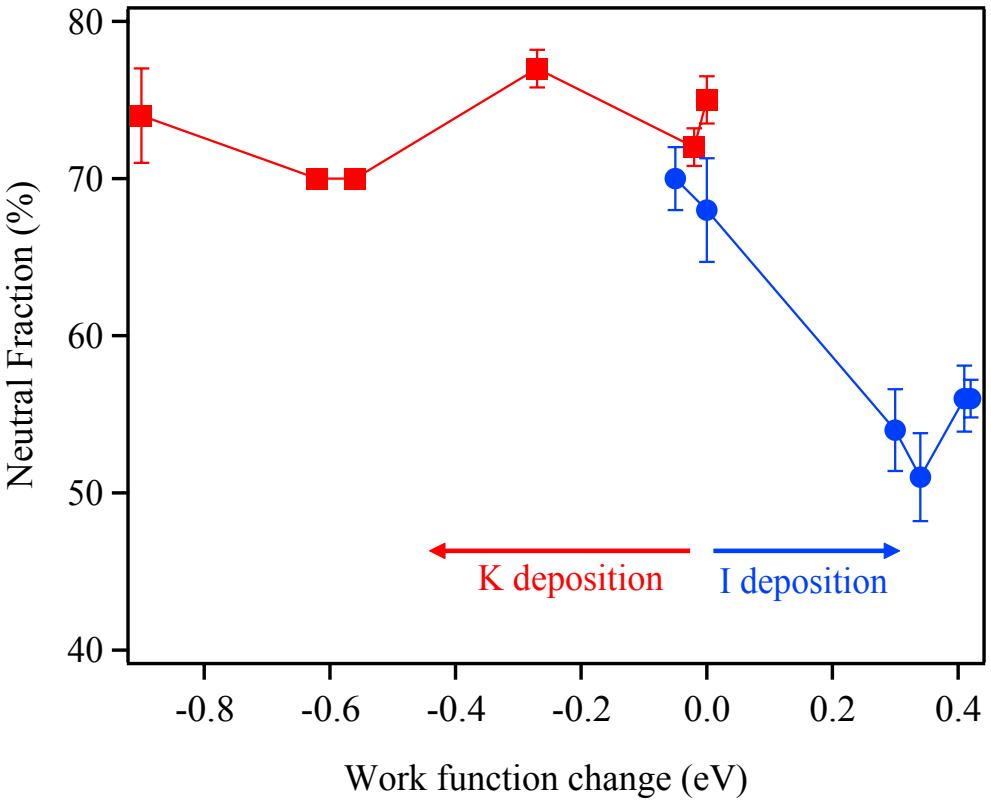

Figure 2.3: The neutralization of scattered 2 keV Na^+ shown with respect to the work function changes that are induced by adsorption of potassium (positively charged, which decreases the work function) and iodine (negatively charged, which increases the work function).

increase the work function and thus decrease the neutralization. To observe any change in work function at all implies that a dipole exists somewhere near the surface, as the otherwise grounded sample has no excess charge. If an adatom adsorbs primarily, or exclusively, to a particular site in the unit cell, the expectation is that the potential will be localized and inhomogeneous. Although the effect of this bonding is reflected in the angular dependence, in trying to determine the local potential the interpretation becomes quite complex. A better way to determine the potential would be to observe how/if the neutralization is altered due to adsorption and compare this to predictions made of the potential for different adsorption scenarios. In the next section we discuss how density functional theory helps explain our findings

2.3.2.2 Density functional theory

The local work function near the surface of Bi-2212 was obtained by DFT calculations with the Vienna ab initio simulation package (VASP) using the generalized gradient approximation and employing the PW91 functional [21]. An energy cutoff of 350 eV was chosen for the basis set and the projector augmented wave (PAW) pseudopotential was used for the description of electron-ion interactions. A slab model with 8 atomic layers in a 3x3 supercell of Bi (rotated 45° from the inset of Fig. 2.1) was used as the clean surface. The central CuO and CaO layers were fixed at their bulk positions, while the topmost BiO and SrO layers were fully relaxed with the criterion that the maximum force on the atoms must be smaller than 0.01 eV/Å.

Several high-symmetry positions, such as top-site, bridge-site and hollow-site, were chosen as test sites for the adsorbates, and the crystal was allowed to relax to its lowest

	Iodine	Potassium
	Binding energy (eV)	
Bi-top	−0.70	0.40
O-top	−0.71	−0.09
Bridge	−1.62	−0.69
Hollow	−1.90	−0.85

Table 2.1: Electrostatic energy associated with the adsorption of atoms for iodine and potassium atoms above a Bi-2212 surface for various trial sites, as calculated by DFT.

energy arrangement. The resulting binding energies are displayed in Table 2.1. They show that atomic iodine has its lowest-energy starting at a hollow-site, relaxing to a position with a binding-energy of −1.90 eV, while potassium, beginning at the same hollow site, relaxes somewhat far away with a minimum energy of −0.85 eV. After finding the arrangement of least energy, the LEP was calculated with the atom in its fully relaxed position.

The real-space relaxed surface structures that resulted from this calculation are shown in the top panels of Fig. 2.4. K significantly perturbs the crystal structure, and is predicted to adsorb nearly on top of an O site somewhat far from the nearest two Bi neighbors. This site would place the positively charged K adatom nearly equidistant from the positively charged Bi sites. Iodine, on the other hand, is expected to adsorb on a hollow site 3 Å above the surface, forming a nearly regular pyramid with the nearest Bi and O. These predictions are consistent with an intuitive chemical picture, since the p level of the iodine atom can bond covalently with several sites, while the s level of the K would more likely form an ionic bond with O^{2-}.

Contour plots of the calculated local work function for Bi-2212 with K and I adsorbates are shown in the lower panels of Fig. 2.4, at distances of 1, 2, and 3 Å above the plane of the surface Bi atoms. Contour plots at 1 Å show virtually no effect from

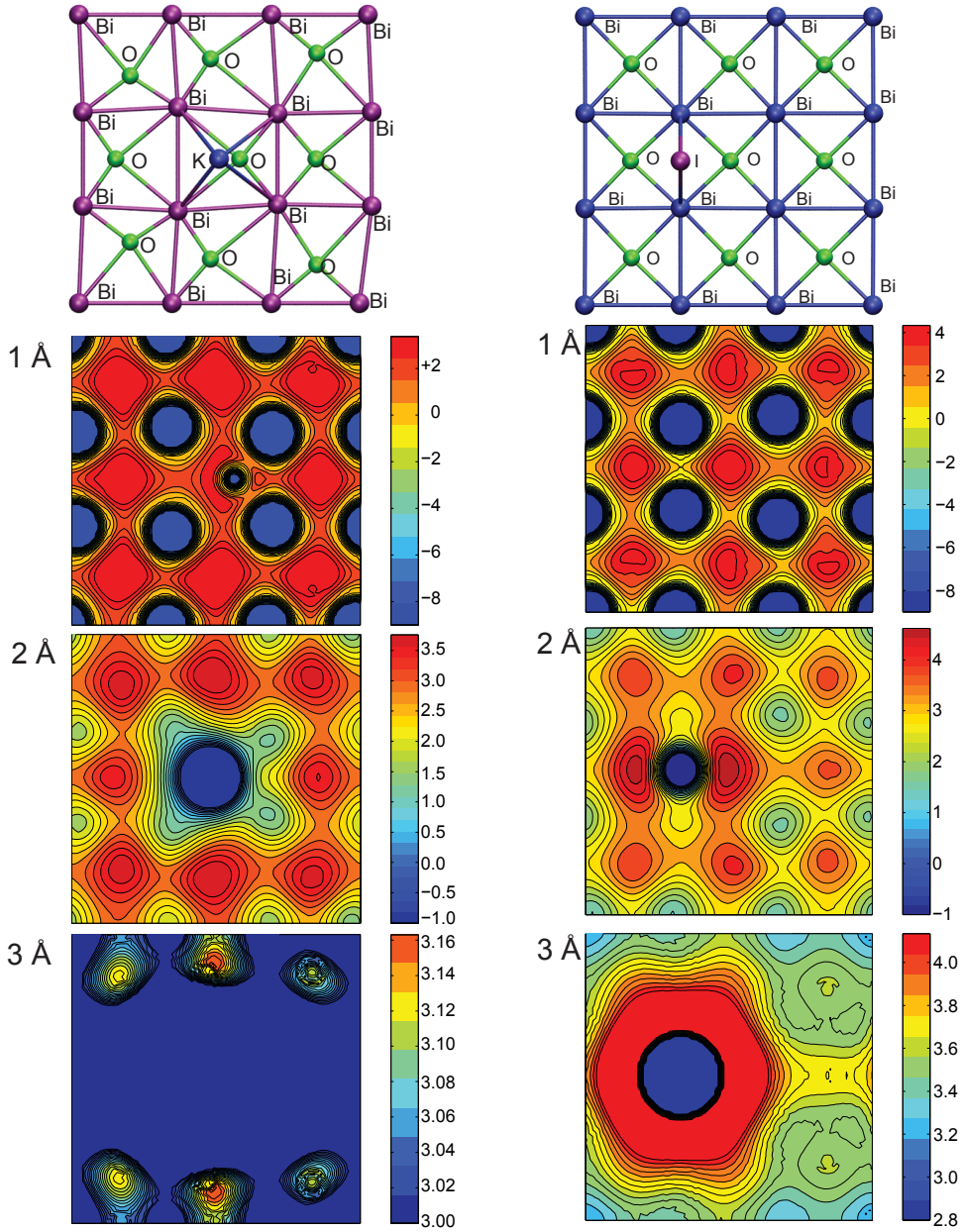

Figure 2.4: Local work function plots of Bi-2212 surfaces with adsorbed potassium and iodine, at 1, 2, and 3 Å from the atomic plane, along with a diagram of the real-space relaxed structure, as calculated by DFT. Each plot is 10 Å square and energy values are given in eV.

the adsorbed adatom compared to the clean surface in either case, other than the slightly positive charge induced on the O atom below the K adatom, as the adsorbate attracts the extra electron. Moreover, the calculated Bi energy at 1 Å (a large negative value < -31 eV) would predict no neutralization, as the Fermi level would be so far below the ionization level of the incoming ion that it would be unable to neutralize it from a purely energetic consideration. Similarly, at 3 Å the surface potential is not expected to make a major contribution to the charge exchange, since the potential there appears to be more or less uniform except at the adsorbate site itself, in contradiction with the argument above regarding the angular dependence of neutralization. However, at 2 Å there is both a significant corrugation in the potential, including the expected shift due to the adsorbate, and a reasonable range of energy values to allow for the observed neutral fractions. Thus, it could be assumed that the freezing distance for resonant neutralization resides somewhere near 2 Å above the BiO plane in Bi-2212.

To more quantitatively determine the freezing distance, the LEP determined by DFT was used to plot the average potential above the Bi sites versus distance from the surface, which is shown in Fig. 2.5, with the criterion that the potential vanishes at infinity. Note that the distance from the surface is defined here as originating from the mean height of the topmost-layer Bi. The average potential for the iodated surface differs from that of the clean surface for a range of distances, supporting a change in ion neutralization with I coverage. Conversely, for K the potential is rather close to that of the clean surface, suggesting that K adsorption would not lead to a change in neutralization. This is in remarkably good agreement with the measurement, provided that the freezing distance is less than 1.7 Å. Further, since the potential is very large and negative below about 1.5

Å , the freezing distance is likely to be between 1.5 and 1.7 Å . The difference between the adsorbed curves and the clean surface curve is plotted in the inset of Fig. 2.5, which shows the greatest disparity between the curves between the curves at 1.65 Å . This is a plausible value for the freezing distance at this ion energy [18].

We note that the prediction is not that the overall work function of the surface does not change upon K adsorption. Indeed, the DFT results do predict that the average overall work function would be altered in the presence of either adsorbate in a manner qualitatively consistent with the measured work function changes. However, since the freezing distance is close to 1.6 Å and since the ion probes the potential around the Bi atoms, the overall work function shift is irrelevant to the resonant charge transfer for the Bi SSP. We further note that the predicted overall work function estimate from the calculation cannot be compared quantitatively to the experimental value, as the coverage of adatoms in the calculation does not match the experimental situation. We thus confine ourselves only to a discussion of relative changes in the work function.

2.3.2.3 Discussion

I_2 and other halogen molecules often adsorb dissociatively, even at low temperature [22]. For TiO_2, chlorine has been shown to sit on a multi-coordinated cation site, preferentially adsorbing at an oxygen vacancy [23]. In our case, the neighboring Bi atoms, which are formally in the 2+ oxidation state, reduce slightly, compared to the stoichiometric surface, in order to accommodate the 1− iodine atom on the hollow site. This would affect the potential at the Bi sites, as predicted by DFT, leading to a decreased neutral fraction,

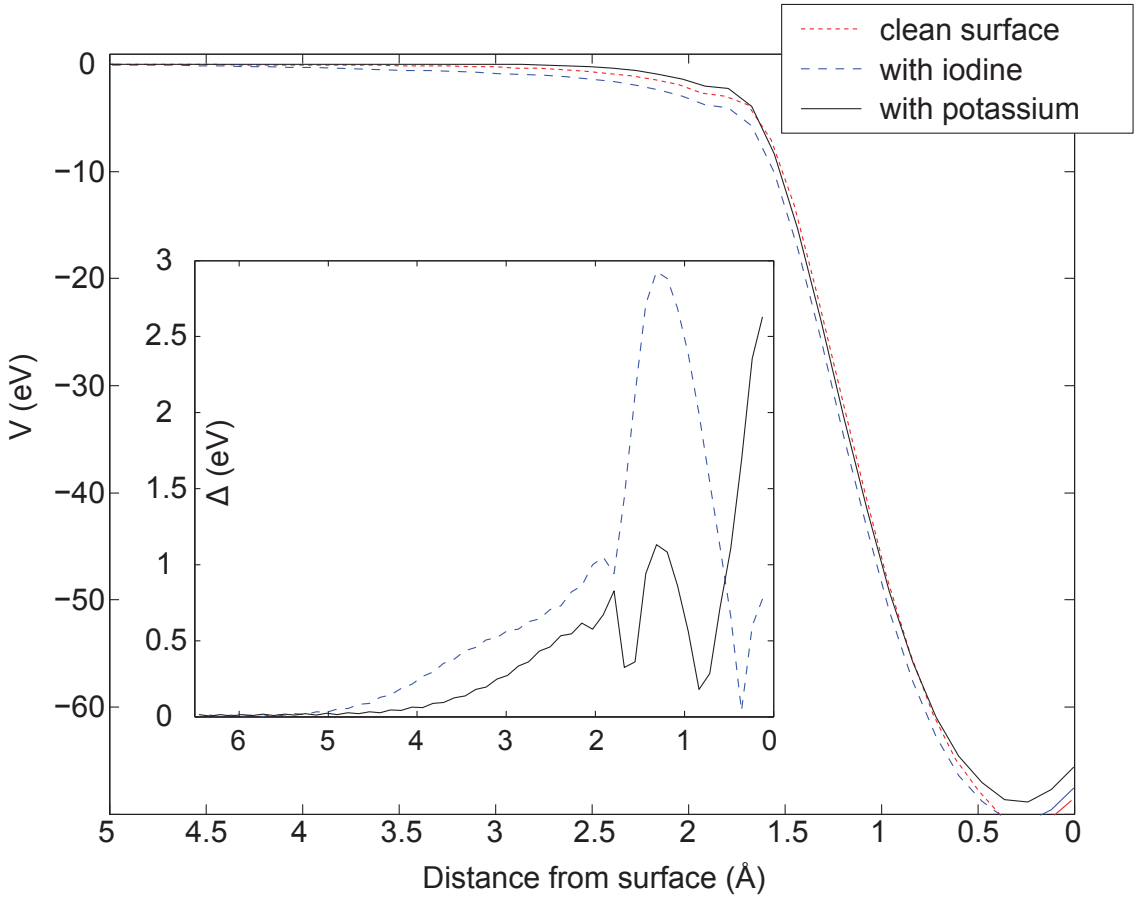

Figure 2.5: Average LEP above Bi sites as a function of distance from the surface, where the potentials for the clean, iodine-, and potassium-adsorbed surfaces are shown. Inset: the differences between the clean LEP and the iodine-surface and potassium-surface LEP, respectively. The lower curve, corresponding to potassium, shows that, for a certain range of values, the LEP of the potassium-adsorbed surface is considerably closer to that of the clean surface than is the LEP of the iodated surface.

as observed.

The absence of a change in Bi SSP neutral fraction in the presence of K can be attributed to the insensitivity of the LEP above the Bi sites, as predicted by DFT. Other than an LEP effect, however, there are two alternative explanations to the result that ionization is affected by iodine but not potassium. First, it could be that single-scattering from Bi is shadowed by the adsorbate, so that one or more of the four surface Bi atoms underneath the adsorbate do not contribute to the measured neutral fraction. Second, it could be that the DFT is not predictive when placing the adsorbate in the high-symmetry site because the actual adsorption sites are instead low-symmetry sites such as step edges and defects. We consider these possibilities in turn.

The notion that the adsorbate prevents ions scattering from Bi atoms below it is doubtful for two reasons. First, the TOF spectra show no significant attenuation of the Bi peak as K is deposited. Second, the results of dynamical scattering simulations performed with KALYPSO [24] predict no attenuation of the peak: Simulations using the ZBL screened potential tracked a large number of collisions of Na^+ ions with the crystal to determine the kinematics of the backscattered ions. A cell, made of the four atoms with the predicted relaxed locations of the Bi atoms nearest to the K atom, was bombarded by 2 keV Na^+ atoms under conditions identical to the experiment. This simulation showed a strong single-scattering peak in the energy spectrum. When K was added in the predicted adsorption position and the simulation was run again, no significant change of the single-scattering peak intensity was observed, and the only difference in the spectrum was the addition of a very small peak corresponding to Na^+ scattering from K. This suggests that the ions probe all of the Bi atoms in the unit cell regardless of the presence of the K adsorbates. Thus, the

calculated average value of the potential at the Bi atoms shown in Fig. 2.5 is the proper one for comparison to the experimental data, as it includes all atoms in the unit cell.

A more plausible explanation than the shadowing effect is that K adsorbs at sites other than those suggested by the DFT calculation. It has been observed previously (see, e.g., Ref. [25]) that alkalis on oxide surfaces can chemisorb at step edges and crystal defects. This has also been observed for some metal reconstructions [26]. On semiconductor surfaces, adsorbed alkalis can form chains, or "nanowires" [27]. Thus, there is a general trend that alkalis often adsorb to form small structures, rather than as isolated adatoms. Although we cannot determine from the present data whether the K is agglomerated at step edges or if it has formed small islands or chains, such adsorption would explain the results. Under this assumption, the saturation coverage could be low and the neutralization in scattering from Bi atoms, the preponderance of which are far away from the K atoms, would be generally unaffected. The adsorption would still influence the macroscopic work function, however, as was observed. STM measurements are suggested as a means for determining the actual adsorption behavior of alkalis on Bi-2212.

2.4 Conclusions

Low energy ion scattering is an effective probe of the physical and electronic surface structure of Bi-2212, namely the local work function changes and physical reconstruction due to adatom adsorption, when used in conjunction with a DFT analysis. The energetically favored adsorption sites for iodine and potassium influence the average potential around the surface Bi atoms in a manner commensurate with the change in neutralization probability

seen in the experiment. In particular, iodine adatoms remove charge from Bi sites, leading to a decrease in the neutral fraction, while K adatoms do not affect the average LEP at the Bi sites. These facts, when considered together, imply that resonant charge transfer is determining the measured neutral fractions, with a characteristic freezing distance of 1.6 ± 0.1 Å .

Bibliography

[1] K. K. Gomes, A. N. Pasupathy, A. Pushp, S. Ono, Y. Ando, and A. Yazdani, Nature **447**, 569 (2007).

[2] K. McElroy, J. Lee, J. A. Slezak, D. H. Lee, H. Eisaki, S. Uchida, and J. C. Davis, Science **309**, 1048 (2005).

[3] K. Tanaka, W. S. Lee, D. H. Lu, A. Fujimori, T. Fujii, Risdiana, I. Terasaki, D. J. Scalapino, T. P. Devereaux, Z. Hussain, and Z. X. Shen, Science **314**, 1910 (2006).

[4] S. H. Moffat, R. A. Hughes, G. D. Poulin, J. S. Preston, D. N. Basov, T. Stract, and T. Timusk, IEEE Trans. Appl. Supercond. **7** (1997).

[5] A.A. Dzhurakhalov and F.F. Umarov, Nucl. Instrum. and Methods Phys. Res. B **171**, 509 (2000).

[6] J. W. Rabalais, *Low Energy Ion-surface Interactions* (Wiley, New York, 1994).

[7] G. Kimmel and B. Cooper, Rev. Sci. Instrum. **64**, 672 (1993).

[8] J. Los and J. J. C. Geerlings, Phys. Rep. **190**, 133 (1990).

[9] J. Zavadil, Surf. Sci. Lett. **143**, L383 (1984).

[10] C. B. Weare and J. A. Yarmoff, Surf. Sci. **352**, 359 (1996).

[11] R. D. Gann, G. D. Gu, Z. Xu, and J. A. Yarmoff, To be published.

[12] W. K. Wang, W. C. Simpson, and J. A. Yarmoff, Phys. Rev. B **61**, 2164 (2000).

[13] J. A. Yarmoff and C. B. Weare, Nucl. Instrum. and Methods Phys. Res. B **125**, 262 (1997).

[14] Y. Matsui, H. Maeda, Y. Tanaka, and S. Horiuchi, Jpn. J. Appl. Phys. **27**, L372 (1988).

[15] O. S. Oen, Surf. Sci. Lett. **131**, L407 (1983).

[16] J. J. C. Geerlings, L. F. T. Kwakman, and J. Los, Surf. Sci. **184**, 305 (1987).

[17] S. Saito, Y. Uhara, Y. Kogushi, H. Yoshida, S. Isono, H.Yamasaki, H. Murakami, T. Sutou, T. Soumura, and T. Kioka, Phys. Status Solidi **202**, R129 (2005) a.

[18] G. A. Kimmel and B. H. Cooper, Phys. Rev. B **48**, 12164 (1993).

[19] G. F. Liu and J. A. Yarmoff, Surf. Sci. **600**, 2293 (2006).

[20] Y. Matsui, H. Maeda, Y. Tanaka, and S. Horiuchi, Jpn. J. Appl. Phys. **28**, L946 (1989).

[21] G. Kresse and J. Hafner, Phys. Rev. B **47**, 558 (1993).

[22] P. A. Dowben and M. Grunze, Phys. Scr. T **4**, 106 (1983).

[23] U. Diebold, Surf. Sci. Rep. **48**, 53 (2003).

[24] M. A. Karolewski, Nucl. Instrum. and Methods Phys. Res. B **230**, 402 (2005).

[25] M. Brause, D. Ochs, J. Gunster, T. Mayer, B. Braun, V. Puchin, W. Maus-Friedricks, and V. Kempter, Surf. Sci. **383**, 216 (1997).

[26] A. Norris and R. McGrath, J. Phys.: Condens. Matter **11**, 9549 (1999).

[27] L. J. Whitman, J. A. Stroscio, R. A. Dragoset, and R. J. Celotta, Phys. Rev. Lett. **66**, 1338 (1991).

Chapter 3

Surface restructuring in sputter damaged $Bi_2Sr_2CaCu_2O_{8+\delta}$

3.1 Introduction

Ion beam mixing of surfaces under particle bombardment is a phenomenon of considerable importance, especially with respect to the resolution of secondary-ion mass spectrometry depth profiling [1, 2, 3] and to the formation of surface structures in thin films via sputtering [4, 6, 5]. The projectile species, energy, and the composition of the target crystal all greatly affect these processes, the result of which could be the formation of 2D or 3D structures [7]. Collision cascades created during sputtering either result in thermal spikes that activate what are essentially chemical interactions, or they proceed in a largely ballistic way, with binary collisions accounting for the final arrangement of atoms.

This chapter contains material published in R.D. Gann, Jinsheng Wen, Zhijun Xu, G.D. Gu, and J.A. Yarmoff, "Surface restructuring in sputter damaged $Bi_2Sr_2CaCu_2O_{8+\delta}$ investigated by low-energy alkali-ion scattering", Phys. Rev. B (in press)

The miscibility of target atoms, sputtering yield, and mass of the projectile all contribute to the final structure, with purely kinematic effects being in competition with chemical or energetic processes.

Despite its importance, there are still significant open questions about the details of the re-arrangement that atoms undergo in ion beam mixing. This is especially true when it comes to the outermost layer of atoms, as the analytical techniques used typically probe many atomic layers, thus missing detail on the monolayer length scale. While the density of species can be depth profiled by RBS after sputtering [8], it is often impossible to say where the atoms in the resulting layers originated. Forming structures with marker layers (ones with more than one atomic species, formed into layers) partially solves this problem, but systems fabricated for this purpose have been large-scale (> 50 nm) in size, and hence miss the fundamental atomic scale details of the ion beam mixing process.

The problem of creating a heterostructure with many distinct marker layers is obviated by using a substance that naturally organizes into pristine planes of differing atomic species. One such material is $Bi_2Sr_2CaCu_2O_{8+\delta}$ (abbreviated Bi-2212), a high-Tc superconductor. It can be reliably cleaved in ultra-high vacuum (UHV), producing atomically flat and clean terraces. Each of the first four layers of the structure contains metallic atoms that differ in mass, from 40 to 209 amu, all within about 6 Å along the c-axis. It is thus unlike two-component materials, such as TiO_2 or GaAs, where the origin of the post-irradiation surface atoms cannot be identified. The application of a surface sensitive and mass-resolved measurement technique to Bi-2212 would enable a determination of not only what the surface was composed of, but where the atoms that make it up originated from with atomic-layer resolution.

Bi-2212 is also an interesting material because the outer layer is composed of Bi, a well-known surfactant. The effect of surfactants on materials is to reduce their overall surface energy. This has the result of allowing layers to exist even with a large lattice mismatch and strain [9]. As such, there is the opportunity to see if it is either kinematics, due to the atomic collisions, or energetic mechanisms, such as surface segregation of surfactants, that ultimately win out in the sputtering process.

We employed low-energy ion scattering (LEIS) with sodium (Na^+) projectiles to determine the composition specifically of the outermost atomic layer after sputtering. Note that the same information could not have been obtained with scanning tunneling microscopy (STM), as it is difficult to specifically identify the species responsible for image contrast [10]. Initial ion scattering studies of the Bi-2212 surface were recently conducted by our group, both with and without adsorbates [11]. This work clearly showed that the as-cleaved surface is terminated solely by Bi-O, as was previously posited, independent of cleave temperature. SIMS studies of Bi-2212 material were mostly ambiguous in detailing any sputter-induced changes [12], as they only investigated relatively large etch rates and were unable to say anything about the structure of the surface following sputtering.

LEIS owes its extreme surface sensitivity to the fact that single binary collisions that result in backscattering occur only with atoms that are directly visible to the ion beam. The ions that undergo single elastic collisions with these exposed surface atoms scatter with energy commensurate with the target mass, so that the atomic species at the surface can be positively identified using simple classical mechanics. By employing time-of-flight (TOF) detection, the surface sensitivity is independent of the ion neutralization, as the detector responds identically to ions and neutrals. This provides a more realistic picture of the atomic

composition at a surface than does traditional ion scattering spectroscopy (ISS) using He projectiles [13] or SIMS studies which detect only secondary ions. Single scattering from Bi, Sr, Ca, and Cu atoms would be well separated in LEIS spectra, so it becomes possible to specifically infer which layers of the structure contribute atoms to the resulting surface layer when the sample is sputtered. (Note that oxygen is too light to identify with Na^+ projectile backscattering.) Although sputter beam studies have been performed looking at the restructuring of three-component solids, such as $SrTiO_3$ [14], none to our knowledge have been conducted with more than 2 easily identifiable species.

In this study, Na^+ TOF-LEIS was collected as the Bi-2212 surface was sputtered by Ar^+ with fluences ranging from very light sputtering to that of one incident Ar^+ ion per surface atom. Ballistic simulations (detailed below) indicate that this energy results in collision cascades that affect several layers in the crystal, and the depth affected at these sputtering energies is estimated to be greater than 20 Å [15]. The results show, however, that an unexpectedly large amount of Bi remains on the surface as Sr becomes uncovered. Thus, the expectations of a purely kinematic process differ from the experimental findings. We conclude that a layer of Bi-O is formed at the surface by the sputtering process, and this layer blunts the effect of further sputtering due to the immiscibility of Bi and its surfactant effect on flat semiconductor growth. The make-up of this layer has essentially no contribution from Ca or Cu, implying that ion beam mixing does not occur due to this protective layer.

3.2 Experimental Procedure

The experiment was conducted in an ultra-high vacuum (UHV) chamber with a base pressure of 3×10^{-10} torr. Single crystal Bi-2212 samples were grown by a floating zone method [16], and the superconductivity of the single crystals was measured by SQUID. The superconducting transition temperature of the as-grown Bi-2212 crystals was 91 K. Samples were cleaved in situ using the following method provided by A.N. Pasupathy [17]: The $\sim 7 \times 7$ mm^2 samples were affixed to a copper sample holder with a very thin layer of H20E epoxy (Epotek), which was cured for 30 minutes at 100 °C. Then, a small piece of aluminum was affixed to the top of the sample itself by way of a small amount of Torr-Seal, which was cured for 15 minutes at 70 °C. After transferring the sample into the UHV chamber, the aluminum-Torr-Seal amalgam was mechanically knocked off, cleaving the sample and revealing a pristine Bi-O layer with a mirror-like surface [11].

To investigate the effects of beam damage, samples cleaved at room temperature were bombarded with an Ar^+ beam at 500 eV with a current density of approximately 5 μA cm^{-2}. Sputtering was carried out with a back-filled PHI sputtering gun at a chamber pressure of 1×10^{-5} torr of Ar. Time-of-flight (TOF) LEIS spectra and secondary electron cutoff measurements aimed at measuring work function shifts were collected following each round of sputtering after the Ar was pumped out, and the cycle was repeated for several rounds. Fluence was increased past where the ratio of surface Bi/Sr reached a plateau, up to a fluence corresponding to one incident Ar^+ ion per surface Bi atom. We note that in prior work [11], no significant structural differences were observed between ISS of samples cleaved at room temperature and those cleaved at low temperature.

The details of the TOF ion scattering apparatus have been described elsewhere [18]. For these experiments, a 2 keV beam of Na^+ ions is produced from a Kimball Physics IGS-4 alkali ion gun, which is pulsed at 80 kHz and focused onto the sample at incoming angle of 30° with respect to the surface normal. The flight time of the scattered projectiles emitted along the surface normal is recorded by measuring the time difference between the ion pulses and counts recorded on a micro-channel-plate detector located in the end of a flight tube at about 0.5 m from the sample. Although the pulse width can be as small as $\sim$ 20 ns, in this study we found that increasing the pulse width to $\sim$ 200 ns gave satisfactory time resolution and much better signal strength. Exposure to the alkali ion beam was limited to ensure less than 1% dosage to any spot on the specimen. The shift of the surface work function was determined by bombarding the sample with 100 eV electrons and measuring the low-energy cutoff of the secondary electron spectra with a Comstock AC-901 electrostatic analyzer, giving work function shifts to within an accuracy of 0.04 eV [19].

Computer simulations using two different software packages were carried out to help understand the LEIS and sputtering results. Both use the screened Ziegler-Biersack-Littmark ("universal") potential, in the binary collision model, to approximate the final trajectories of ions and surface atoms in the scattering and sputtering processes.

The first simulation package utilized was KALYPSO [20], which is ideally suited for ion scattering. Although limited to two target elements, it can quickly simulate the energy spectrum of backscattered ions for a predetermined crystal structure and set of initial trajectories. Because of the two-element limitation, scattering from Bi and Sr in the crystalline structure had to be modeled separately, as described below. The sum of these

results would be identical to the result of performing the simulations together, as there were essentially no backscattered trajectories that interacted with both of these elements.

The second simulation software package, MARLOWE [21], was used to estimate the efficiency with which each atomic species in the crystal was sputtered, assuming that the process is essentially ballistic. The software can accommodate the entire crystal structure of Bi-2212, and keeps track of the dynamics of collisions in a cascade created by an incident ion. Atoms displaced in a collision can remain in the displaced position during subsequent cascades, allowing simulation of the effect that crystal damage has on the sputtering rate. The software keeps track of all ejected atoms, and so it is ideal for simulating the sputtering yield for this system. Because the program has a limit of 5 atomic species, it was not possible to also specify Ar as the incident ion. Instead, Ca was used for the projectile, as its mass is nearly the same. Although the accuracy of the screened potential will be slightly incorrect due to the different number of electrons in Ar and Ca, this small deviation is assumed to be negligible.

In MARLOWE, the unit cell of Bi-2212 was specified, and a $3 \times 3 \times 3$ crystal constructed from it. Incident Ca ions were given a kinetic energy of 500 eV and the initial trajectories were chosen randomly on the target surface. Using identical binding energies of 0.5 eV for all species, atoms escaping from the crystal by way of collision cascades were recorded and tabulated as a function of accumulated damage. In this way, the sputtering rate of each species can be modeled relative to all the others as the crystal is subjected to lattice vacancies and displacements. After a collision cascade has terminated, the crystal can either be reset or the current damaged configuration can be retained for further calculations. In our simulations, the program accumulated damage until the crystal reached a steady state

(chosen to be after 100 cascades), whereupon it was reset. The number of outgoing atoms was then tabulated to give the distribution of sputtered atoms by species. We note that the system is quite insensitive to the value of binding energy, as is normally reported for these energy ranges [22]. As such, the model does not update binding energies for displaced atoms.

3.3 Results and Discussion

Figure 3.1 shows the atomic structure of Bi-2212. The material is a layered crystal with repeated inverted layers. The oxygen atoms are in-plane with the metal atoms for all layers except the Sr-O layer, in which the oxygen atoms are located slightly closer to the Bi-O layer. Weak van der Waals binding between the adjacent Bi-O layers ensures that samples always cleave at this interface [23].

A TOF spectrum from as-cleaved Bi-2212 is shown as the bottom curve of Fig. 3.2. The sharp peak representing quasi-single-scattering binary collisions of Na+ with Bi is clearly seen at about 4 μs flight time. The broad background at longer flight times corresponds to projectiles that have escaped the surface after suffering multiple collisions, or species recoiled into the detector (presumably oxygen). No scattering from Sr or any other metallic element is visible from the virgin surface, as was previously observed [11].

TOF-LEIS spectra collected as the sputtering fluence is increased are shown in Fig. 3.2. Note that it is estimated that there are 1.5×10^{15} surface atoms cm^{-2} in Bi-2212, so these spectra represent the range of fluences from 0 to 1 Ar^+ ion per surface Bi atom (although it should be noted that each collision cascade is expected to eject on average

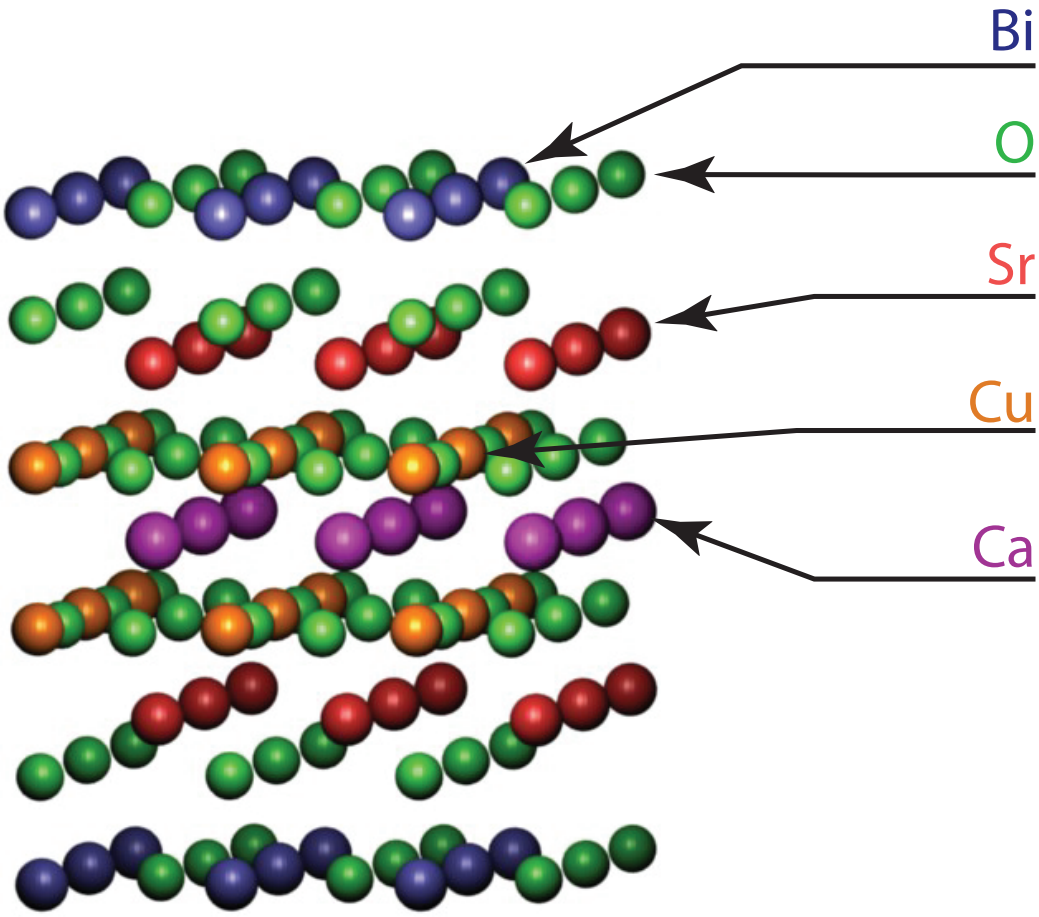

Figure 3.1: A side view of the crystal structure of $Bi_2Sr_2CaCu_2O_8$. The dimensions depicted are 7.33 Å × 7.33 Å × 12 Å

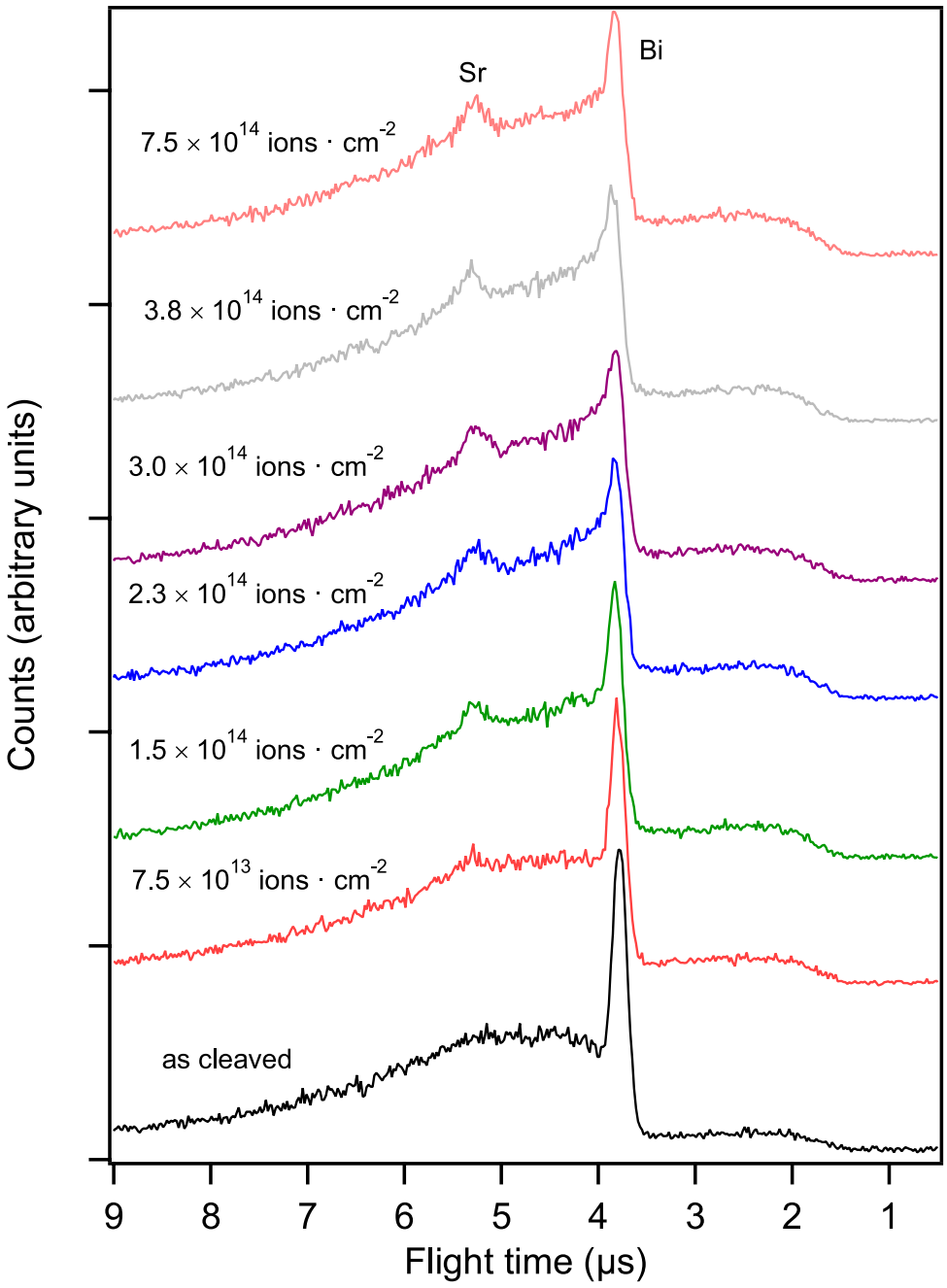

Figure 3.2: Total yield scans of Bi-2212 as the surface is sputtered.

about 1.6 atoms [24]). The single-scattering peak (SSP) that emerges at ~ 6 μs after 1 minute of sputtering is attributed to scattering from Sr, as the flight time indicates that the energy of that peak corresponds to an elastic binary collision of Na^+ with Sr, consistent with the simulations (c.f. Figure 3.3). The Bi peak is somewhat attenuated as the Ar^+ fluence increases, while the intensity of the Sr SSP increases. After a fluence of 2×10^{14} cm^{-2}, these intensities saturate. In addition, the underlying Cu and Ca species are never visible with LEIS. Although not shown in the figure, even quadrupling the fluence produces no further noticeable effects.

The cross-section for scattering is dependent on the mass of the target atom, and is thus not the same for all species in this material. It is possible, however, to estimate the cross-sections for scattering of Na^+ from these species using Thomas-Fermi theory [25]. The purpose is to give a rough estimate of the minimum amount of Cu that would need to be at the surface due to ion-beam mixing so that the signal would be visible. The calculated ratios of the differential cross sections for Na scattering from Sr, Ca, Cu, compared to Bi, are $\sigma_{Bi}/\sigma_{Sr} = 1.65$, $\sigma_{Bi}/\sigma_{Ca} = 1.90$, and $\sigma_{Bi}/\sigma_{Cu} = 2.29$. Thus, since Cu has only a slightly smaller cross section than Sr, it should also be seen if it were present in a similar concentration. By employing a fitting procedure (described below), it is shown that the fraction of surface atoms made up of Cu is less than 1%. We can conclude from this that the LEIS spectra probe only the outermost layer of the sample; moreover, although Sr becomes visible quickly, Cu, though located only one atomic layer below, is never present at the surface. Thus, Cu atoms are not promoted in any significant number by the ion bombardment from the third layer to the higher layers where they could be detected.

To investigate whether the absence of single scattering from Sr is reasonable from

the as-cleaved surface, and to clarify the role of oxygen vacancies in the eventual emergence of a Sr peak, simulations were performed using KALYPSO. The two-element limitation of the software required that Na^+ scattering from two model crystals be simulated separately. The first model crystal is the flat uppermost atomic layer of Bi-O as depicted in Fig. 3.1. The second includes the Sr atoms, the oxygen atoms associated with the Sr layer, and the oxygen atoms that lie directly above the Sr atoms in the Bi-O layer. We used an incoming altitudinal angle of 30°, along the low-index direction, and an incoming energy of 2 keV, consistent with the experiment.

The normal emission intensity for scattering from the Sr system is plotted vs. outgoing energy in Fig. 3.3 for differing levels of first layer oxygen vacancies (bottom three curves). Oxygen vacancies were created explicitly in the target crystal by removing a specific fraction of equivalent surface oxygen atoms from the second model structure. The vacancies were chosen so that there would not be any effect of correlations, e.g., there could be additional effects if two adjacent surface oxygen atoms were removed. Although some scattering from Sr is observed in the simulations in the absence of vacancies, at normal emission the trajectories are blocked along the outgoing trajectory by the first layer oxygen atoms positioned directly above the Sr atoms. Some events do scatter from Sr and then glance off of a surface O atom on the way out, however, which results in a small, wide peak at about 600 eV. The peak is at a lower energy than the single-scattering energy of Na^+ from Sr because of extra losses incurred in the grazing collisions with oxygen. This small signal for single scattering from Sr would be very difficult to resolve against the large background in the experimental spectra, and for small detection angles may not appear at all. As oxygen is removed from the surface, however, a clear single-scattering peak from Sr

emerges at about 700 eV, while the 600 eV peak corresponding to scattering from both Sr and O diminishes. Also shown in Fig. 3.3 are the simulated data for scattering from the Bi-O layer and the experimental data, plotted with respect to energy, for the cleaved and sputtered surfaces. The agreement of the single scattering peak positions for Bi and the revealed Sr is quite good.

A quantitative analysis of the scattering yield from Bi and Sr is displayed in Fig. 3.4, where the Bi intensity is seen declining simultaneously with the Sr intensity rising. This scattering intensity is calculated using a fit procedure to fit the peaks in the TOF spectra as follows: The background in the neighborhood of the peak is considered to be linear, with a Gaussian superimposed on it. After this curve is fit, the area under the Gaussian is calculated and used as the measured intensity, whereas the area under the line is considered to be background. Note that the Bi and Sr signal strengths have been normalized to each other using the cross-section ratios provided above. The graphs simultaneously level-off at a fluence of 2.2×10^{14} cm^{-2}.

The observed ratio of Bi/Sr atoms at the surface, corrected for scattering cross section, is shown in Fig. 3.5 as a function of sputtering fluence along with the surface work function. The highest fluence corresponds to one incident Ar^+ ion per surface Bi. Ion scattering indicates that the ratio (right axis) saturates at a value of 2 Bi to 1 Sr atom at the surface. After abruptly shifting down (presumably due to the quick desorption of oxygen), the work function (left axis) increases to its quasi-static value of 0.4 eV above the clean Bi-2212 work function (4.85 eV). The intensity ratio and the work function reach their final values at nearly the same fluence. This steady-state is surprisingly long-lived, as

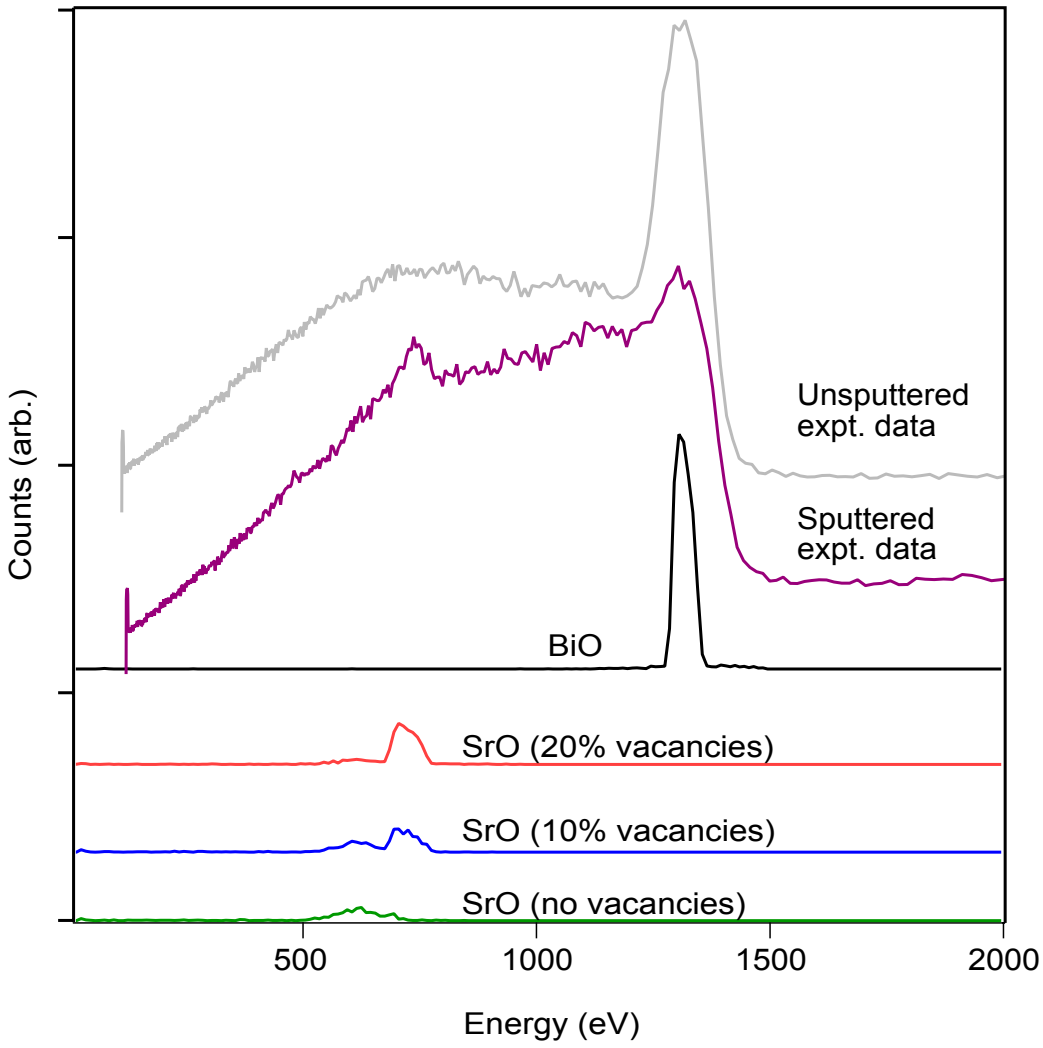

Figure 3.3: Ion scattering spectra predicted by KALYPSO simulation of the Bi-2212 upper layers (Bi-O and Sr-O). Sr-O is shown for differing levels of oxygen vacancies in the Bi-O layer. Also shown for comparison are measured TOF spectra of the as-cleaved and sputtered surfaces.

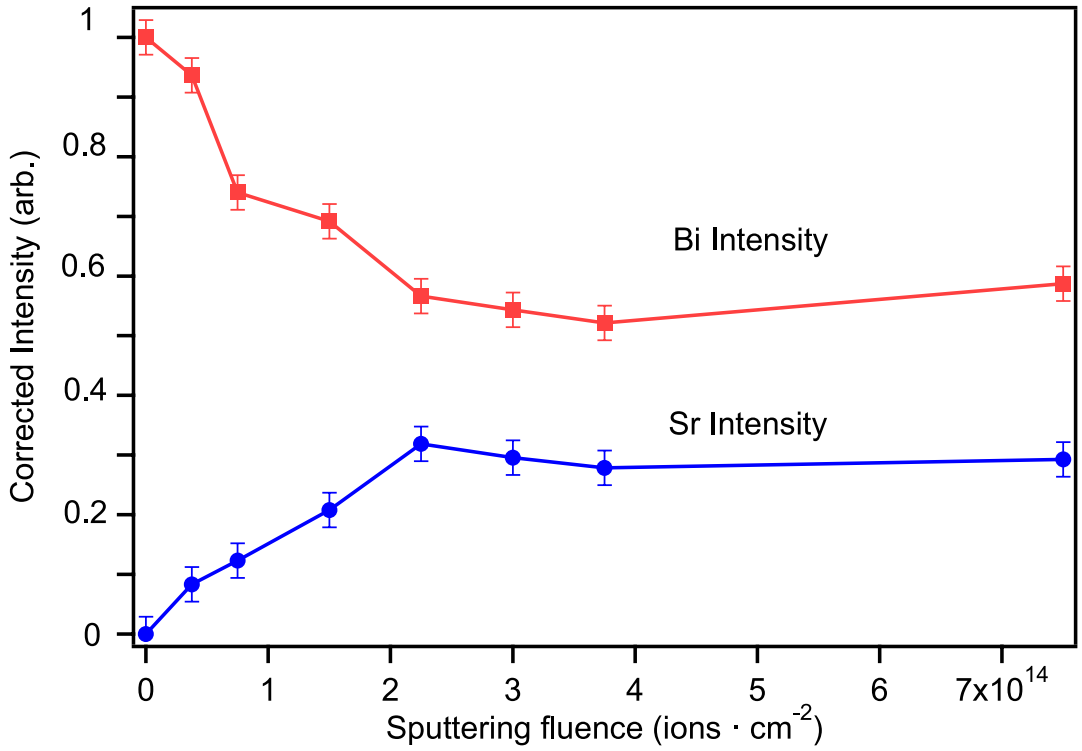

Figure 3.4: Measured single scattering intensities determined from the TOF spectra. The values are calculated by taking the area of the peaks in Fig. 3.3 and correcting for the scattering cross-section.

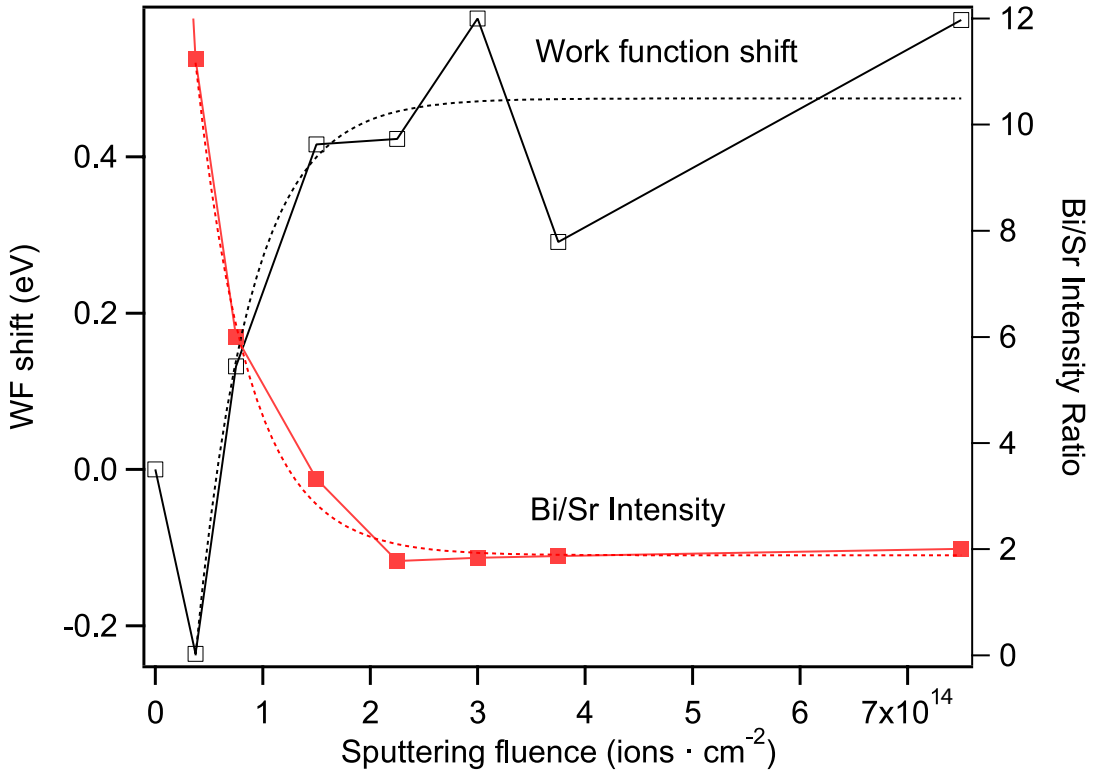

Figure 3.5: Ratio of the intensities of the Bi and Sr backscattering peaks, and the surface work function shift, plotted as a function of sputtering fluence.

quadrupling the fluence does not noticeably change it.

What is notable about this result is the lack of apparent ion beam mixing past the point of Sr saturation. Low energy bombardment in heterostructures has been shown (e.g. [26, 27]) to broaden the apparent interface on the order of 1 nm at fluences similar to ours, which would include all of the first 7 layers of the Bi-2212 structure. This being the case, it would seem that all layers of the Bi-2212 structure would be evenly mixed at the surface, and not merely the first and second layers. Correspondingly, if the oxygen were removed, it would make these other metallic species very easy to see in the TOF spectra, as the broad

background would diminish. Moreover, supposing that the process were relatively slow, the work function should reflect a more gradual change as buried species diffuse to the surface, whereas our findings show that the work function promptly decreases and then stays there.

Figure 3.6 shows the number and type of atoms ejected in a sputtering collision cascade as simulated by MARLOWE, where the horizontal axis can be thought of as time or sputtering fluence. The histogrammed number of ejected particles is tabulated by how many runs had been performed without resetting the crystal, so that time-evolution of the sputtering yield could be ascertained as a function of crystal damage. There were approximately 410^4 target atoms, with 14% each of Bi, Sr, and Cu, 7% of Ca, and 51% oxygen to begin with. As can be seen, oxygen is readily removed, with Bi at a third of that rate and Sr at a mere quarter of that. The simulation predicts that after a small number of runs most of the Bi has been sputtered away, while the Sr is considerably more resistant to sputtering. This is not, however, consistent with the experimental observations.

Any oxygen vacancies in the top layer should result in a continual increase of the Sr signal, as MARLOWE predicts that many Bi and O atoms should be sputtered, but not many Sr atoms. Instead, however, the Sr stays partially obscured. Considering that the initial ratio of Bi to Sr in the substrate was 1:1, and that Bi is much more readily sputtered, one would expect a mixed surface to have much more Sr signal in the data. By the end of the simulated crystal damage, there is a ratio of 1.45 Sr to 1 Bi. In other words, the simulation predicts that there will be more Sr than Bi, which is the reverse of what is observed in the experiment.

The sputtering simulation assumes that the atoms are displaced only due to actual

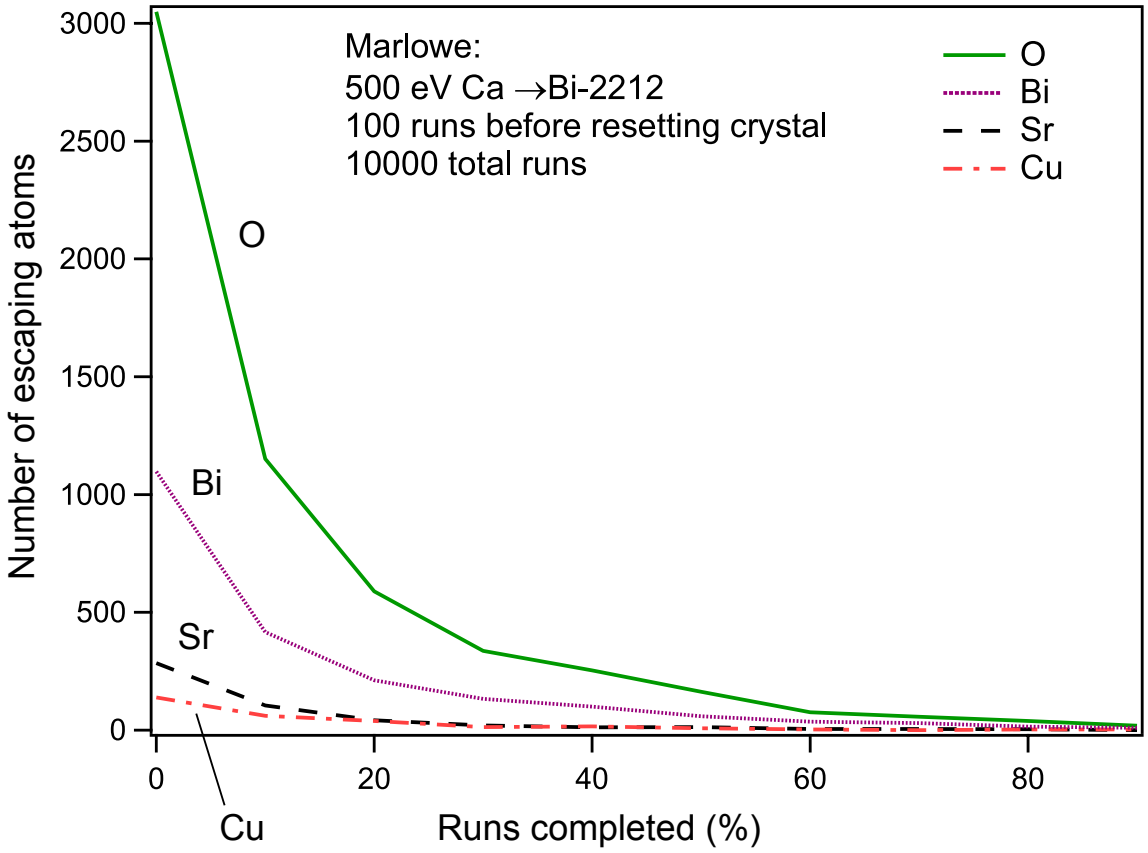

Figure 3.6: Number of sputtered atoms of O, Bi, Sr, Cu, as predicted by MARLOWE simulation, as a function of sputtering damage. 100 trials of 100 incident ions of Ca were separately performed, and the results added afterwards. The data is histogrammed by time (number of ions incident on the surface out of 100).

collision cascades. Bi, however, has a low miscibility, and at the surface is likely to be highly mobile. Oxygen, too, is apt to migrate from lower layers to the surface, which has been suggested to explain the results of SIMS studies of Bi-2212 [12].

With this in mind, there is a very real possibility that a flat layer of Bi-O, or the somewhat less likely Bi_2O, forms at the surface, even though its structure is incommensurate with the underlying crystal. Growth of semiconductors such as Bi-O is observed in surfactant-like behavior in 2D CVD experiments [28]. Bi, a natural donor, lowers the energy of the surface layer, forming a smooth surface even when there is a large lattice mismatch between the overlayer and the substrate. Indeed, thin films of Bi-O are found to have a particularly low internal stress in the presence of excess oxygen [29]. Because of its low miscibility, and its low surface energy, we expect that the capping layer is around 1 atomic layer in thickness. Studies of the roughness of this system by in situ AFM would be interesting, though they are not possible in our apparatus.

That the scattering signal from Sr remains lower than expected and that of Bi higher, implies a layer of Bi-O at the surface. This layer would then obscure the Sr, even as oxygen was sputtered away, and would also negate any ion-beam mixing from occurring. The result is that Bi and Sr signals saturate at the values measured. Since the structure of this Bi-O overlayer may not be the same as that of the as-cleaved surface, the measured Bi/Sr ratio does not necessarily imply that the approximately 20% oxygen vacancies that was predicted using KALYPSO is quantitatively correct.

Note that we cannot strictly discount the possibility that the top layer is composed of amorphous Bi rather than Bi-O. There are, however, several reasons why it is reasonable to assume that the top layer has oxygen. Because of the relatively low surface energy, it

has been observed that lighter species segregate to the surface in systems such as Pt/TiO2 [30]. Furthermore, there is evidence to suggest that oxygen in Bi-2212 is highly mobile in vacuum, diffusing from the bulk to the surface [12, 31]. In addition, the work function would be expected to decrease if oxygen were being removed from the outermost layer, while in fact the work function increases as steady-state is attained. A high surface work function is normally associated with the dipoles created at an oxide surface. Note that x-ray photoelectron spectroscopy (XPS) data of the Bi core level shifts between the as-cleaved and the sputtered surface could clarify this, since the oxygen-induced Bi 4f binding energy shifts are on the order of a few eV. We are unable, however, to perform an XPS study on these samples with our equipment.

3.4 Conclusions

Behavior of the Bi-2212 surface under sputtering was investigated by 2 keV Na^+ low-energy ion scattering. The surface oxygen and Bi are readily removed at the start, in good agreement with simulation. Further sputtering unexpectedly results in a quasi-steady-state, leading to a stable Bi/Sr ratio. The results imply that a protective layer of Bi-O forms due to the high mobility of oxygen and the low miscibility of Bi. This process can form an amorphous layer because of the lowering of surface energy characteristic of the Bi surfactant effect, which forms a layer independent of the crystal structure of Bi-2212 itself. This layer then blunts the effects of local ion beam mixing so that Bi and O atoms block incoming ions from reaching the majority of Sr and other species in the crystal.

Bibliography

[1] J. Likonen, M. Hautala, and I. Koponen, Nucl. Instrum. Methods Phys. Res. B **64** (1-4), 149 (1992)

[2] C. W. Magee and R. E. Honig, Surf. Interface Anal. **4** (2), 35 (1982).

[3] J. B. Clegg and D. J. Oconnor, Appl. Phys. Lett. **39** (12), 997 (1981).

[4] C. W. Yuan, D. O. Yi, I. D. Sharp, S. J. Shin, C. Y. Liao, J. Guzman, J. W. Ager, III, E. E. Haller, and D. C. Chrzan, Phys. Rev. B, **80** (13), 134121 (2009)

[5] K. U. Joshi, A. M. Narsale, D. Kanjilal, T. N. Warang, T. K. Gundurao, and D. C. Kothari, Surf. Coat. Technol. **203** (17-18), 2476 (2009)

[6] C. W. Yuan, D. O. Yi, I. D. Sharp, S. J. Shin, C. Y. Liao, J. Guzman, J. W. Ager, III, E. E. Haller, and D. C. Chrzan, Phys. Rev. Lett. **102** (14), 146101 (2009).

[7] K. Zhang, M. Brotzmann, and H. Hofsass, New J. Phys. **13** (2011).

[8] W. Bolse, Mater. Sci. Eng. A **253** (1-2), 194 (1998).

[9] M. Copel, M. C. Reuter, E. Kaxiras, and R. M. Tromp, Phys. Rev. Lett. **63** (6), 632 (1989).

[10] S. Sugita, T. Watanabe, and A. Matsuda, Phys. Rev. B **62** (13), 8715 (2000).

[11] R. D. Gann, J. X. Cao, R. Q. Wu, J. S. Wen, Z. J. Xu, G. D. Gu, and J. A. Yarmoff, Phys. Rev. B **81** (3), 7 (2010).

[12] S. Saito, Y. Uhara, Y. Kogushi, H. Yoshida, S. Isono, H. Yamasaki, H. Murakami, T. Sutou, T. Soumura, and T. Kioka, Phys. Status Solidi A **202** (12), R129 (2005).

[13] J. Wayne Rabalais, *Low Energy Ion-surface Interactions* (Wiley, 1994).

[14] Zhiming Wang, Kehui Wu, Qinlin Guo, and Jiandong Guo, Appl. Phys. Lett. **95** (2), 021912 (2009).

[15] V. Konoplev, M. J. Caturla, I. Abril, and A. Gras-Marti, Nucl. Instrum. Methods Phys. Res. Sect. B **90** (1-4), 363 (1994).

[16] G. D. Gu, K. Takamuku, N. Koshizuka, and S. Tanaka, Jour. Cryst. Grow. **130** (1-2), 325 (1993).

[17] Abhay N. Pasupathy, Personal Communication.

[18] C. B. Weare and J. A. Yarmoff, Surf. Sci. **348** (3), 359 (1996).

[19] H. E. Bauer and H. Seiler, Surf. Interface Anal. **12** (1-12), 119 (1988).

[20] M. A. Karolewski, Nucl. Instrum. Methods Phys. Res. Sect. B **230**, 402 (2005).

[21] M. T. Robinson and I. M. Torrens, Phys. Rev. B **9** (12), 5008 (1974).

[22] Wolfgang Eckstein, *Computer Simulation of Ion-Solid Interactions* (Springer, Berlin, 1991).

[23] Y. Matsui, S. Horiuchi, H. Maeda, and Y. Tanaka, Jpn. J. Appl. Phys. **28** (6), 946 (1989).

[24] T. Nenadovic, B. Perraillon, Z. Bogdanov, Z. Djordjevic, and M. Milic, Nucl. Instrum. Methods Phys. Res. Sect. B **48** (1-4), 538 (1990).

[25] E. S. Parilis, L. M. Kishinevsky, N. Yu Turaev, B. E. Baklitzsky, F. F. Umarov, V. Kh Verleger, S. L. Nizhnaya, and I. S. Bitensky, *Atomic Collisions on Solid Surfaces* (North-Holland, Tashkent, Uzbekistan, 1993).

[26] J. H. He, C. A. Carosella, G. K. Hubler, S. B. Qadri, and J. A. Sprague, Phys. Rev. Lett. **96** (5), 056105/1 (2006)

[27] M. Menyhard and P. Sule, Surf. Interface Anal. **39** (6), 487 (2007).

[28] S. W. Jun, G. B. Stringfellow, J. K. Shurtleff, and R. T. Lee, Jour. Cryst. Grow. **235** (1-4), 15 (2002).

[29] R. B. Patil, R. K. Puri, and V. Puri, J. Phys. Conf. Ser. **114** (1), 012036 (2008).

[30] F. Pesty, H. P. Steinruck, and T. E. Madey, Surf. Sci. **339** (1-2), 83 (1995).

[31] S. Saito, T. Sutou, Y. Norimitsu, N. Yajima, Y. Uhara, T. Uenosono, T. Soumura, and T. Tani, Appl. Surf. Sci. **252** (2), 379 (2005).

Chapter 4

Dopant-enhanced neutralization of low energy Li^+ scattered from Si(111)

Charge exchange at surfaces is fundamentally important in many physical and chemical processes. Charge exchange influences, among other things, adsorption, etching, oxidation, surface reactions, and vapor deposition. In the dry processing of silicon for microelectronic fabrication, a dependence on doping of oxidation [1], etching rates [2], and silicide formation [3] has been observed. To determine how doping-induced electronic structure changes influence these processes requires a basic understanding of how charge exchange at semiconductor surfaces is influenced by doping. For example, the doping concentration changes the density of states at the surface by adding excess majority carriers, which could

This chapter contains material submitted as R. D. Gann, Z. Sroubek, and J. A. Yarmoff, Phys. Rev. Lett.

have a large effect on electron tunneling rates between reactants and the surface. In addition to populating the bands, the band gap of Si narrows with increasing dopant density [4], which may also influence charge exchange.

An example of the fundamental role that doping plays in surface reactions is the spontaneous etching of Si by XeF_2 in which the degree and type of dopant affects the reaction rate [5-7]. The reason for the etching rate dependence has been the subject of debate. Excess carriers due to doping may provide nucleation sites for chemical reactants, for example. Another possibility is that the negative F ions formed via tunneling influence band bending at the surface, which in turn affects the mobility of F^- in surface fluorosilyl layers. Because of the importance of charge exchange in physical and chemical processes, such as XeF_2 etching, direct measurements of charge exchange at semiconductor surfaces as a function of doping are crucial.

Low-energy ion scattering from surfaces provides a unique test environment for investigating charge exchange. This technique has shed considerable light on ion yields in secondary-ion mass spectroscopy [8], stimulated desorption [9, 10], and surface chemical phenomena such as reactivity, selectivity of reactions [11], and chemisorption. Despite the importance of semiconductors in materials science and manufacturing, there has been scant work on how the bulk band gap affects charge transfer between atomic particles and solid surfaces. Most theoretical analyses of charge exchange during ion scattering, for example, consider the solid to be a free Fermi gas of electrons with a jellium surface. Some recent theoretical [12] and experimental [13] studies have investigated the effects of an anisotropic projected surface band structure on charge transfer, but, again, only for metals.

Silicon provides a system in which the bulk band gap can be altered while retaining

the surface structure and work function, as the (111) face of differently doped samples can be identically prepared as hydrogen-terminated 7×7 surfaces with the Fermi level unpinned. By scattering low-energy ions from hydrogen-terminated Si as a function of doping, the effects of band gap magnitude, rather than merely the location of the highest occupied electronic level, can be probed.

Projectiles with low ionization energies or electron affinities (e.g., alkalis, O, Cu) are best suited for investigations of charge exchange that probe valance states of solids [14]. Li^+ alkali ions are used in the present work because their low mass allows for easy scattering from the relatively light Si atoms, their ionization potential overlaps the filled states in the solid, and the radial symmetry of the $2s$ ionization level enables a simple analysis. In the low energy regime (0.5-10 keV), the charge transfer to scattered alkali ions is dominated by resonant charge transfer (RCT), a one-electron process in which electrons tunnel between the sample and the ion only if the energy is degenerate between the two levels [15]. This process is non-adiabatic, resulting in a significant level broadening of the ionization state into a resonance, and consequently enhanced tunneling into newly available energy states.

On the clean Si(111) surface, there are dangling bonds which pin the Fermi level roughly in the middle of the gap, and provide neutralization that would otherwise not occur [17]. What is not completely clear, however, is which energy levels actually determine the neutralization: the bulk Fermi energy, the surface levels where the Fermi level is pinned, or a mixture of the two due to a transition region. As the surface dangling bonds are passivated, such as by deposition of atomic hydrogen, the Fermi level becomes unpinned [19], altering the charge transfer significantly. In the case of Si(111) and (100), for lightly doped samples the charge transfer to scattered Li^+ ions is suppressed as hydrogen is deposited [17].

Aside from the influence of dangling bonds, dopant density may also affect charge transfer. In a metal, the neutralization depends principally on the work function of the sample and the ionization level in the projectile atom [20]. Being that the difference in work function between heavily doped and lightly doped Si is only approximately 0.04 eV [21], very little difference in neutralization probability would be expected. The band gap in Si is narrowed significantly, however, above 10^{17} impurities per cm^3. It could be that the overlap of these bands with the ionization level in resonance with the surface bands would then have a large effect on neutralization.

The present work investigates the effect of dopant density and hydrogen adsorption on the neutralization of Li^+ ions scattered from the H/Si(111)-7 $\times$ 7 surface. Neutral fractions (NFs) and work functions are measured as samples are dosed with atomic hydrogen to passivate the dangling bonds. Measurements show that the n-type sample with a high dopant density has a large NF, despite nearly identical work functions between lightly- and heavily-doped samples. A simple flat-band jellium model, excluding states in the gap, is used to predict the NF of the fully passivated surface, and the agreement with experiment is excellent. This clearly shows that the bulk band gap has a large effect on ion-surface charge exchange, and that the process can be easily modeled.

All samples were prepared by resistive heating to 1100°C in ultra-high vacuum (base pressure 3×10^{-10} torr), yielding a clean, 7×7 surface as verified by x-ray photoelectron spectroscopy and low-energy electron diffraction. We used lightly-doped n-type (5.0 Ω cm), lightly p-type (1.0 Ω cm), medium n-type (0.01 Ω cm), and heavily n-type (0.001 Ω cm) samples. Atomic hydrogen was produced by backfilling the chamber with H_2 gas while the sample was held 1 inch away from and facing a hot tungsten filament that cracks the

molecules [22]. Doses are given in Langmuirs (1 L = 10^{-6} torr s) of H_2, as the actual production rate of atomic H cannot be directly characterized. Thus, 1 L is much less than 1 incident hydrogen atom per surface atom. Saturation of the work function occurs at about 1200 L, though data was collected beyond that. Changes in the work function are determined from the low energy cut-off in secondary electron spectra collected with an electrostatic analyzer (Comstock) while the sample is bombarded by 200 eV electrons [23]. Time-of-flight (TOF) ion scattering was carried out with a pulsed ion gun (Kimball Physics), employing a pulse width of about 20 ns. Scattered species were detected by a triple micro-channel-plate array in a backscattering geometry with a fixed scattering angle of 150°. The sample was positioned so that ions reaching the detector were from normal emission. The detector leg is equipped with deflection plates that can deflect all ions, allowing separate collection of total and neutral yield spectra. To calculate NF, the area of the single-scattering peak in the neutral spectrum is divided by that of the totals [16].

Measurements of work function and NF as the samples are dosed with hydrogen are displayed in Fig. 4.1. The NF and work functions of the clean surfaces are nearly identical. As hydrogen passivates the surface, the Fermi level becomes unpinned, and the work function decreases (for n-type) or increases (for p-type) to match the bulk value, due to the fact that the pinned Fermi level is 0.63 eV above the valence band maximum, nearly in the middle of the gap. This dependence of the work function on doping type indicates that the hydrogen adsorption is indeed unpinning the Fermi level. The values for NF shown in the bottom panel of Fig. 4.1, however, do not follow the work function trends. Instead, lightly doped samples of either dopant type have similar NF to each other, decreasing from about 25% to 18%, whereas the heavily n-doped samples were flat or marginally increasing

in the range of 30-35%, a result which is statistically significant. The fully passivated medium-doping value (not shown) was intermediate to these two values (see Fig. 4.3).

There are several factors that combine in determining the NF for scattered alkalis. When the projectile is far from the surface, the vacant s level is sharp and located at the ionization energy, but it shifts up when approaching the surface due to the electrostatic image potential. At the same time, the atomic wave function admixes with the wave functions of electrons in the solid, effectively broadening the ionization level. As such, these experiments can determine whether the band gap measurably affects the admixing of atomic and surface electronic states. If the density of states in the gap is truly zero, one may expect a dependence of the neutralization probability on doping, providing that most of the neutralization involves electrons in that energy range.

Our analysis is based on a jellium model of the substrate that has been successfully implemented for a qualitative interpretation of measured NFs [24]. We focus only on the passivated surface without dangling bond surface states. The interacting atom is described by its ionization level ψ_a, its ionization energy ϵ_a, and the virtual line-width Δ as functions of distance from the surface. The energy ϵ_a is the sum of the free atom ionization energy and the image charge shift saturated at the jellium boundary, and the value of Δ is determined by the jellium electron density. The substrate energy levels are described by their energy ϵ_k and the wave functions ψ_k. A microscopic model of Δ relates the broadening and the electron transfer matrix element V_{ak} between ψ_k and ψ_a via the approximate independent-particle golden rule formula $V_{ak}^2 \cong \Delta_a/\pi\rho$, where ρ is the density of electronic states of the substrate. V_{ak} is taken as independent of k, and is essentially, together with ϵ_a, the only

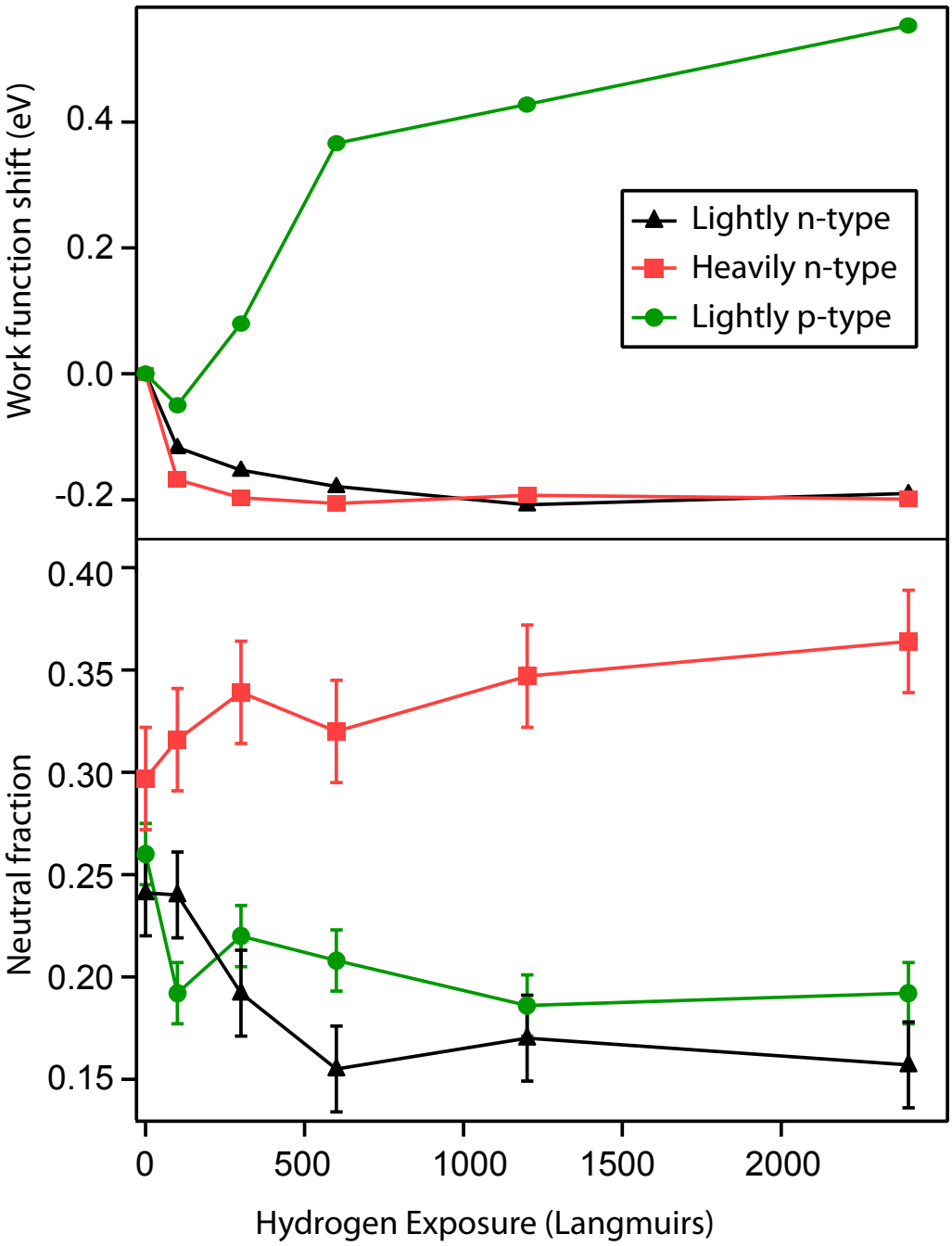

Figure 4.1: Work function shifts and neutral fractions for 3 keV Li^+ scattered from Si(111) surfaces as a function of H exposure.

parameter in the theoretical description of charge transfer in the low energy regime. This model agrees very well with experimental data for Li scattered from Cu with V_{ak} and ϵ_a deduced from the jellium model and using $r_s = 2.8$ au for the electron gas radius [25].

For Li scattered from Si, it is possible to approximate V_{ak} and ϵ_a by substituting for the corresponding jellium. Since the electron gas radius of Si, $r_s = 2$, is similar to the $r_s = 2$-2.8 used by Marston et al. for Li scattered from Al [25, 26], we use their values for V_{ak} and ϵ_a. The substrate is specified by the energy distribution of substrate k levels.

The level shift and broadening for Li is shown schematically as a function of distance from the surface in Fig. 4.2 alongside the Si band diagram. The model takes into account the change of NF with surface electronic structure by the inclusion of more levels in the conduction band as doping is increased. The band gap in Si narrows in the presence of dopants, which is attributed to the interaction of minority carriers with several majority carriers, thus reducing the barrier to exciton formation according to [4]

$$\Delta E_G = (3q^2/16\pi e) \cdot (q^2 n/ekT)^{1/2} = 22.5(n/10^{18})^{1/2} \text{ meV}. \tag{4.1}$$

For simplicity, we let the band gap narrowing lower the conduction band edge in the calculation.

We consider a wave function $|\phi(t)\rangle$ of the Li-Si system composed of the Si wave functions $|\psi_k\rangle$ in the bands around the gap and the atomic level $|\psi_a\rangle$, so that

$$|\phi(t)\rangle = \sum_k b_k(t)|\psi_k(r)\rangle + b_a(t)|\psi_a(r)\rangle. \tag{4.2}$$

where k runs over all levels in the solid under consideration. Referenced to the vacuum, energy levels are counted from the (arbitrary) value of -9.13 eV to the valence band edge

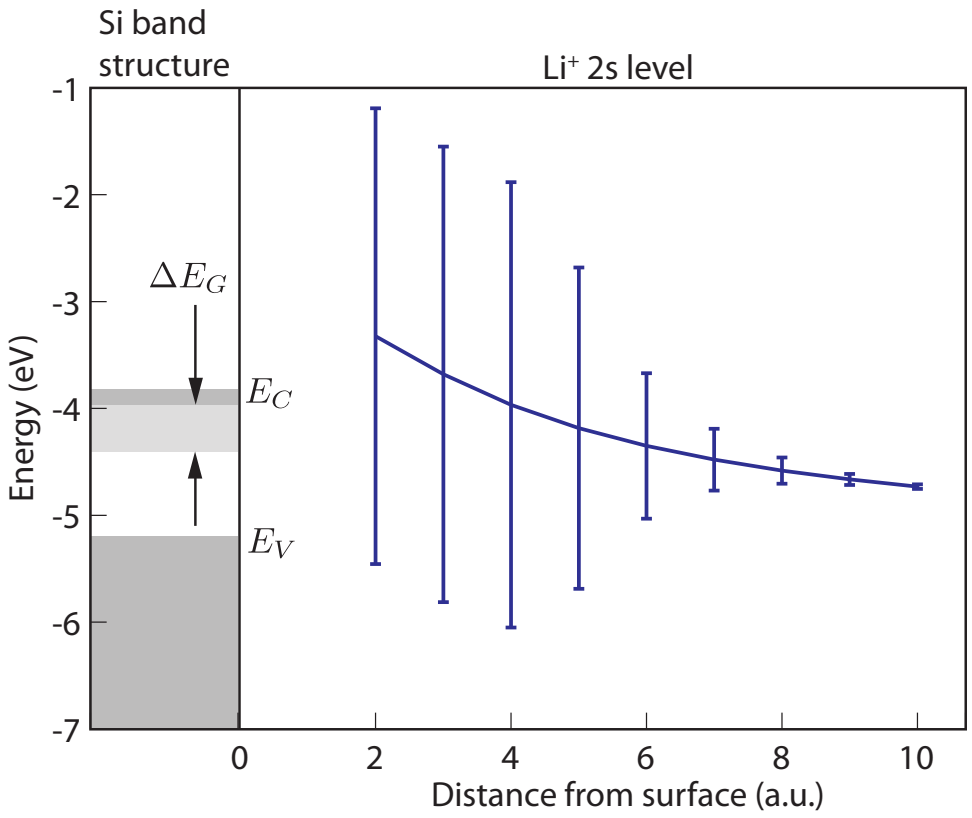

Figure 4.2: Right: The level position and broadening of the Li $2s$ as the ion approaches the surface. Left: a schematic of the band structure of fully passivated Si, showing the change in band gap with increased doping.

at -5.17 eV, and then from the conduction band minimum, as calculated from (4.1), to the vacuum level. For no band narrowing, the conduction band edge is taken to be -4.01 eV. Insertion of (4.2) into the Schrodinger equation gives a set of differential equations

$$\begin{cases} i\dfrac{db_a}{dt} = \displaystyle\sum_k b_k V_{ak} + b_a \epsilon_a \\ i\dfrac{db_k}{dt} = b_a V_{ak} + b_k \epsilon_k, \end{cases} \tag{4.3}$$

(in atomic units).

To calculate the NF of Li at the end of the scattering process, the independent particle approximation of the many-body problem is used, based on the solution to the Heisenberg equations of motion, which gives NFs that are in good agreement with experiment for alkalis scattered from metal surfaces [26, 27]. The solution of the time-dependent coefficients of the operators is equivalent to the solution of (4.3) for $b(t)$. For the initial prepared state of atomic and Si levels occupied up to the Fermi energy, the value of NF is given by NF $= \sum |b_k(\infty)|^2$, where the summation is over all occupied states. The values of V_{ak} and ϵ_a and their time dependence are taken from Ref. [25], with V_{ak} slightly larger by a factor of 1.4 to fit the asymptotic data for zero doping. The experimental and theoretical NFs for different dopings are shown in Fig. 4.3 slightly underestimating for low to intermediate doping and overestimating for high doping.

The simplest explanation for the marginal deviation is some persistent inhomogeneity in the hydrogenated surface. The evolution of the 7×7 surface as atomic hydrogen is dosed has been studied extensively [22]. Although quoted exposure figures are not directly comparable, the "fully passivated" dosages in this work are well beyond those in the literature at which steady state was reached. For such large exposures, the surface

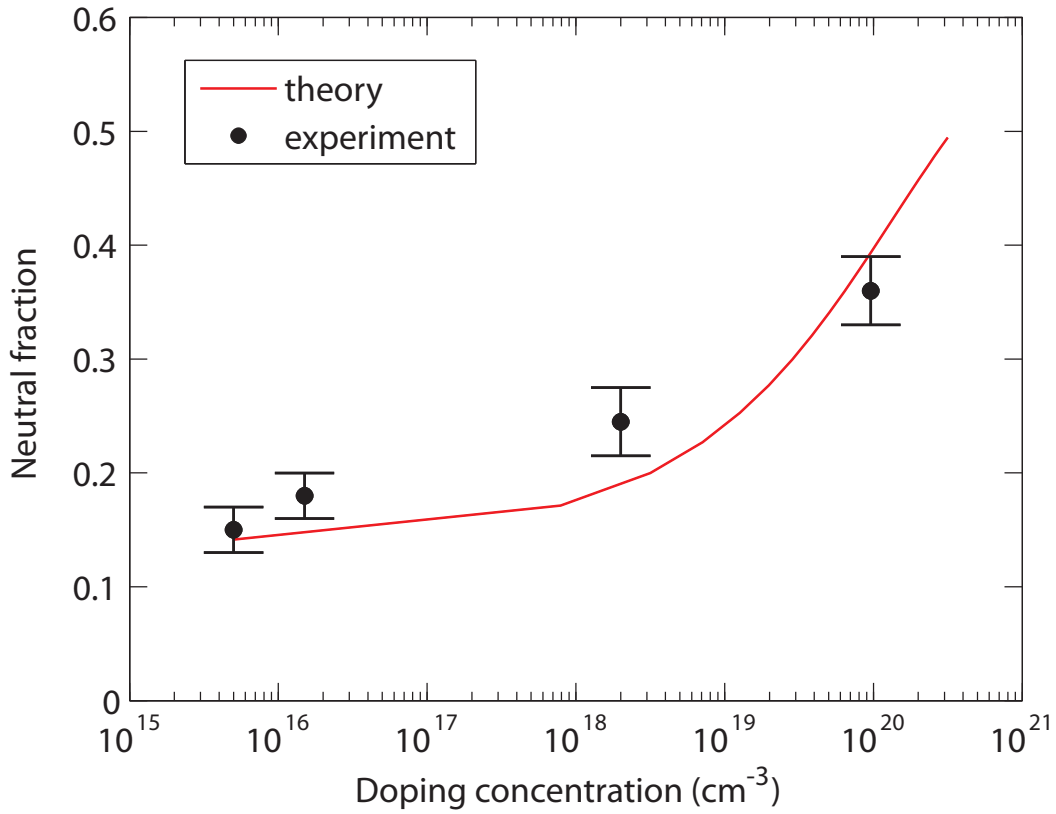

Figure 4.3: Measured neutral fractions (filled circles) for saturation coverage of H, along with the neutral fraction predicted by the solution to Eqns 4.3.

is etched by atomic hydrogen and a steady state population of monohydrides, dihydrides, and trihydrides is established, along with some newly created dangling bonds [28]. Ideally, a passivated (111) surface would be entirely composed of monohydrides, but this is not attainable.

The inhomogeneity, and therefore incomplete unpinning of the Fermi surface, will lead to saturation values that are a mixture of the predicted fully passivated values and those associated with a surface pinned by dangling bond states. Nominally, the pinned surface gives a NF around 27%. Thus, if some population of dangling bonds still exists, the predicted value will be too small for the low doping sample, and too large for the high doping samples, as observed.

Nevertheless, the agreement between the experiment and the model is striking, which demonstrates that the bulk band gap in a semiconductor is a large factor in the neutralization of scattered alkali ions. The fraction changes markedly with doping level, due to the band gap narrowing while leaving the work function virtually unchanged. A simple model captures the important features of the admixing of states quantitatively, implying that this effect is fundamental to charge exchange between atomic species and semiconductor surfaces. In some sense, the semiconductor can be thought of as a free-electron gas confined to a region with a jellium surface, but with electronic levels missing in the gap.

Bibliography

[1] B. E. Deal and M. Sklar, Journal of the Electrochemical Society **112** (4), 430 (1965).

[2] Hwaiyu Geng, *Semiconductor Manufacturing Handbook*. (McGraw-Hill Companies, 2005).

[3] Roland A. Levy, *Reduced Thermal Processing for ULSI*. (Plenum Press, Murray Hill, New Jersey, 1990).

[4] H. P. D. Lanyon and R. A. Tuft, IEEE Trans. Elec. Dev. **26** (7), 1014 (1979).

[5] H. F. Winters and D. Haarer, Phys. Rev. B **36** (12), 6613 (1987)

[6] F. A. Houle, J. Appl. Phys. **60** (9), 3018 (1986).

[7] G.F. Liu, Z. Sroubek, P. Karmakar, J.A. Yarmoff, J. Chem. Phys. **125**, (2006).

[8] H. W. Werner, Vac. **24** (10), 493 (1974).

[9] M. Szymonski, J. Kolodziej, Z. Postawa, P. Czuba, and P. Piatkowski, Prog. Surf. Sci. **48** (1-4), 83 (1995).

[10] J. Lee, Z. Zhang, J.T. Yates, Jr., Phys. Rev. B **79**, 081408 (2009).

[11] J. C. Tully, Ann. Rev. Phys. Chem. **51**, 153 (2000).

[12] E. A. Carter, K. Niedfeldt, and P. Nordlander, Surf. Sci. **600** (21) (2006).

[13] Andrew Schmitz, John Shaw, Himadri S. Chakraborty, and Uwe Thumm, Phys. Rev. A **81** (4) (2010).

[14] B.J. Garrison, A.C. Diebold, J.H. Lin, Z. Sroubek, Surf. Sci. **124**, 461 (1983).

[15] J. J. C. Geerlings, L. F. T. Kwakman, and J. Los, Surf. Sci. **184** (3), 305 (1987).

[16] C. B. Weare and J. A. Yarmoff, Surf. Sci. **348** (3), 359 (1996).

[17] Y. Yang and J. A. Yarmoff, Phys. Rev. Lett. **89** (19) (2002).

[18] A. R. Canario, T. Kravchuk, and V. A. Esaulov, New J. Phys. **8** (2006).

[19] F. J. Himpsel, Surf. Sci. **299** (1-3), 525 (1994).

[20] J. Los and J. J. C. Geerlings, Phys. Rep.-Rev. Sec. Phys. Lett. **190** (3), 133 (1990).

[21] C. J. Karlsson, E. Landemark, L. S. O. Johansson, U. O. Karlsson, and R. I. G. Uhrberg, Phys. Rev. B **41** (3), 1521 (1990).

[22] J. J. Boland, Adv. Phys. **42** (2), 129 (1993).

[23] H. E. Bauer and H. Seiler, Surf. Interface Anal. **12** (1-12), 119 (1988).

[24] P. Nordlander, J.C. Tully, Physf. Rev. B **42**, 5564 (1990).

[25] A. V. Onufriev and J. B. Marston, Phys. Rev. B **53** (20), 13340 (1996).

[26] J. B. Marston, D. R. Andersson, E. R. Behringer, B. H. Cooper, C. A. DiRubio, G. A. Kimmel, and C. Richardson, Phys. Rev. B **48** (11), 7809 (1993).

[27] R. Brako and D. M. Newns, Surf. Sci. **108** (2), 253 (1981).

[28] U. Jansson and K. J. Uram, J. Chem. Phys. **91** (12), 7978 (1989).

Appendix A

Binary collision mechanics

Suppose a particle of mass m_1 enters a region with initial velocity $\mathbf{v}_{10}$ and collides elastically with a particle m_2 which is initially at rest, as shown in Fig. 1.1. Suppose further that we care only about the final energy of the particle m_1. Then, because of conservation of energy and momentum,

$$m_1\mathbf{v}_{10} = m_1\mathbf{v}_{1f} + m_2\mathbf{v}_{2f} \tag{A.1}$$

$$\frac{1}{2}m_1v_{10}^2 = \frac{1}{2}m_1v_{1f}^2 + \frac{1}{2}m_2v_{2f}^2 \tag{A.2}$$

Rearrange the former equation and square

$$m_1(\mathbf{v}_{10} - \mathbf{v}_{1f}) = m_2\mathbf{v}_{2f} \Rightarrow m_1^2(v_{10}^2 + v_{1f}^2 - 2\mathbf{v}_{10}\cdot\mathbf{v}_{1f}) = m_2^2v_{2f}^2. \tag{A.3}$$

Call the scattering angle θ between $\mathbf{v}_{10}$ and $\mathbf{v}_{1f}$, and call $\mu = m_2/m_1$. Then,

$$v_{10}^2 + v_{1f}^2 - 2v_{10}v_{1f}\cos\theta = \mu^2v_{2f}^2. \tag{A.4}$$

From energy,

$$\mu v_{2f}^2 = v_{10}^2 - v_{1f}^2, \tag{A.5}$$

so

$$(1+\mu)v_{1f}^2 - 2v_{10}v_{1f}\cos\theta + (1-\mu)v_{10}^2 = 0, \tag{A.6}$$

and invoking the quadratic formula,

$$v_{1f} = v_{10}\left[\frac{\cos\theta \pm \sqrt{\mu^2 - \sin^2\theta}}{1+\mu}\right]. \tag{A.7}$$

The result is that the scattered kinetic energy of the projectile m_1 is

$$E_{1f} = E_{10}\left[\frac{\cos\theta \pm \sqrt{(m_2/m_1)^2 - \sin^2\theta}}{1+m_2/m_1}\right]^2. \tag{A.8}$$

Appendix B

Chamber 2 operations guide

B.1 Pump-down and venting procedures

B.1.1 Getting to high-vacuum

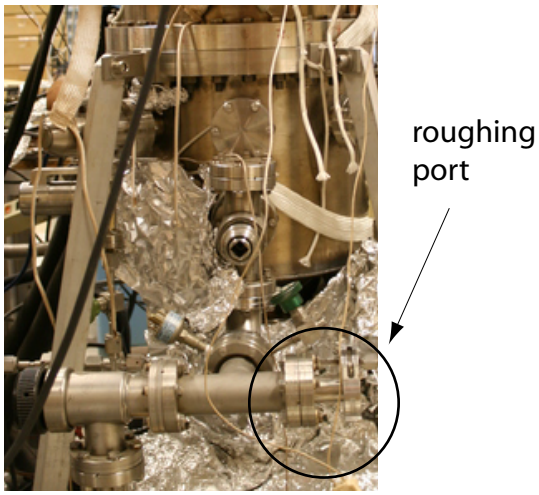

1. Attach oil-free diaphragm pump to indicated port. Let rough pump for 5-10 minutes or until very little air is coming out of the outlet.

2. With turbo pump at full rotations, open the gate valve to the baby chamber. Quickly

close the right-angle valve to the marked torque using a torque wrench. It is around 30 ft lbs at present. Replace the blank kwik-flange KF-25. Monitor the turbo controller to ensure there is not a huge leak.

3. Attach the small rough pump to the appendage ion pump kwik flange port. Evacuate the ion pump and then close the Nupro valve to it, but leave the other valve open. Switch on the appendage ion pump supply. The red LED should light for quite some time (hours, even), before the low-pressure regime is reached.

4. Turn on the baby-chamber ion gauge. This one can usually be left at the low-emission setting (0.1). Once it reads 1×10^{-4} torr, you can turn on the main chamber ion gauge.

5. Run the Ti sublimator for 5-10 minutes by turning the current up to at least 42 amps. This will pump very efficiently at higher pressures.

6. Once the main chamber pressure is below 1×10^{-5}, turn the ion pump controller switch to "start" and turn the unit on. Watch the pressure carefully. If it begins to rise above 1×10^{-5}, turn it off and let the turbo pump on it for awhile longer.

B.1.2 Baking

1. Remove cryogen transfer line (see Section B.2), XPS cover, and all cables from chamber.

2. The Mitotoyo micrometers on the VG manipulator should not be baked. To remove them:

   (a) Adjust the micrometers until the smaller hole in the manipulator "table" aligns

with a corresponding hole under it. Insert the immobilizing pin (despite it having threads, it does not need to be screwed into place).

(b) Remove the larger two bolts using a 5 mm allen wrench. The shop typically does not stock these, so losing one may mean a trip to the store.

(c) Remove the two bolts on the top/bottom with a 4 mm allen wrench, and remove the black mounting plate.

(d) Using a ball-ended 3 mm allen wrench, unscrew the two bolts holding the the micrometer while maintaining force between the dial and the receiving piece. This ensures that the two half-rings don't fall out.

3. Move the manipulator all the way up and remove the stepper motor.

4. Wrap a single layer of foil around the bellows. Wrap a long heating tape around it several times, leaving a gap of 2-3 inches between wraps.

5. Wrap heating tapes around the rest of the chamber walls, with 2-3 inch gaps, affixing them with high-temperature tolerant teflon-coated adhesive tape. Plug heating tapes into extension cords. Then, wrap aluminum foil around the whole chamber until the chamber walls themselves are not visible.

6. The chamber has 6 protected variable AC transformers (variacs) fused at 7.5A each. They will energize only if the ion gauge pressure is below the set-point, which can be changed by opening the ion gauge controller's front panel. 1×10^{-6} is a sensible setting. Plug extension cords into variacs, flip the on switch on each, and turn knobs to 30%.

7. Check each tape's current using the clamping (inductive) ammeter.

8. Turn up the bake-out over the course of a few hours, keeping the total current on each variac below the fused value. Run the Ti sublimator every couple of hours. Try to reach a uniform 200°C.

9. After 12-48 hours, turn the bake-out off. When the feedthrus have cooled enough, attach cabling to everything that has a filament and turn the filament to the operating current for a short time. Remove the cables before they melt.

10. Once the chamber is cool, turn the ion-gauge water cooling on by opening both the inlet and outlet valves. Then reattach the stepper motor, micrometers, and cables.

B.1.3 Venting

1. Turn off the ion gauge water cooling and wait for the tube to reach room temperature. Turn off the ion gauge, the ion pump, and anything else that is on.

2. Open the right-angle valve with the torque wrench, 20-25 turns, and attach a dry, clean source of nitrogen (the vent valve of a liquid nitrogen dewer is best). Open the Nupro valve. Monitor the line by pinching it every so often to make sure it collapses from the vacuum of the chamber. This will help keep you from overpressurizing the chamber. Overpressurizing is very bad.

B.2 Cryogenic cooling

1. Check the date of the last time the vacuum jacket of the transfer line was evacuated. It should be pumped out overnight once every 2-3 months. If needed, attach a KF-25

line to a chamber with a turbo pump and evacuate.

2. Insert the transfer line into manipulator by lowering the z-axis until the Faraday cup is just above the x-ray source, then lifting the line up and carefully inserting. Screw in a couple times.

3. Insert the other side into the dewer, making sure the o-ring is on. Screw down tightly, using channel locks if needed. Ensure that you can not hear nitrogen gas escaping.

4. Open the transfer line valve by twisting the brass fitting while keeping the transfer line itself stationary. 2 full turns is usually sufficient.

5. Pressurize the dewer if necessary to get cryogen to begin flowing.

6. The Janis manipulator does not have a built-in heater to keep it from icing during operation. This is bad, because ice will form, melt, and rust the bearings in the Thermionics rotary seal. To avoid this, put a small heating tape around the top of the manipulator and apply heat to make sure there is no ice forming on or around the rotary seal.

B.3 Ion scattering spectroscopy

1. Connect the ion gun to the power supply/pulser box.

2. Push “Power” and “Source”.

3. Turn source up to the running current (usually 1.42 for Na and 1.5 for Li).

4. Turn HV up to desired energy and lens to about 2/3 of that voltage.

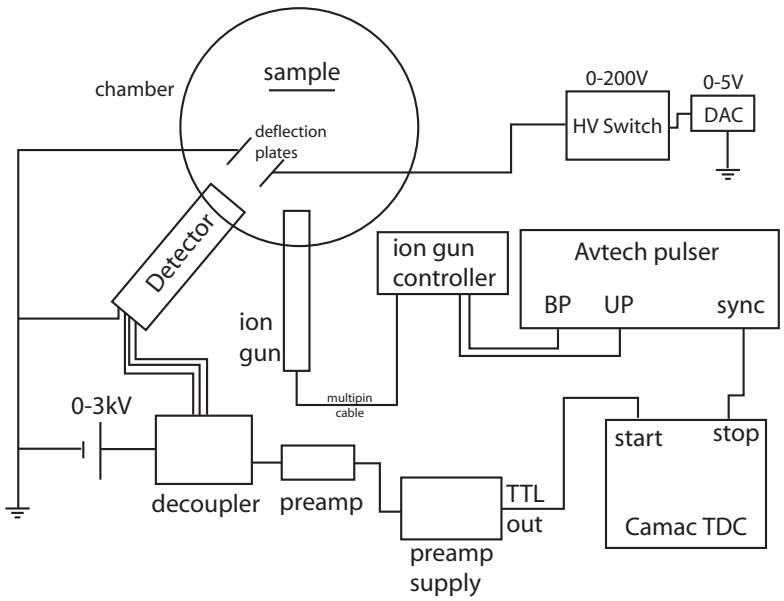

Figure B.1: Setup for time-of-flight spectroscopy. Imposing, isn't it?

5. Turn all deflection plates to 0.

6. Tune the lens by reading the sample current with a picoammeter.

7. Switch the picoammeter to the Faraday cup, ground the sample holder, and find the beam by moving the micrometers. Once found, focus the beam (maximize current) by iteratively adjusting lens, position, and deflection plate voltages. Leave $y-$ at 0V.

8. Find the width of the tuned beam by sweeping the Faraday cup across the beam in y and z directions. It should be less than 2 mm, measuring the full width at 10% of the maximum.

9. Attach the decoupling box to the channel plate detector, along with a grounder to the "front" feedthru. Connect a +0–3 kV supply to the input of the decoupling box

and the preamp to the preamp power supply. Wrap foil around everything.

10. Connect the Avtech pulser to the pulser box. Since we left $y-$ at 0, that should be the unipolar. At the time of this writing, I was usually using $x-$ as the bipolar. Ensure, using a 10x AC probe in an oscilloscope, that the peak-to-peak voltage is at least 100V on the unipolar, and that $f = 80$ kHz.

11. With the preamp power supply OFF, turn on the HV channel plate supply to 2.97 kV. Then turn on the preamp power supply. Observe this rule when turning on or off: the preamp should never be on during one of these operations.

12. Flip the switches on the two pulsing channels to the "pulse" setting.

13. Connect the preamp TTL output to the counter channel of the DAQ card and read the counts vs. time in Scanninator. Compare the dark counts to the pulsed ion beam signal by turning $y-$ to its maximum, and toggling it between static and pulsed modes (this effectively blanks the beam when on the static setting). Adjust the discriminator on the preamp by turning the trim pot. Maximize the signal to noise.

14. Connect the TTL sync from the Avtech to the "stop" on the CAMAC TDC. Connect the preamp TTL output to the "start" of the CAMAC TDC.

15. Connect the HV switch box to one deflection plate and ground the other. Connect the TTL input of the switch box to one of the DACs on the NI DAQ board.

16. Take data with GetTOF.

Note: The rise time of the Avtech can be adjusted by putting a potentiometer in between the pulsing box BP line and the gun. The RC time constant is $\tau = (Z_{\text{out}} + R) \times C$. The

Avtechs have output impedance 50Ω and drive a load of capacitance ≈ 100 pF, resulting in a rise time of ≈ 20 ns. If you add a resistance R equal to 1 kΩ, you will get a rise time of about $2.2 \times 1050 \times 100 \times 10^{-12} = 231$ ns. This is about ten times the rise time without R.

B.3.1 Channel plate detector

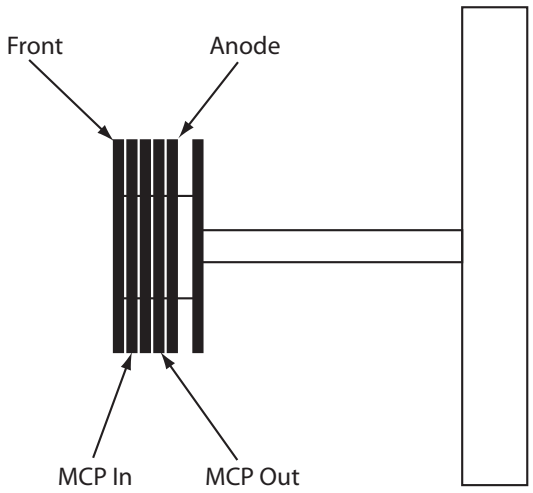

Figure B.2: Schematic of the channel plate detector. The channel plates themselves (not shown) are squeezed between each plate from MCP In to MCP Out.

The microchannel plate detector (see Fig. B.3.1) is comprised of several plates that serve to hold and apply voltages to multiplier plates made by Burle. The front is normally held at ground, and has a fine steel mesh to filter stray fields. MCP In, similarly, is normally held at ground. A high positive voltage is applied to MCP Out, which creates a potential that draws electrons created in the plates down to the anode, where they are collected. Burle rates their plates at 1000V, and they operate fine at 900V when new.

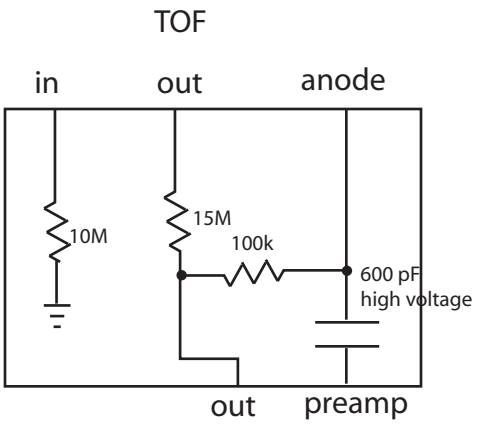

Figure B.3: Wiring diagram for the TOF decoupling box. The capacitor should be able to hold at least 600V. There is a large stock of them in the "Preamp Stuff" drawer.

Chamber 2, having 3 channel plates, uses a voltage of 2.97kV, slightly less than the rated maximum.

B.3.2 TOF Decoupling Box Schematic

B.4 X-ray photoelectron spectroscopy

1. Connect the XPS cover by pulling the cables thru, connecting the two quick-connect water lines *firmly*, and connecting the two electrical lines by tightening the nut that holds the spade onto a threaded rod (I like to use a 7/16" nut driver for this). The longer wire goes to the upper connector.

2. Turn on the chiller by flipping the switch on the back. Check the water pressure (should be around 50) and make sure there is no low-level warning. If there is, unscrew the gray plug on top and pour in some deionized water.

3. Connect the multipin "X-ray source" cable to the source, and the lug to a good ground.

4. Make the 4 necessary connections on the analyzer: the anode box, the input box, the multipin connector, and the decoupler/preamp connection. Make sure the preamp is connected to the preamp supply.

5. Turn on the main power switch on the back of the XPS rack (near the bottom).

6. On the x-ray filament control, press "on", then 1f, then turn the filament up to 3.4A slowly.

7. Carefully move the manipulator to the XPS position. Once there, put lead over the nearby windows to limit radiation exposure.

8. Increase HV to 10kV on the x-ray HV control.

9. Turn on Main Power and HV on Scan Generator.

10. Turn on TCE300, and with the preamp supply OFF, push V-multi in.

11. Turn on the preamp supply.

12. Scan with the computer. To read in voltage, use factor 200.06 and offset -2.96. To see binding energy, you can use 200.06 and -1245.76 as the offset, and then scan from -900 to $+20$, interpreting negative numbers as positive binding energies. This is unfortunately necessary because Scanninator cannot scan backwards while plotting forwards.

13. To refine the sample position, maximize the signal of the peak of interest. This could be done by setting the DAC to the peak position and reading counts as a function of

time while one manipulated the lens and sample position. However, I find this doesn't work well, as the background may increase along with the peak height itself. What you really need to do is compare the peak height to a nearby (non-peak) position's countrate. I have written a small Labview routine to do this, which should be on the computer. Simply input the voltage of the peak and of a nearby voltage, and it will read out the S/N as a function of time.

Note: At the time of this writing, the Al/Mg switch does not operate, and we have only been plugging in the Mg cable. To switch to Al, one would have to shut the machine down, and swap the Al cable for the Mg cable, then turn it back on.

B.5 Work function measurement

Comstock Electron Gun

Pin	ID	color
1	-y	brown
2	+x	dark blue
3	+y	yellow
4	-x	green
5	gnd	alligator clip
6	anode	dark brown
7	fil	white
8	lens	light blue
9	fil	dark blue

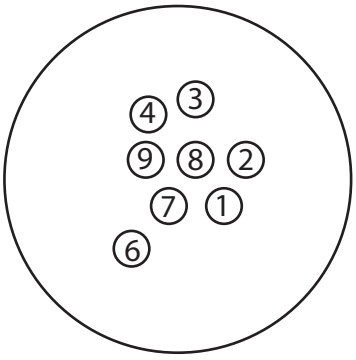

Figure B.4: Comstock electron gun wiring diagram. Many of the sockets have text labels in addition to color code.

1. Connect the e-gun as indicated. The alligator clip can be connected to any good ground (usually a nearby bolt is ok).

2. Connect a supply to the HV input of the e-gun supply (-200V is usually ok for WF). This supplies the electron energy. Turn on the filament. As of this writing, the gun has a .010" tungsten filament made to run 6-8A, although I usually need less than this to get the desired beam current (200 nA).

3. Tune the e-gun.

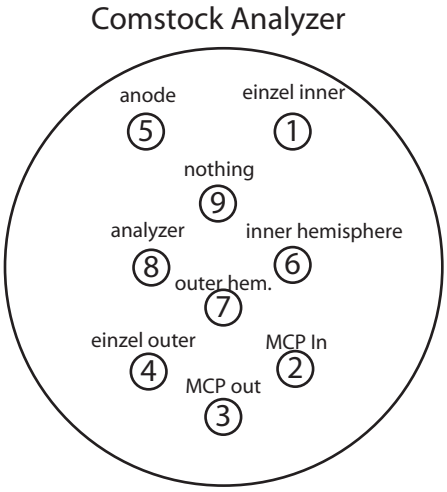

Figure B.5: Schematic of the Comstock Analyzer flange.

4. Connect the Comstock Analyzer as shown in Fig. B.5 (You may want to have the e-gun off during this. It's a relatively high voltage completely exposed. I have shocked myself doing this.).

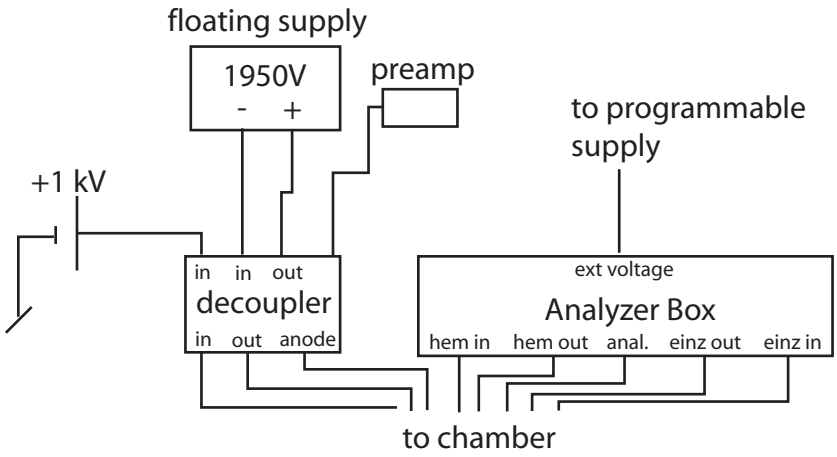

Figure B.6: Setup for work function measurement with the Comstock e-gun and analyzer. The front of the channel plate detector is floated with respect to ground to attract electrons into the analyzer.

5. Connect -20V to the sample.

6. Set pass energy on the analyzer box by grounding "ext voltage" and measuring the voltage on Hem. In. and Hem. Out, then setting according to

$$\pm V = \frac{\pm\text{pass energy}/2}{2.252}.$$

E.g. for measuring electrons with a 10 eV pass energy you want $+2.2$V on the inner and -2.2V on the outer.

7. Scan with computer. Note that the ramping voltage floats the analyzer, and that electrons of energy equal to the pass energy get thru. So, for 20 eV electrons, the cutoff signal will be around $V_{\text{ext}} \approx -10$V. For 50 eV pass energy and -20V on the sample, you actually have to ramp through *positive* 30V to see the cutoff.

B.5.1 Comstock Analyzer Repair

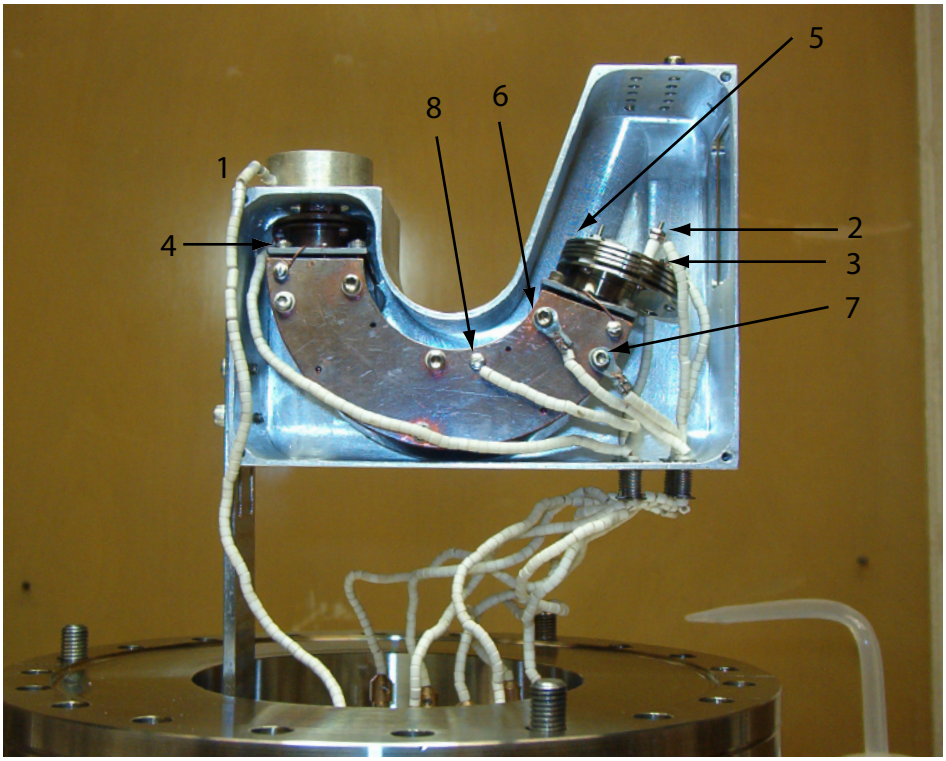

Figure B.7: Photo of the inside of the Comstock hemispherical analyzer. Numerical labels correspond to those in Figure B.5.

The Comstock analyzer is mounted on a 8" flange port by way of a 6" to 8" zero length adapter flange. The 6" flange cannot itself be removed from the adapter from the outside, so to remove it from the chamber, you must remove the 8" flange. This is easier said than done, because the analyzer actually hangs below the level of the opening. Hence, one has to do a lot of wiggling to get it in and out, which can easily break the insulating ceramics. I have no advice; this just sucks.

The analyzer can be finicky to work on. The hemisphere (shown in Fig. B.7) is mounted inside an aluminum shield by way of threaded insulators. At this time, they are

made of Macor, as they had to be replaced at least once. They are held into these insulators by several partially threaded rods. These must be screwed in just enough to hold well, but not so much that the threads ground out the analyzer.

The inner einzel lens connection (1 in the figure) is also a pain. The ceramic that isolates the wire can slip in and out of the hole, and special attention should be paid to this each time the analyzer is worked on. Check that this is not grounded every step of the way as you put it back in the chamber.

B.5.2 Analyzer Decoupling Box Schematic

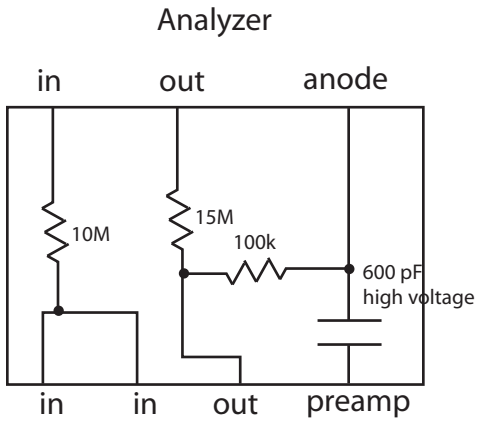

B.6 Depositing materials

B.6.1 Bromine

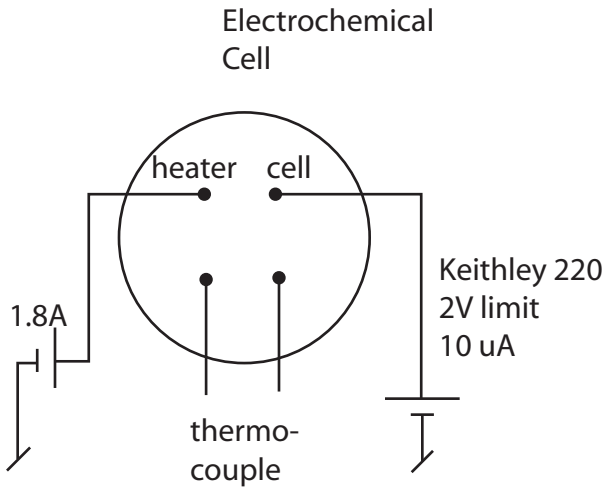

Hook up the electrochemical cell as shown. The Keithley 220 is a precise source of small current. Set the voltage limit to 2V and then set the current to constant 10 μA. An exposure of 1 $\mu\text{A} \cdot \text{min}$ is equivalent to 1.8×10^{14} molecules leaving the cell.

B.6.2 Gold

Each time the gold evaporator is refilled, a calibration with the QCM is required. If the calibration is already done, refer to the graph (such as Fig. B.8), set the desired current using the Lambda supply, set the voltage to something high (maybe 3V), let the evaporator warm up, then open the shutter for the desired time. Normally you want to wait until the growth rate flattens out, then open the shutter.

To recalibrate:

1. Move the QCM in front of the evaporator (in chamber center) and open the shutter.

2. Connect the cooling water lines to the QCM, and open the valves. Connect the QCM electronics.

3. Set the QCM to the density and Z factor of Au (listed in the QCM manual).

4. You first need to wet the filament. Do this by setting the Lambda current to a nominal amount much less than the current of the previous calibration (say, 18A) and set V to 3V. Verify that there is no growth on the QCM.

5. Increase the current in steps of 0.1 A, every 15 seconds or so, by pushing the up arrow on the supply in current mode. Eventually, you'll hit a certain current where the voltage will rise and evaporation will begin at a relatively high rate. This indicates the filament has been wet.

6. Using the down arrow, reduce the current until the rate is about 1 Å per minute. Note this value.

7. Turn off the machine and let the evaporator cool down (for perhaps 20 minutes).

8. Zero the QCM controller, set the current to the previous value, and turn up the voltage. Record the time of each growth step (1 Å, 2 Å, etc.) for at least 15 minutes.

9. Plot growth vs time. Linearly interpolate between points to get a consistent time step. In Matlab I would use

   ```
   interp1(timevals,amountvals,[0:60:15*60])
   ```

   where timevals held the time in seconds of each growth step, amountvals was the number of angstroms. This returns a vector that holds total growth at 1 min, 2 min, etc.

10. Take a derivative of this and plot growth rate vs time, as seen in Figure B.8.

11. Repeat at a different current, if necessary, by letting it cool down and then set the new current. It may take a few tries to zero in on an acceptable growth rate (one that isn't fast or slow, or doesn't require waiting too long to warm up).

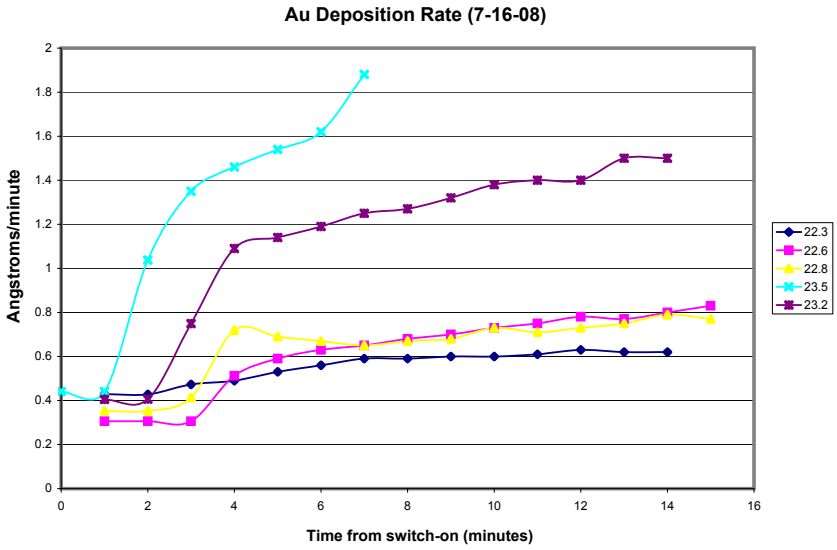

Figure B.8: Au growth rate vs time for different current settings. The ideal setting indicated in this calibration is to use 22.3A, wait for 7 minutes, then open the shutter. This would result in a fairly constant growth rate of 0.6 Å per minute (i.e. 0.01 Å per second).

B.6.3 Alkalis (Na and K)

Connect the Lambda or other source to either the upper-left connector (for Na) or upper-right connector (for K) and the lower (common) feedthru. With the sample turned away, turn on the current to 6.5A for 60s (6.87A if using another, more accurate supply). Then turn the sample toward the getter for the desired amount of time.

Appendix C

A calculation of neutralization of Li from Si

To calculate the neutralization of Li scattered from Si surfaces, we start with a trial wave function, and generate a system of differential equations in terms of the energy levels and the matrix element V_{ak} of a perturbing potential. We then calculate V_{ak} by way of 1st order perturbation theory, and making some reasonable assumptions.

The wave function is a linear combination of orthonormal functions $|\psi_1\rangle$, $|\psi_2\rangle$, ..., and $|\psi_a\rangle$:

$$\phi(t) = \sum_k b_k(t)\,|\psi_k(r)\rangle + b_a(t)\,|\psi_a(r)\rangle \tag{C.1}$$

where $k = 1, 2, \ldots$ are the levels in the Si and a denotes the atomic orbital. The Schrodinger equation in atomic units is

$$i\frac{\partial\phi(t)}{\partial t} = H(t)\phi(t). \tag{C.2}$$

Substituting (C.1) into (C.2) yields

$$i\sum_k \dot{b}_k \left|\psi_k\right\rangle + i\dot{b}_a \left|\psi_a\right\rangle = (H_0+V)\left(\sum_k b_k \left|\psi_k\right\rangle + b_a \left|\psi_a\right\rangle\right) \tag{C.3}$$

where H_0 is the unperturbed Hamiltonian, V is the perturbing potential, and dot denotes time derivative. We now take the inner product with $\langle\psi_a|$ to get

$$i\sum_k \dot{b}_k \left\langle\psi_a\right| \left.\psi_k\right\rangle + i\dot{b}_a \left\langle\psi_a\right| \left.\psi_a\right\rangle = \left\langle\psi_a\right| (H_0+V)\left(\sum_k b_k \left|\psi_k\right\rangle + b_a \left|\psi_a\right\rangle\right) \tag{C.4}$$

The orthonormality requirement is that $\langle\psi_a|\,\psi_a\rangle = 1$ and $\langle\psi_a|\,\psi_k\rangle = 0$. Defining

$$V_{ak} = \left\langle\psi_a\right| V \left|\psi_k\right\rangle,$$

$$\epsilon_a = \left\langle\psi_a\right| (H_0+V) \left|\psi_a\right\rangle,$$

we find

$$\begin{aligned} i\dot{b}_a &= \sum_k b_k \left\langle\psi_a\right| (H_0+V) \left|\psi_k\right\rangle + b_a \left\langle\psi_a\right| (H_0+V) \left|\psi_a\right\rangle \\ &= \sum_k b_k \left\langle\psi_a\right| H_0 \left|\psi_k\right\rangle + \sum_k b_k V_{ak} + b_a\epsilon_a \end{aligned} \tag{C.5}$$

But note that

$$H_0 \left|\psi_k\right\rangle = \epsilon_{0k} \left|\psi_k\right\rangle. \tag{C.6}$$

Then,

$$i\dot{b}_a = \sum_k b_k V_{ak} + b_a\epsilon_a. \tag{C.7}$$

Now take $\langle\psi_j|$ on both sides of (C.3) to find

$$i\left\langle\psi_j\right| \sum_k \dot{b}_k \left|\psi_k\right\rangle + i\left\langle\psi_j\right| \dot{b}_a \left|\psi_a\right\rangle = \left\langle\psi_j\right| (H_0+V) \sum_k b_k \left|\psi_k\right\rangle + \left\langle\psi_j\right| (H_0+V) b_a \left|\psi_a\right\rangle \tag{C.8}$$

But using $\langle\psi_j|\,\psi_k\rangle = \delta_{jk}$,

$$i\dot{b}_j = b_j \left\langle\psi_j\right| H_0 \left|\psi_j\right\rangle + b_j \left\langle\psi_j\right| V \left|\psi_j\right\rangle + b_a V_{ja} \tag{C.9}$$

Presuming that $\epsilon_j = \langle\psi_j| (H_0 + V) |\psi_j\rangle$, I find (taking $j \to k$)

$$i\dot{b}_k = b_k\epsilon_k + b_a V_{ka} \tag{C.10}$$

We thus have the system

$$\begin{cases} i\dfrac{db_a}{dt} = \displaystyle\sum_k b_k V_{ak} + b_a\epsilon_a \\ \\ i\dfrac{db_k}{dt} = b_k\epsilon_k + b_a V_{ka}. \end{cases} \tag{C.11}$$

consisting of a set of $n+1$ ordinary differential equations, where there are n electron orbitals under consideration in the silicon, and $k = 1 \ldots n$.

Making the substitution

$$b_k = c_k e^{-i\epsilon_k t}, \tag{C.12}$$

so that

$$\frac{db_k}{dt} = \left(\frac{dc_k}{dt} - i\epsilon_k c_k\right) e^{-i\epsilon_k t}, \tag{C.13}$$

we find for the second equation, for all k,

$$i\left(\frac{dc_k}{dt} - i\epsilon_k c_k\right) e^{-i\epsilon_k t} = \epsilon_k c_k e^{-i\epsilon_k t} + b_a V_{ak} \tag{C.14}$$

or

$$\begin{cases} i\dfrac{db_a}{dt} = \displaystyle\sum_k c_k V_{ak} e^{-i\epsilon_k t} + b_a\epsilon_a \\ \\ i\dfrac{dc_k}{dt} = b_a V_{ak} e^{i\epsilon_k t}. \end{cases} \tag{C.15}$$

The only things we have to describe to calculate the system Eqns C.15 are the energy levels ϵ_k under consideration, the energy level ϵ_a as a function of z, the initial wave functions, and, most importantly, V_{ak}. The former 3 are rather easy to approximate, but the final one is not.

In 1st order perturbation theory, the transition rate of a state with perturbation V is given by Fermi's Golden Rule

$$\Delta(z) = 2\pi \sum_k \rho(\epsilon_a)|V_{ak}|^2, \tag{C.16}$$

in atomic units ($\hbar = 1$). If we assume that V_{ak} is real and does not vary much over the levels under consideration, then we can take all the terms out of the sum and obtain

$$\Delta = 2\pi\rho(\epsilon_a)|V_{ak}|^2 \sum_k 1 = 2\pi\rho(\epsilon_a)|V_{ak}|^2 M \tag{C.17}$$

where $2M$ is the number of discrete levels under consideration. The density of states is $\rho = M/D$ for flat band half width D. This allows for rearranging to obtain

$$V_{ak}^2 = \frac{\Delta}{2M\pi\rho}. \tag{C.18}$$

To make use of this, we need an independent calculation of the resonance width, as given in Nordlander and Tully. However, it is more convenient to use the expression given in Marston(Phys. Rev. B **53** (20), 13340 (1996)):

$$\Delta = \frac{\Delta_0}{(e^{4\alpha z} + (\Delta_0/\Delta_{\rm sat})^4 - 1)^{1/4}} \tag{C.19}$$

The actual calculation can be handled by this code in Matlab.

Main program: elex6a3.m

```
function elex6a3;
%dynamic electronic interaction on a
%semiconductor surface with a gap.

% energies of electronic levels of the H:Si substrate


%the number NumbLevels of electronic levels in the
%valence band (0-100)
```

```
%and in the conduction band (101-200)
%The level (201) is Li ionization level and is described in odefun132.
%Energies env of  Si levels are in eV and en
%are in atomic units.
%The energy of the Li level is Ea and the
%interaction of the Li level with  Si levels
%is u  (see odefun132)


%4.02 eV is the cond band edge below vac level
%1.18 eV is the band gap
%I think 4 is arbitrary

NumbLevels=200;
nn=2*NumbLevels;
for nv=1:1:NumbLevels; % makes env be 100 x 1,
 % containing numbers from -9.13 to -5.17.
 env(nv)=nv*(4/NumbLevels)-4-4.05-1.12;
 end % corresponds to the first 100 levels below the valence band
     % edge counting by 0.04 eV
for nv=NumbLevels+1:1:nn;
 env(nv)=nv*(4/NumbLevels)-4-4.05-.225;
end %Corresponds to the levels above the band gap (above E_C)
en=env'*(1/27.2); %convert to Hartrees



%initial conditions ini:the level 201 (the ionization
% energy of Li) is not occupied
% at t=-infinity.The purpose is to find out the probabilities that
%electrons from  the valence band levels and
%possibly (for the n-doped Si)from a few
%levels in the conduction band are transferred to 201 and occupy the level
%201 at time t=+infinity. This time is equal to t=tend=2000 in our case.The
% absolute values of b(nv,t) squared is equal to the probability that an
% electron from the level nv occupies the level 201 at t. To
% calculate b(nv,t) we have to solve a set of
% linear differential equations:

%i*(d b(nv,t))/dt=b(201,t)*u*exp(i*en(nv)*t)
%i*(d b(201,t))/dt=b(201,t)*Ea(t) +u*sum((b(nv,t)*exp(-i*en(nv)*t))


%With initial conditions
inip=zeros(1,(nn+1));
```

```
 inip(nn+1)=1;
 ini=inip';
 ini
 en


 %The calculation is carried out  to find b(tend,nn).  |


    tend=2000;

%the calculation:
%The DE is defined in odefun132
%The domain for the solution is time 0 to 2000
%initial values for b are given by ini
%Absolute tolerance 10^-12, Relative tolerance 10^-9
%en and nn are passed along as constants
b=ode45(@odefun132,[0,tend],ini,...
odeset('AbsTol',1e-12,'RelTol',1e-9),en,nn);

t=0:1:tend;
gg=deval(b,t);
xx=deval(b,tend);

yy=abs(xx);
yyy=yy.*yy
save yyy yyy

%yyy(nv) is equal to the probability that an electron
%from nv occupies 201 at
%t=tend. thus the neutralization of Li scattered from H:Si is the sum of
%yyy from 1 to 100(Fermi energy of pure H:Si).With n-doping the
%occupation of levels 101,102
%etc must be added.
```

The ODE function:

```
function pp=odefun132(t,p,en,nn);


%the velocity v of the Li projectile at 3000 eV is 0.132 atomic units. The
% perpendicular velocity is .132*cos(30*pi/180) = 0.114.
% Atomic units measure mass in mass of electron, which is
% 0.000548579867 amu.
```

```
vin=0.1143;
vout=0.0824;
if(t < 1000)
    z=(t-1000)*vin;
else
    z=(t-1000)*vout;
end


%energy(in a.u.) Ea of the level 201 as a function of
% z and thus of t
Ea=(-5.39/27.2)+1/(sqrt(16*z*z +(27.2*27.2)/(2.6*2.6)));

% the matrix element of the time dependent perturbation
% potential between the level 201 and any level of the
% substrate (in a.u.)is u.The
% amplitude of u is chosen such that the width of the virtual level of Li
% is about 4eV at z=0 ,i.e. at t=1000.
%u =(1/27.2)*(0.24/1.41)/(cosh(0.42*z)*sqrt(2));
rho=200*27.2/3.96;
u=2*sqrt(2.23/(pi*rho*(exp(4*0.86*abs(z))+(2.23/.04)^4-1)^(1/4)));

%definition of the right sides of the time/dependent Schrodinger eq.
ac = cos(en*t);
as = i*sin(en*t);
uimp=zeros(nn+1);
uimp(nn+1,1:nn)=-i*u*((ac-as));
uimp(1:nn,nn+1)=-i*u*(ac+as);
uimp(nn+1,nn+1)=-i*Ea;
uimp;
p;

uimp;
pp=uimp*p;
pp;
```

The result of these functions is to create a file yyy.mat that contains the neutralization from each energy level. Summing over all filled levels will thus give you the neutral fraction.

Appendix D

Poisson statistics and calculating neutral fractions

The algorithm given at the end of this section integrates the total and neutral yield peaks, and then estimates the error in this determination. The error relies on the deviation due to counting statistics, known as shot noise. We first prove that the standard deviation is the square root of the number of counts obtained.

The probability of v successes, according to the binomial distribution, is

$$P(v) = \frac{N!}{(N-v)!v!} p^v (1-p)^{N-v} \tag{D.1}$$

which can be rewritten slightly as

$$P(v) = \frac{N!}{N^v (N-v)!} \frac{(Np)^v}{v!} \left(1 - \frac{Np}{N}\right)^N \left(1 - \frac{Np}{N}\right)^{-v} \tag{D.2}$$

Concerning ourselves with the first factor, we can employ the Stirling formula

$$\ln x! \approx x \ln x - x \tag{D.3}$$

for large x, which is certainly the case for all the terms here. Taking the natural log of the first factor, then,

$$\ln\left(\frac{N!}{N^v(N-v)!}\right) \approx [N\ln N - N] - [v\ln N] - [(N-v)\ln(N-v) - (N-v)].$$

After gathering terms, we find this is equal to

$$(N-v)\ln\left(\frac{N}{N-v}\right) - v = -\left(1-\frac{v}{N}\right)\ln\left(1-\frac{v}{N}\right)^N - v.$$

Neglecting v/N compared to 1 and recalling from calculus that

$$\lim_{N\to\infty}\left(1-\frac{v}{N}\right)^N = e^{-v},$$

this simplifies to

$$-\ln\left(e^{-v}\right) - v = v - v = 0.$$

Thus the first factor in P is 1:

$$P(v) = \frac{\mu^v}{v!}\left(1-\frac{\mu}{N}\right)^N\left(1-\frac{\mu}{N}\right)^{-v}, \tag{D.4}$$

where I have substituted the expectation value $\mu = Np$. Two more simplifications

$$\left(1-\frac{\mu}{N}\right)^N \approx e^{-\mu} \qquad \left(1-\frac{\mu}{N}\right)^{-v} \approx 1$$

and we obtain, finally,

$$\mathcal{P}(v) = \frac{\mu^v}{v!}e^{-\mu}. \tag{D.5}$$

This is the **Poisson Distribution**. It gives the range of values one would read for a system with a large number of trials, but a small number of successes. The average value for this

distribution is

$$\begin{aligned}\langle v\rangle &= \sum_{v=0}^{\infty} v\mathcal{P}(v) = \sum_{v=0}^{\infty} ve^{-\mu}\frac{\mu^v}{v!} \\ &= \mu e^{-\mu}\sum_{v=1}^{\infty}\left(\frac{v}{v!}\right)\mu^{v-1} = \mu e^{-\mu}\sum_{v=1}^{\infty}\frac{\mu^{v-1}}{(v-1)!} \\ &= \mu e^{-\mu}e^{\mu} = \mu.\end{aligned} \tag{D.6}$$

We are after the standard deviation, σ, given by

$$\sigma = \left\langle v^2\right\rangle - \langle v\rangle^2 \tag{D.7}$$

so we must also calculate $\left\langle v^2\right\rangle$, which we do by application of the derivative trick:

$$\begin{aligned}\left\langle v^2\right\rangle &= \sum_{v=0}^{\infty} v^2\mathcal{P}(v) = \sum_{v=0}^{\infty} v^2e^{-\mu}\frac{\mu^v}{v!} \\ &= e^{-\mu}\sum_{v=0}^{\infty} v^2\frac{\mu^v}{v!} = e^{-\mu}\left(\mu\frac{\partial}{\partial\mu}\right)\sum_{v=0}^{\infty} v\frac{\mu^v}{v!} \\ &= \mu e^{-\mu}\left(\frac{\partial}{\partial\mu}\left(\mu e^{\mu}\right)\right) = \mu e^{-\mu}\left(e^{\mu}+\mu e^{\mu}\right) \\ &= \mu + \mu^2.\end{aligned} \tag{D.8}$$

Thus, we obtain that

$$\sigma^2 = \mu \quad \Rightarrow \quad \sigma = \sqrt{\mu}. \tag{D.9}$$

By taking a single measurement, say $v_0 = \mu$, we determine the entire shape of the distribution.

The Matlab function NF is listed below.

```
function foo=nf(s, peakwidth, slope, peakval)

% frac=nf(s, peakwidth, slope, peakval)
% s is either a string path to a file or it is the Nx3 matrix of
```

```
% time-of-flight data. If a string, data will be loaded from disk.
% peakwidth: the desired half-width of the peak
%% slope: If not specified, slope will be found using
% linear interpolation between
% data points. If specified, constraining point is nearest
% to peakval - width
% peakval: The t value for the peak. If not specified, will be found
% automatically

%Version 0.2, 6/10/2010 R.G.
    %Fixed bugs with integration and drawing when the points weren't
    %interpolated. Was giving negative integrated area.
%Version 0.1, 6/4/2010 R.G.
    %Initial version

if(size(s,1)==1)
    [x,y]=hdrload(s);
else
    y=s;
end

times=y(:,1);totals=y(:,2);neutrals=y(:,3);
tstep=times(2)-times(1);

% Find desired indices
if(exist('peakval'))
    [temp,peakindex]=min(abs(times-peakval));
    peakheight=totals(peakindex);
    fprintf('Peakval is %g counts at t=%g\n',peakheight,times(peakindex));
else
    [peakheight,peakindex]=max(totals);
    fprintf('Finding peak automatically: Peakval
    is %g counts at t=%g\n',peakheight,times(peakindex));
end
x1=times(peakindex)-peakwidth;
[temp,x1minus]=min(abs(times-x1));
if(x1 < times(x1minus))
    x1minus=x1minus-1;
end

% For now, I'll always constrain based on (x1,y1)
% The below values for y1 are found by simply linearly
%interpolating between data
% points. They do not correspond to y values that the data actually have.
y1=((totals(x1minus+1)-totals(x1minus))/tstep)...
```

```
*(x1-times(x1minus))+totals(x1minus);
y1neu=((neutrals(x1minus+1)-neutrals(x1minus))/tstep)...
*(x1-times(x1minus))+neutrals(x1minus);
if(~exist('slope'))
    %Auto-detect slope based on the peak half-width.
    x2=times(peakindex)+peakwidth;
    [temp,x2minus]=min(abs(times-x2));
    y2=((totals(x2minus+1)-totals(x2minus))/tstep)...
*(x2-times(x2minus))+totals(x2minus);
    slope=(y2-y1)/(x2-x1);
else
    %   If slope is enforced, x2 has to be constrained by the data rather
    %   than the stated width. Find (y(x_a)-y_a)*(y(x_b)-y_b) For each pair
    %   of data. The intersection is at all points
    %   for which this product is negative. Then, find which pair is
    %   nearest x1+peakwidth. This is
    %   involved enough that I made a subfunction.
    [x2,y2]=DataIntersection(slope,times,totals,x1,y1,peakindex,peakwidth);
    fprintf(1,'Enforcing slope %g. Effective half-width is %g\n',...
slope,abs(x2-x1));
end
% The slope for the neutral yield is strictly required to be proportional
% to the scaling factor between the two spectra. For now, I just assume
% that the factor is the peak height quotient. This could be one
% of many optional
% inputs.
neuslope=slope*neutrals(peakindex)/totals(peakindex);
% Once that's determined, repeat the process of finding the right-most
% endpoint. Note that the constraint here is still x1 from the first
% spectra.
[x2neu,y2neu]=DataIntersection(neuslope,times,neutrals,x1,y1neu,...
peakindex,peakwidth);
[temp,x2minus]=min(abs(times-x2));
if(x2 < times(x2minus))
    x2minus=x2minus-1;
end

%Insert the interpolated points into the data for
%integration purposes. This way we don't fudge the result.
timesaug=[times(1:x1minus); x1; times(x1minus+1:x2minus);...
 x2; times(x2minus+1:end)];
timesneuaug=[times(1:x1minus); x1; times(x1minus+1:x2minus);...
 x2neu; times(x2minus+1:end)];
totalsaug=[totals(1:x1minus); y1; totals(x1minus+1:x2minus);...
 y2; totals(x2minus+1:end)];
```

```
neutralsaug=[neutrals(1:x1minus); y1neu;...
 neutrals(x1minus+1:x2minus); y2neu; neutrals(x2minus+1:end)];

%The following vectors will be used later to make sure that the integral is
%positive. Noise on the neutral yield will sometimes result in integrating
%when the function is *below* the background line. Not good. The check for
%this right now is rudimentary.
neuline=neuslope*(timesneuaug-x1)+y1neu;
signcheck=neutralsaug(x1minus+1:x2minus+2)-neuline(x1minus+1:x2minus+2);


washoldon=ishold; %Why doesn't this work anymore?

% Offset EVERY Y POSITION of total plot by max(neutrals);
yplotoffset=max(neutrals);

patch(timesaug(x1minus+1:x2minus+2),totalsaug(x1minus+1:x2minus+2)...
+yplotoffset,'r');
hold on;
totalcombinedarea=trapz(timesaug(x1minus+1:x2minus+2),...
totalsaug(x1minus+1:x2minus+2));
totalbackgroundarea=(timesaug(x2minus+2)-timesaug(x1minus+1))...
*(totalsaug(x2minus+2)+totalsaug(x1minus+1))/2;
integratedtotalarea=totalcombinedarea-totalbackgroundarea;
plot(times,totals+yplotoffset,'k');
plot([x1+(peakheight-y1)/slope x1-y1/slope],...
[peakheight+yplotoffset 0+yplotoffset]);
plot([timesaug(x1minus+1) timesaug(x2minus+2)],...
[totalsaug(x1minus+1)+yplotoffset totalsaug(x2minus+2)+yplotoffset],'g');


fprintf(1,'Total background: y=%g t + %g\n',slope,y1-slope*x1);
% Any code in this file can be altered, but it is VERY IMPORTANT that the
% limits for the patch function above match the limits in the below call to
% the integrating trapz function. Otherwise, the program will draw one
% thing and calculate another.
integratedtotalarea=trapz(timesaug(x1minus+1:x2minus+2),...
totalsaug(x1minus+1:x2minus+2)) - ...
    (x2-x1)*(y2+y1)/2;
fprintf(1,'Total area: %g\n',integratedtotalarea);

% I plot the neutral background line before I check for spurious
% integration.
plot([x1+(yplotoffset-y1neu)/neuslope x1-y1neu/neuslope],[yplotoffset 0]);
plot(times,neutrals,'k');
```

```
[x1neu,y1neu]=DataIntersection(neuslope,times,neutrals,x2neu,y2neu,...
peakindex,-(peakwidth-i*tstep));

%Here is the check for spurious negative integration. It just checks near
%the beginning (not AT the beginning, because that is always on the curve)
%for any time that the background line plotted in the previous line is
%actually ABOVE the data. If found, it will attempt to compensate by
%checking nearby data points for when this is no longer the case. This is
%not robust at all. It totally fails if the bad area comes after the second
%element.
j=2;
if signcheck(j)<0
    plot(x1,y1neu,'m.');
    fprintf(1,'Warning: Negative area found. ')
    while signcheck(j)<0 && j<5 % 5 would be a lot of thrown-out points.
        x1minus=x1minus+1; j=j+1;
    end
    fprintf(1,'Excluding %g points\n',j-2);
    fprintf(1,'A purple dot has been drawn where the original limit
of integration was.\n');
    % In this case, we should again find the intersection based on the new
    % constraint and insert this into the original time vector. Then, since
    % x1minus has already been altered, the rest of the code works the
    % same. Note that I call DataIntersection with a negative peakwidth.
    % It works that way.
    [x1neu,y1neu]=DataIntersection(neuslope,times,neutrals,x2neu,y2neu,...
peakindex,-(peakwidth-j*tstep));
    timesneuaug=[times(1:x1minus); x1neu; times(x1minus+1:x2minus);...
x2neu; times(x2minus+1:end)];
    neutralsaug=[neutrals(1:x1minus); y1neu;...
    neutrals(x1minus+1:x2minus); y2neu; neutrals(x2minus+1:end)];
end

patch(timesneuaug(x1minus+1:x2minus+2),..
neutralsaug(x1minus+1:x2minus+2),'r');
neutralcombinedarea=trapz(timesneuaug(x1minus+1:x2minus+2),...
neutralsaug(x1minus+1:x2minus+2));
neutralbackgroundarea=(timesneuaug(x2minus+2)-timesneuaug(x1minus+1))...
*(neutralsaug(x2minus+2)+neutralsaug(x1minus+1))/2;
integratedneutralarea=neutralcombinedarea-neutralbackgroundarea;
%plot(times,neutrals,'k');
plot([timesneuaug(x1minus+1) timesneuaug(x2minus+2)],...
[neutralsaug(x1minus+1) neutralsaug(x2minus+2)],'g');
fprintf(1,'Neutral background: y=%g t + %g\n',neuslope,y1neu-neuslope*x1);
```

```
fprintf(1,'Neutral area: %g\n',integratedneutralarea);
fprintf(1,'Neutral fraction: %g ',integratedneutralarea/...
integratedtotalarea);
toterror=sqrt(integratedtotalarea/tstep);
neuerror=sqrt(integratedneutralarea/tstep);
nferror=(integratedneutralarea/integratedtotalarea)*((neuerror/...
(integratedneutralarea/tstep))+(toterror/(integratedtotalarea/tstep)));
fprintf(1,'+/- %g\n',nferror);
%retain hold state; or not. This used to work. I think patch breaks it.
if(~washoldon)
    hold off;
end
axis([min(times) max(times) min(neutrals) max(totals)+yplotoffset]);
```

Needed for this is the function to read in a text file with a header.

```
function [header, data] = hdrload(file)

% HDRLOAD Load data from an ASCII file containing a text header.
%     Modified 6-13-07 to ignore blank lines -R. Gann
%     [header, data] = HDRLOAD('filename.ext') reads a data file
%     called 'filename.ext', which contains a text header.  There
%     is no default extension; any extensions must be explicitly
%     supplied.
%
%     The first output, HEADER, is the header information,
%     returned as a text array.
%     The second output, DATA, is the data matrix.  This data
%     matrix has the same dimensions as the data in the file, one
%     row per line of ASCII data in the file.  If the data is not
%     regularly spaced (i.e., each line of ASCII data does not
%     contain the same number of points), the data is returned as
%     a column vector.
%
%     Limitations:  No line of the text header can begin with
%     a number.  Only one header and data set will be read,
%     and the header must come before the data.
%
%     See also LOAD, SAVE, SPCONVERT, FSCANF, FPRINTF, STR2MAT.
%     See also the IOFUN directory.


% check number and type of arguments
if nargin < 1
  error('Function requires one input argument');
```

```
elseif ~isstr(file)
  error('Input must be a string representing a filename');
end


% Open the file.  If this returns a -1, we did not open the file
% successfully.
fid = fopen(file);
if fid==-1
  error('File not found or permission denied');
  end


% Initialize loop variables
% We store the number of lines in the header, and the maximum
% length of any one line in the header.  These are used later
% in assigning the 'header' output variable.
no_lines = 0;
max_line = 0;


% We also store the number of columns in the data we read.  This
% way we can compute the size of the output based on the number
% of columns and the total number of data points.
ncols = 0;


% Finally, we initialize the data to [].
data = [];


% Start processing.
line = fgetl(fid);
if ~isstr(line)
  disp('Warning: file contains no header and no data')
  end;
%  if(~strcmp(line,''))
[data, ncols, errmsg, nxtindex] = sscanf(line, '%f');
%end


% One slight problem, pointed out by Peter vanderWal: If the
% first character of the line is 'e', then this will scan as
% 0.00e+00. We can trap this case specifically by using the
% 'next index' output: in the case of a stripped 'e' the next
```

```
% index is one, indicating zero characters read.  See the help
% entry for 'sscanf' for more information on this output
% parameter. We loop through the file one line at a time until
% we find some data.  After that point we stop checking for
% header information. This part of the program takes most of the
% processing time, because fgetl is relatively slow (compared to
% fscanf, which we will use later).
while isempty(data)|(nxtindex==1)
  if(~strcmp(line,''))
  no_lines = no_lines+1;
  max_line = max([max_line, length(line)]);
  % Create unique variable to hold this line of text information.
  % Store the last-read line in this variable.
  eval(['line', num2str(no_lines), '=line;']);
  end
  line = fgetl(fid);
  if ~isstr(line)
    disp('Warning: file contains no data')
    break
    end;
  [data, ncols, errmsg, nxtindex] = sscanf(line, '%f');
  end % while


% Now that we have read in the first line of data, we can skip
% the processing that stores header information, and just read
% in the rest of the data.
data = [data; fscanf(fid, '%f')];
fclose(fid);


% Create header output from line information. The number of lines
% and the maximum line length are stored explicitly, and each
% line is stored in a unique variable using the 'eval' statement
% within the loop. Note that, if we knew a priori that the
% headers were 10 lines or less, we could use the STR2MAT
% function and save some work. First, initialize the header to an
% array of spaces.
header = setstr(' '*ones(no_lines, max_line));
for i = 1:no_lines
  varname = ['line' num2str(i)];
%  if(strcmp(line1,''))
%  fprintf(1,'line is empty');
%  end
  % Note that we only assign this line variable to a subset of
```

```
  % this row of the header array.  We thus ensure that the matrix
  % sizes in the assignment are equal.
  eval(['header(i, 1:length(' varname ')) = ' varname ';']);
  end


% Resize output data, based on the number of columns (as returned
% from the sscanf of the first line of data) and the total number
% of data elements. Since the data was read in row-wise, and
% MATLAB stores data in columnwise format, we have to reverse the
% size arguments and then transpose the data.  If we read in
% irregularly spaced data, then the division we are about to do
% will not work. Therefore, we will trap the error with an EVAL
% call; if the reshape fails, we will just return the data as is.
eval('data = reshape(data, ncols, length(data)/ncols)'';', '');
```